Smart Nanocomposites

Volume 2, Number 1

Table of Contents

Nova Science Publishers, Inc.
New York

Smart Nanocomposites

This Journal presents new studies in the fast growing area of smart materials, in particular, composite nanostructured materials. It focuses on the physics and physical chemistry of surfaces, interfaces, thin films and coatings, nanoparticles and other nanostructures, as well as on their new and smart applications. Original approaches in fabrication and applications of nanostructured materials will get special attention. Nanostructured ceramics, alloys, various nanocarbon forms (nanotubes, fullerenes, graphene) and their composites used in sensors (including single molecule sensing) and actuators, artificial metabolism, drug delivery, selective membranes, fuel cells, energy storage, and photovoltaics are just a few examples of new classes of materials and applications that are within the scope of the Journal. It features the results of interdisciplinary research from universities, national labs, and privately owned companies.

The Journal is peer-reviewed with the highest standards and quality of publications. The purpose of this Journal is to bring the most up-to-date advances in nanotechnology together, and to give research groups the opportunity to compare their results with other groups' data. To achieve this, the Journal focuses mostly on practical applications of nanodevices, and on proof of the concept publications. Areas of interest include (but not are limited to): sensors, smart membranes, smart coatings for corrosion protection, aspects of significance to nanorobots: power supplies, nanorobot manipulating devices, and microchips for artificial intelligence. The Journal also deals with safety issues: safety of nanotechnology to the environment, controlling the nanodevices, and other aspects.

Smart Nanocomposites
is published in two issues per year by

Nova Science Publishers, Inc.
400 Oser Avenue, Suite 1600
Hauppauge, New York 11788-3619, U.S.A.
Telephone: (631) 231-7269
Fax: (631) 231-8175
E-mail: main@novapublishers.com
Web: www.novapublishers.com

ISSN: 1949-4823

Subscription Rate per Volume (2011)
Print: $195 Electronic: $195 Combined Print + Electronic: $292.50
Personal Subscription Rate (2011): $50

Additional color graphics might be available in the e-version of this journal.

Smart Nanocomposites
Volume 2, Number 1
ISSN: 1949-4823

SYNTHESIS, SPECTROSCOPIC INVESTIGATION AND ANTIMICROBIAL STUDIES OF METAL COMPLEXES OF 7,12-DIOXO-3,4,9,10-TETRAPHENYL-1,2,5,6-TETRAAZACYCLODODECA-2,4,8,10-TETRAENE-8,11-DICARBONITRILE

Abdou S. El-Tabl*[a], Ahemd M. A. El-Seidy[b], Mohamad M. E. Shakdofa[b] and Alaa El-Deen A. I. Hamdy[a]

[a]Department of Chemistry, Faculty of Science,
El-Menoufia University, Shebin El-Kom, Egypt
[b]Inorganic Chemistry Department,
National Research Center, Dokki, Cairo, Egypt

ABSTRACT

New series of Cu(II), Ni(II), Co(II), Cd(II), Mn(II), Zn(II), Fe(III) and Cr(III) of the 7,12-dioxo-3,4,9,10-tetraphenyl-1,2,5,6-tetraazacyclododeca-2,4,8,10-tetraene-8,11-dicarbonitrile, (H_2L), have been synthesized and characterized by elemental analyses, IR, UV-VIS, ^{1}H-NMR, mass and ESR spectra, magnetic susceptibility and molar conductivity measurements. The spectral data and magnetic measurements of the complexes indicate that, the ligand behaves either as neutral bidentate, monobasic bidentate, neutral tetradentate or bibasic tetradentate ligand. The geometries of the metal complexes are either square planar or octahedral. The antibacterial and antifungal activities of the compounds showed that, some of metal complexes exhibited a greater inhibitory effect than standard drugs(Tetracycline) for bacteria, (Amphotericin B) for fungi.

Keywords: Schiff base, metal complexes, synthesis, spectroscopic studies, ESR, antimicrobial.

* Corresponding Author E-mail: asaeltabl@yahoo.com

INTRODUCTION

There has been considerable interest in the synthesis of transition metal complexes of macrocyclic ligand systems because they play vital roles in biological systems [1]. Also, interest in these species stems largely from the enhanced kinetic and thermodynamic stability of their complexes relative to those of related open chain ligands. Macrocyclic complexes are also of interest because of the synthetic flexibility involved in their preparation which allows for systematic variation in parameters such as ring size, the nature of the donor atoms, and the steric and electronic effects associated with the groups located on the periphery of the macrocyclic ring [2]. There has been a spectacular growth in the interest in metal complexes with tetraazamacrocyclic ligands followed by extensive work on the metal controlled template synthesis of macrocyclic species [3]. Macrocyclic metal complexes using acetylacetone and 2,6 diacetyl pyridine have been reported [4]. Based upon the above consideration and in continuation to our earlier studies on the metal(II)/(III) macrocyclic complexes [5], This article aimedto synthesis, spectroscopic investigation and antimicrobial studies on metal complexes of Cu(II), Ni(II), Co(II), Cd(II), Mn(II), Zn(II), Fe(III) and Cr(III) of 7,12-dioxo-3,4,9,10-tetraphenyl-1,2,5,6-tetraazacyclododeca-2,4,8,10-tetraene-8,11-dicarbonitrile.

EXPERIMENTAL SECTION

Material

All the reagents employed for the preparation of the ligand and its complexes were of the best grade available and used without further purification.

Synthesis of the Schiff base Ligand [H_2L](1)

A hot ethanolic solution (50 mL) of acetocyanohydrazide (12.1 mmole, 1.2g) was added to a hot ethanol solutionic (50 mL) of benzil (12.1 mmole, 2.55 g). The mixture was refluxed for 3h after cooling, the yellow precipitate was filtered off, washed with ethanol and dried under vacuum over anhydrous $CaCl_2$, Scheme 1.^{1}H NMR (300MHz, $CHCl_3$): δ =10.94 [S, 1H, O<u>H</u>], 10.79 [S, 1H, NH], 7.9-7.6 [m, 20H, aromatic].From this data the ligand present in Keto-enol form in liquid state (DMSO) which was supported by the presence of NH and OH groups.

Synthesis of the Metal Complexes

Metal complexes were prepared by mixing a hot methanolic solution of the metal salts with the required amount of a hot ethanolic solution of the ligand to form 1:1 or 1:2 L/M (ligand /metal). The reaction mixture was then refluxed for 2-4 hr depending on the metal salt used. The precipitates formed were filtered off, washed with ethanol, and dried under vacuum over anhydrous $CaCl_2$.

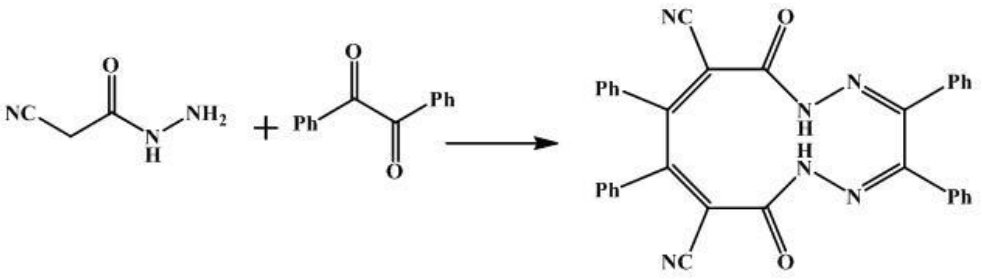

Scheme 1.Schematic representation for the formation of the ligand H_2L.

In-Vitro Antibacterial and Antifungal Activities

The investigation of the biological activities of the newly synthesized se ligand and its metal complexes and also their corresponding metal salts were carried out in the Botany Department Lab. of microbiology, Faculty of Science, El-Menoufia University, Egypt. The antibacterial and antifungal activities were investigated by disc diffusion method [6,7]. The antibacterial activities were done using gram positive bacteria (*Staphylococcus aurous*) and gram negative bacteria (*Escherichia coli*) and fungus (*Aspergillusflavus)* and yeast (*Candida albicans*) at 2000 ppm concentrations in DMSO. DMSO poured disc was used as negative control. The bacteria were subcultured in nutrient agar medium which was prepared using (g/L^{-1} distilled water) NaCl (5 g), peptone (5 g), beef extract (3 g), agar (20 g). The fungus was subcultured in Dox´s medium which was prepared using ($g.L^{-1}$ distilled water) yeast extract (1g), sucrose (30 g), $NaNO_3$, agar (20 g), KCl (0.5 g), KH_2PO_4 (1 g), $MgSO_4.7H_2O$ (0.5 g) and trace of $FeCl_3$.$6H_2O$.The yeast was subcultured in MYGP medium which prepared using ($g.L^{-1}$ distilled water) yeast extract (3g), Malt extract (3 g), glucose (10 g), agar (20 g), peptone (5 g). These mediums were then sterilized by autoclaving at 120 ^{0}C for 15 min. After cooling to 45 ^{0}C the medium was poured into 90 mm diameter Petri dishes and incubated at 37 ^{0}C or 28 ^{0}C, respectively. After few hours, Petri dishes were stored at 4 ^{0}C. Microorganisms were spread over each dish by using sterile bent Loop rod. The test is carried out by placing filter paper disks with a known concentration of the compounds on the surface of agar plates inoculated with a test organism. Standard antibacterial drug (Tetracycline), antifungal drug (Amphotericin B) and solution of metal salts were also screened under similar conditions for comparison. The Petri dishes were incubated for 48-72 h. at 37 or 30 ºC, respectively. The zone of inhibition was measured in millimeters carefully. All determinations were made in duplicated manner for all compounds. The average of the two independent readings was record.

Physical Measurements

The ligand and its metal complexes were analyzed for C, H, N, and Clcontents at the Micro-analytical Laboratory, Faculty of Science, Cairo University, Egypt. Analytical and physical data of the ligand and its metal complexes are reported in Table 1.

Table 1. Analytical and physical data of the ligand H_2L and its metal complexes

No.	Ligand/ Complexes	FW	Yield (%)	Analysis (%) / Found (calcd)					Λ^a_M
				C	H	N	M	Cl	
1	H_2L ($C_{34}H_{22}N_6O_2$)	546.6	72	74.5(74.7)	4.2(4.1)	15.5(15.4)	-	-	-
2	$[H_2LCu_2(OC(O)CH_3)_4].3H_2O$($C_{42}H_{40}Cu_2N_6O_{13}$)	963.9	87	52.2(52.3)	4.5(4.2)	8.9(8.7)	12.9(13.2)	-	11
3	$[H_2LCu(OC(O)CH_3)_2].H_2O$ ($C_{38}H_{30}CuN_6O_7$)	746.2	89	61.0(61.2)	4.2(4.1)	11.6(11.3)	8.3(8.5)	-	9
4	$[LCu_2Cl_2(H_2O)_2].H_2O$ ($C_{34}H_{26}Cl_2Cu_2N_6O_5$)	796.6	79	51.0(51.3)	3.4(3.3)	10.7(10.6)	15.9(16.0)	8.7(8.9)	15
5	$[H_2LCuCl_2].2H_2O$ ($C_{34}H_{26}Cl_2CuN_6O_4$)	717.1	77	56.9(57.0)	4.0(3.7)	11.8(11.7)	8.7(8.9)	9.8(9.9)	17
6	$[LCu_2(NO_3)_2(H_2O)_2].H_2O$ ($C_{34}H_{26}Cu_2N_8O_{11}$)	849.7	81	48.0(48.1)	3.3(3.1)	13.4(13.2)	14.7(15.0)	-	22
7	$H_2LCu_2(SO_4)_2(H_2O)_4$ ($C_{34}H_{30}Cu_2N_6O_{14}S_2$)	937.9	84	43.3(43.5)	3.5(3.2)	9.1(9.0)	13.4(13.6)	-	20
8	$[H_2LCu(SO_4)(H_2O)_2].2H_2O$ ($C_{34}H_{30}CuN_6O_{10}S$)	778.3	83	52.7(52.5)	4.1(3.9)	10.9(10.8)	8.0(8.2)	-	18
9	$H_2LNi_2(OC(O)CH_3)_4(H_2O)_4$ ($C_{42}H_{42}N_6Ni_2O_{14}$)	972.2	89	51.7(51.9)	4.1(4.4)	8.4(8.6)	11.9(12.1)	-	10
10	$H_2LNi_2(NO_3)_4(H_2O)_4C_{34}H_{30}N_{10}Ni_2O_{18}$	984.0	76	41.3(41.5)	3.4(3.1)	14.3(14.2)	11.7(11.9)	-	12
11	$H_2LCo_2Cl_4(H_2O)_4$ ($C_{34}H_{30}Cl_4Co_2N_6O_6$)	878.3	74	46.5(46.5)	3.6(3.4)	9.8(9.6)	13.1(13.4)	16.1(16.2)	14
12	$H_2LCo_2(NO_3)_4(H_2O)_4$ ($C_{34}H_{30}Co_2N_{10}O_{18}$)	984.5	75	41.3(41.5)	3.3(3.1)	14.4(14.2)	11.8(12.0)	-	18
13	$H_2LMn_2Cl_4.(H_2O)_4$ ($C_{34}H_{30}Cl_4Mn_2N_6O_6$)	870.3	79	46.(46.9)	3.7(3.5)	10.0(9.7)	12.4(12.6)	16.2(16.3)	19
14	$H_2LCr_2Cl_4(H_2O)_4$ ($C_{34}H_{30}Cl_4Cr_2N_6O_6$)	864.4	73	47.0(47.2)	3.5(3.5)	10.0(9.7)	11.9(12.0)	16.3(16.4)	20
15	$LFe_2Cl_4(H_2O)_4$ ($C_{34}H_{28}Cl_4Fe_2N_6O_6$)	870.1	78	46.8(46.9)	3.5(3.2)	9.8(9.7)	12.6(12.8)	16.2(16.3)	17
16	$[H_2LZn_2(OC(O)CH_3)_4].2H_2O$($C_{42}H_{38}N_6O_{12}Zn_2$)	949.5	71	53.0(53.1)	4.1(4.0)	9.0(8.9)	14.0(13.8)	-	8
17	$[LZnCl_2(H_2O)_2].3H_2O$ ($C_{34}H_{30}Cl_2N_6O_7Zn_2$)	836.3	73	48.6(48.8)	3.6(3.6)	10.2(10.1)	15.7(15.6)	8.4(8.5)	9

No.	Ligand/ Complexes	FW	Yield (%)	Analysis (%) / Found (calcd)					Λ^{a}_{M}
				C	H	N	M	Cl	
18	[LCd2Cl2(H2O)2].4H2O (C34H32Cd2Cl2N6O8)	948.4	78	43.0(43.1)	3.5(3.4)	9.0(8.9)	23.7(23.7)	7.4(7.5)	18
19	$[H_2LCdCl_2].3H_2O$ ($C_{34}H_{28}CdCl_2N_6O_5$)	783.9	82	52.0(52.1)	3.7(3.6)	10.9(10.7)	14.1(14.3)	9.0(9.0)	14
20	$[H_2LCd_2(OC(O)CH_3)_4].2H_2O$($C_{42}H_{38}Cd_2N_6O_{12}$)	1043.6	83	48.3(48.3)	3.8(3.7)	8.2(8.1)	21.3(21.5)	-	10
21	$[H_2LCd(OC(O)CH_3)_2].3H_2O$ ($C_{38}H_{34}CdN_6O_9$)	831.1	80	54.7(54.9)	4.4(4.1)	10.2(10.1)	13.7(13.5)	-	11
22	$[H_2LCd_2(NO_3)_4].2H_2O$ ($C_{34}H_{24}Cd_2N_{10}O_{15}$)	1037.4	79	39.2(39.4)	2.5(2.3)	13.6(13.5)	21.6(21.7)	-	17
23	$[H_2LCd_2(SO_4)_2].3H_2O$ ($C_{34}H_{28}Cd_2N_6O_{13}S_2$)	1017.6	81	40.0(40.1)	2.9(2.8)	8.5(8.3)	22.0(22.1)	-	14

Molar Conductance =Λ_m ($\Omega^{-1}cm^2mol^{-1}$).

The metal ion contents of the complexes were determined by the previously reported methods [8]. IR spectra of the ligand and its metal complexes were measured using KBr discs with a Jasco FT/IR 300E Fourier transform infrared spectrophotometer covering the range 400–4000 cm^{-1} and in the 500–100 cm^{-1} region using polyethylene-sandwiched Nujol mulls on a Perkin Elmer FT-IR 1650 spectrophotometer. ^{1}H NMR spectrum was obtained on 300 MHz VARIAN NMR spectrometers. Chemical shifts (ppm) are reported relative to TMS. The mass spectrumwas run at 70 eV with HP MODEL: MS. 5988A. The electronic spectra of the ligand and its complexes were obtained in Nujol mulls using a Shimadzu UV–240 UV–Vis recording spectrophotometer. Molar conductivities of the complexes in DMSO (10^{-3} M) were measured using a dip cell and a Bibbyconductimeter MC1 at room temperature. Magnetic moments at 298 K were determined using the Gouy method by the following equation $\mu_{eff} = 2.84\sqrt{\chi_m \times T}$with $Hg[Co(SCN)_4]$ as calibrate.Diamagnetic corrections were estimated from Pascal's constant.[9] ESR measurements of solid complexes at room temperature were made using a Varian E-109 spectrophotometer, with DPPH as a standard material. TLC is used to confirm the purity of the compounds.

RESULTS AND DISCUSSION

All metal complexes are stable in air and insoluble in common organic solvents but easily soluble in DMF and DMSO.The elemental and physical analyses (Table 1), spectral data (Table 2 ans 3), confirmed the suggested structures Figure 1.

Mass Spectra of the Ligand

The mass spectrum of the Schiff base ligand **(1)** revealed the molecular ion peak at m/e 547, which is coincident with the formula weight (546.6) for this ligand and supports the identity of the structure.

Infrared Spectra

The IR spectral data for the ligand **(1)** and its metal complexes are presented in Table 2. The IR spectrum of the ligand showed bands at3195, 1660 and 1600 cm^{-1} may be due to ν(NH), ν(C=O) and ν(C=N) groups, respectively [10]. The absence of any signals for hydroxy group indicates that the ligand is present in the keto-form in the solid state.The spectra of solid complexes are compared with those of the ligand in order to know the mode of bonding. The spectra showed that, the ligand behaved either as:

1. Neutral bidentate ligand, coordinating through C=O and C=N of one side of the ligand (complexes 3, 5,8, 17,19, 21), the mode of coordination was suggested by the following evidence: i) ν(C=O)and ν(C=N) of one side of the ligand were shifted to lower wave number with decreasing their intensities, while the other ones found almost at their original place, indicating that, only one of each pair were involved in the coordination, [11].ii) ν(NH)of one side of the ligand was shifted to higher wave

number, while the other one found almost at their original place, iii) the simultaneous appearance of new bands in the 655-634 and 520-549 cm^{-1} regions are due to the ν(M–N) and ν(M–O) vibrationsrespectively[12].

2. Neutral tetradentateligand, coordinating through C=O and C=N of both sides of the ligand (complexes2,7, 9-14,16, 20,22,23), the mode of coordination was suggested by the following evidence: i)all ν(C=O)and ν(C=N) were shifted to lower wave number with decreasing their intensities [11], ii) both ν(NH)were shifted to higher wave number, iii) the simultaneous appearance of new bands in the 657-637 and 555-530 cm^{-1} regions are due to the ν(M–N) and ν(M–O) respectively [12].
3. Dibasic tetradentateligand, coordinating through C-O and C=N of both sides of the ligand (complexes4, 6, 15, 18), the mode of coordination was suggested by the following evidence: i)all ν(C=N) were shifted to lower wave number with decreasing their intensities [11], ii) all ν(C=O) and ν(NH)disappeared with the appearance of bands due to new ν(C=N) found at higher wave number [13], the disappearance of the formed ν(OH) indicates the deprotonation of the ligands prior to coordination through oxygen atom.[13],iv) the simultaneous appearance of new bands in the 610-660 and 530-545 cm^{-1} regions are due to the ν(M–N) and ν(M–O) vibrationsrespectively[12].

Some complexes included water molecules. The broad bands in the 3600-3436 cm^{-1} region are due to coordinated water or water of crystallization. The bands for water of crystallization are different from those of coordinated water. The presence of water moleculeswithin the coordination sphere in the hydrated complexes 6-15 and 17-18is supported by the presence of bands in the 3600-3436 , 960-945 and 610-635 cm^{-1} regions due to OH stretching, H_2O rocking and H_2O wagging, respectively [14]. The absence of coordinated water molecules in complexes 2, 3, 5, 16 and 19-23 was confirmed from the absence of the rocking, twisting and wagging vibrational modes [14], as well as the presence of weak and broad bands in 3590-3510 cm^{-1} rangeindicating that, the water in all of these complexes is lattice rather than coordinated [15].

Extensive IR spectral studies reported on metal aceto complexes indicate that, the acetate ligand may coordinate to a metal center in either a mono-dentate, bidentate or bridging manner [17]. The $\nu_{asym.}(CO_2)$ and $\nu_{sym.}(CO_2)$ of the free acetate ions are at 1560 cm^{-1} and 1416 cm^{-1}, respectively [17]. In mono-dentate coordination ν(C=O) is found at higher energy than $\nu_{asym.}(CO_2)$ and ν(C-O) is lower than $\nu_{sym.}(CO_2)$. As a result, the separation between the two ν(CO) bands is much larger in mono-dentate complexes than in the free ion.[13,16].The opposite trend is observed in bidentateaceto coordination; the separation between ν(CO) is smaller than for the free ion. For bridging acetate with both oxygen atoms coordinated as in copper(ll) acetate, however, the two ν(CO) bands are close to the free ion values[13,16]. Complexes 2, 3, 9, 16, 20 and 21show two new bands appear in 1575-1568 and 1366-1359 cm^{-1} regions, which may be attributed to $\nu_{asym}(COO^-)$ and $\nu_{sym.}(COO^-)$ respectively. The separation value (Δ) between $\nu_{asym}(COO^-)$ and $\nu_{sym.}(COO^-)$ in these complexes was more than 200 cm^{-1} (204-211), suggesting the coordination of carboxylate group in a mono-dentate fashion [17]. Further, the complex exhibits δ(COO) at 750 cm^{-1} which is considered diagnostic for unidentate acetates [16].

Table 2. IR frequencies of the bands (cm^{-1}) of ligand H_2L and its complexes and their assignments

No.	ν(H_2O)	ν(NH)	ν(C≡N)	ν(C=O)	ν(C=N)	νs(Coo), νas(Coo), (Δ), ν(NO3) or ν(SO4)	ν(M-N)	ν(M-O)	ν(M-Cl)
1	-	3195m	2225v.s	1660v.s	1600s	-	-	-	-
2	3585br	3205m	2228v.s	1645s,1640s	1590m	1575, 1365, 210	640m	530m	-
3	3515br	3210m,3196m	2227v.s	1663vs,1643s	1601s,1588m	1570,1362, 208	655m	520m	-
4	3510br	-	2225v.s	-	1610 m1587m	-	610w	540w	395w
5	3561br	3205m,3197m	2227v.s	1661vs,1647s	1599s,1578m	-	653m	522w	400m
6	3515br	-	2224v.s	-	1611m,1589m	1450, 1038, 1362, 700	650w	545w	-
7	3460br	3208	2225v.s	1644s	1592m	1200, 1110, 1055, 995, 615	657w	539w	-
8	3570br	3203m,3194m	2225v.s	1663v.s,1642s	1602 s,1580 m	1198, 1100. 1045, 1000, 605	634m	534m	-
9	3485br	3206m	2228v.s	1650s	1591m	1569, 1365, 204	648m	539m	-
10	3465br	3200m	2225v.s	1641s	1587m	1455, 1030, 1367, 710	645m	548m	-
11	3449br	3202m	2225v.s	1644s	1590m	-	645m	555m	384m
12	3455br	3199m	2225v.s	1640s	1588m	1453, 1030, 1365, 705	641w	247m	-
13	3450br	3204m	2226v.s	1650s	1585m	-	637m	530m	405m
14	3436br	3198m	2224v.s	1639s	1587m	-	650m	545m	375m
15	3460br	3203m	2225v.s	1643s	1590m	-	650m	530m	385w
16	3510br	3199m,3193m	2226v.s	1660vs,1649 s	1600 s,1687 m	1571, 1363, 208	648m	534m	-
17	3560br	3203m,3196m	2225v.s	1644s	1589m	-	640m	531m	402m
18	3600br	-	2225v.s	-	1608m,1591m	-	660m	537m	405m
19	3590br	3204m,3195m	2226v.s	1660vs,1638 s	1601s,1590 m	-	653m	534m	399w

No.	ν(H_2O)	ν(NH)	ν(C≡N)	ν(C=O)	ν(C=N)	νs(Coo), νas(Coo), (Δ), ν(NO3) or ν(SO4)	ν(M-N)	ν(M-O)	ν(M-Cl)
20	3540br	3197m	2227v.s	1640s	1584m	1568, 1364, 204	645m	540m	-
21	3530br	3202m, 3194m	2225v.s	1662v.s 1646s	1599s 1587m	1570, 1359, 211	648m	549m	-
22	3510br	3201m	2225v.s	1638s	1583m	1451, 1040, 1363, 711	662m	549m	-
23	3535br	3206m	2225v.s	1642s	1588m	1195, 1105. 1038, 1003, 611	649m	534m	-

m=medium, s=strong, b=broad, w=week, sh=shoulder.

Table 3. The electronic spectral bands (nm) and magnetic moment (B.M)for the ligand and its complexes

No.	Ligand/ Complexes	π–π*, n–π*, and CT bands	d–d bands	μ_{eff} in BM
1	H_2L	285, 320, 355, 400	-	-
2	$[H_2LCu_2(OC(O)CH_3)_4].3H_2O$	300, 335, 370, 405	539	1.53
3	$[H_2LCu(OC(O)CH_3)_2].H_2O$	290, 330, 365, 411	540	1.81
4	$[LCu_2Cl_2(H_2O)_2].H_2O$	295, 325, 380, 410	545	1.6
5	$[H_2LCuCl_2].2H_2O$	299, 323, 365, 408	545	1.82
6	$[LCu_2(NO_3)_2(H_2O)_2].H_2O$	295, 330, 381, 403	550	1.50
7	$H_2LCu_2(SO_4)_2(H_2O)_4$	298, 334, 364, 420	489, 560, 695	1.48
8	$[H_2LCu(SO_4)(H_2O)_2].2H_2O$	296, 342, 365, 405	495, 570, 680	1.84
9	$H_2LNi_2(OC(O)CH_3)_4(H_2O)_4$	291, 330, 362, 409	510, 615, 930	2.12
10	$H_2LNi_2(NO_3)_4(H_2O)_4$	300, 340, 365, 415	495, 625, 915	2.4
11	$H_2LCo_2Cl_4(H_2O)_4$	294, 339, 382, 420	470, 620	3.1

Table 3. (Continued)

No.	Ligand/ Complexes	π–π*, n–π*, and CT bands	d–d bands	μ_{eff} in BM
12	$H_2LCo_2(NO_3)_4(H_2O)_4$	305, 345, 375, 408	490 , 645	2.9
13	$H_2LMn_2Cl_4.(H_2O)_4$	300, 341, 382, 418	450, 500, 601	3.6
14	$H_2LCr_2Cl_4(H_2O)_4$	315, 344, 376, 421	560	1.58
15	$LFe_2Cl_4(H_2O)_4$	305, 335, 375, 414	575, 645	4.51
16	$[H_2LZn_2(OC(O)CH_3)_4].2H_2O$	300, 341, 380, 425	-	-
17	$[LZnCl_2(H_2O)_2].3H_2O$	308, 349, 370, 419	-	-
18	$[LCd_2Cl_2(H_2O)_2].4H_2O$	298, 335, 365, 409	-	-
19	$[H_2LCdCl_2].3H_2O$	305, 345, 380, 413	-	-
20	$[H_2LCd_2(OC(O)CH_3)_4].2H_2O$	310, 350, 370, 422	-	-
21	$[H_2LCd(OC(O)CH_3)_2].3H_2O$	299, 339, 368, 410	-	-
22	$[H_2LCd_2(NO_3)_4].2H_2O$	315, 342, 370, 417	-	-
23	$[H_2LCd_2(SO_4)_2].3H_2O$	308, 337, 372, 424	-	-

The spectra of the complexes 4, 5, 11, 13-15 and 17-19 showed assignable weak intensity ν (M-CI) bands in 405-394 cm^{-1} range, indicating terminal chloro ligands [18].The spectrumof nitrato complexes show bands in 1455-1450 (υ_1),1040-1030 (υ_2), 1367-1362 (υ_4) and 710-700 (υ_5) regions withυ_1–υ_4 separation of 88 cm^{-1}, characteristic of mono-dentatenitrato group [17].The sulphate ion has a regular tetrahedral structure belonging to the point group T_d,[19]. In its ionic state, SO_4 has nine vibrational degrees of freedom, distributed in four normal modes of vibration. Out of these, only two are infrared active[19]. When SO_4functions as a unidentate ligand, the oxygen coordinating to a metal atom is no longersymmetrically equivalent to the other three oxygen atoms and the effective symmetry of $SO_4$is lowered to C_3, [20].In C_3,symmetry, six infrared absorption bands are observed. WhenSO_4 functions as a bidentate group, its effective symmetry is further lowered to C_{2v}. InC_{2v}symmetry, eight modes of vibration, out of the total of nine, are infrared active[20]. The sulphato complexes showed bands in the 1195-1200, 1100-1110, 1038-1045, 995-1003 cm^{-1} regions indicating a bidentate coordinating sulphato group [21].

Molar Conductance Data

The molar conductivities of the complexes in DMF (10^{-3} M) are listed in table 1. All complexes show a non-electrolyte nature [22].

Electronic Spectra and Magnetic Moments

The solid state spectrum of the ligand shows bands at 285 nm assignable to the phenyl ring $\pi\rightarrow\pi^*$ transitions [23] and 355 nm assignable to $\pi\rightarrow\pi^*$ of C=N groups [24]. The $n\rightarrow\pi^*$ transition associated with the (C=N) moiety found around 400 nmin the spectrum of the free ligand and is generally shifted to higher energy on complexation[25]. There are also charge-transfer transitions partially responsible for the intense colors of the complexes. The bands present at energies above 333 nm in the spectra of the metal complexes are due to Cl→ M(II) and O→ M(II) transitions [26]. Copper complexes 7 and 8 showed signals in 489-495, 560-570 and 680-695 nm regions, which were assigned to $^2B_{1g}\rightarrow{}^2E_g$, $^2B_{1g}\rightarrow{}^2B_{2g}$ and $^2B_{1g}\rightarrow{}^2A_{1g}$ transitions of copper(II) ion in a tetragonally elongated octahedral structure [27], while complexes 2-6show a broad band in 539-550 nm region due to $^2B_{1g}\rightarrow{}^2E_g$ transition in a square planar Cu(II) structure [28]. The magnetic moment of complexes3, 5, and 8lie in the 1.84-1.81 B.M. range,indicating the presence of one unpaired electron[29].The nickel(ll) complexes9 and 10have spectra typical of an octahedral system showing bands lie in495-510,615-625and915-930nm region, may be assigned to $^3A_{2g}\rightarrow{}^3T_{1g}(P)$ and (ν_3),$^3A_{2g}\rightarrow{}^3T_{1g}(F)$ (ν_2)and $^3A_{2g}(F)\rightarrow{}^3T_{2g}(F)$ (ν_1)transitions, respectively, [28,30].The ν_2/ν_1ratio were1.51 and 1.46 respectively. Complex 10 showed ratio less than the usual range of 1.5-1.75, indicating distorted octahedral nickel(II) complex [31].The cobalt(II) complexes 11 and 12 have spectra typical of an octahedral system showing two bands, in the 470-490 and 620-645 nm regions, assignable to $^4T_{1g}(F)\rightarrow{}^4T_{2g}(P)$($\nu_3$) and $^4T_{1g}(F)\rightarrow{}^4A_{2g}$ (F) (ν_2)transitions, respectively, indicating an octahedral structure [30,32]. Manganese(II) complexes 13 showed bands at 450, 500 and 601 nm, these bands were corresponding to $^6A_{1g}\rightarrow{}^4E_g$, $^6A_{1g}\rightarrow{}^4T_{2g}$ and $^6A_{1g}\rightarrow{}^4T_{1g}$ transitions which is compatible to an octahedral structure for manganese(II) complexes [33].

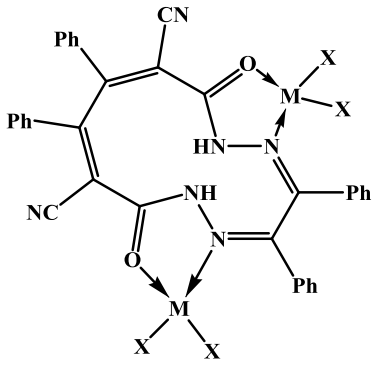

$[H_2LM_2X_4].nH_2O$
Complex 2: M=Cu, X= $OC(O)CH_3$, n=3
Complex 16: M=Zn, X= $OC(O)CH_3$, n=2
Complex 20: M=Cd, X= $OC(O)CH_3$, n=2
Complex 22: M=Cd, X= NO_3, n=3
Complex 23: M=Cd, X and X= SO_4, n=3

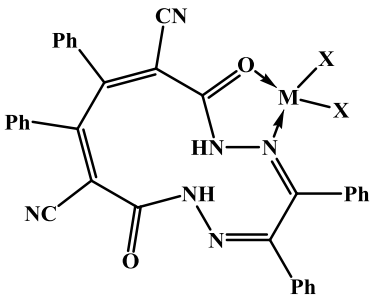

$[H_2LMX_2].nH_2O$
Complex 3: M=Cu, X= $OC(O)CH_3$, n=1
Complex 5: M=Cu, X= Cl, n=1
Complex 19: M=Cd, X= Cl, n=3
Complex 21: M=Cd, X= $OC(O)CH_3$, n=3

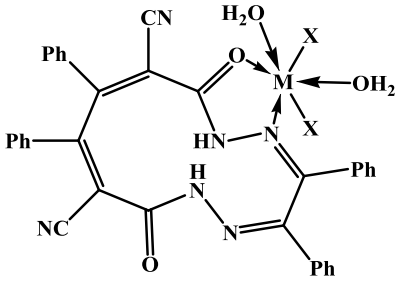

$[H_2LMX_2(H_2O)_2].nH_2O$
Complex 8: M=Cu, X and X= SO_4, n=2
Complex 17: M=Zn, X= Cl, n=3

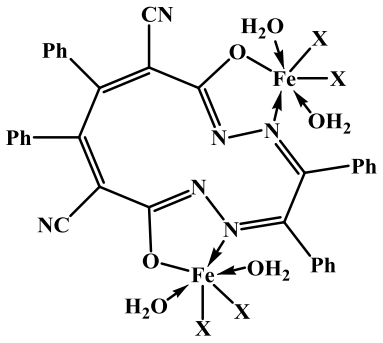

Complex 15: $[LFe_2Cl_4(H_2O)_4]$

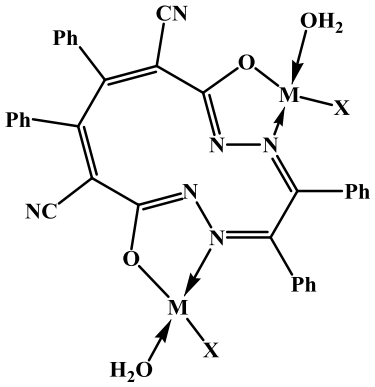

$[LM_2X_2(H_2O)_2].nH_2O$
Complex 4: M=Cu, X= Cl, n=1
Complex 6: M=Cu, X= NO_3, n=1
Complex 18: M=Cd, X= Cl, n=1

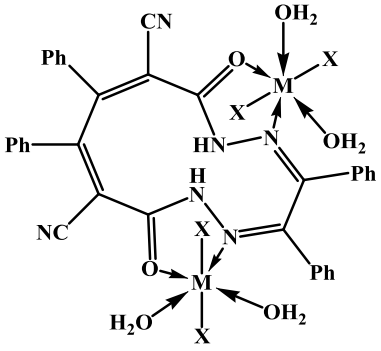

$[H_2LM_2X_4(H_2O)_4].nH_2O$
Complex 7: M=Cu, X and X= SO_4
Complex 9: M=Ni, X=$OC(O)CH_3$
Complex 10: M=Ni, X= NO_3
Complex 11: M=Co, X= Cl
Complex 12: M=Co, X= NO_3
Complex 13: M=Mn, X= Cl
Complex 14: M=Cr, X= Cl

Figure 1. The proposed structures of metal complexes of the ligand H2L1.

Chromium (III) complex 14 showed band 560 nm which is attributed to $^4A_2 \rightarrow {}^4T_1$ transitions of six coordinate chromium(III) complex [34]. Iron(III) complex 15 gave band at 600 nm is due to $^6A_1 \rightarrow {}^4T_1$ transitions, suggesting octahedral structure [32,33].The magnetic moments of complexes 2, 4, 6-7 and 9-15were lower than the spin-only value, implying an operation of spin-exchange interactions take place between metal ions [35]. The structure representation of metal complexes is present in Figure 1.

ESR Spectra

The ESR spectra of polycrystalline samples of copper(II) complexes (2-8) at room temperatures (298 K) were of axial type with $g_{||} > g_{\perp}$ characteristic of $^2B_{1(dx2-y2)}$ ground state [36]. The complexes show $g_{||} > g_{\perp} > g_e$, indicating a $d_{(x2-y2)}$ ground state [37]. All complexes, except complex 5, exhibit $g_{||} < 2.3$, suggesting considerable covalent characters around the copper ion. Kivelson and Neiman [38] have reported that a $g_{||}$ value greater than 2.3 indicates ionic character, as in complex 5. The g-values were related by the expression[5], $G = (g_{||}-2)/(g_{\perp}-2)$, if $G > 4.0$, then local tetragonal axes were aligned parallel or only a slightly misaligned, if $G < 4.0$, significant exchange coupling is present, Table 4.

Complexes 3, 5and 8showed $G > 4.0$ indicate that there is no direct copper-copper interaction in the solid state. In case of other complexes, the G value is <4, which suggests considerable exchange interactionstakes place. The $g_{||}/A_{||}$is taken as an indication for the stereochemistry of the copper(II) complexes. Addison [39] has suggested that, this ratio may be an empirical indication of the tetrahedral distortion of the square planar geometry. The values of $g_{||}/A_{||}$quotient in the range 105–135 $cm^{-1}$are expected for copper complexes within perfectly square-based geometry and those higher than 150 cm^{-1} for tetrahedrally distorted complexes. The values of $g_{||}/A_{||}$ for complexes 2-6lie in therange 125-134 indicating a square planar geometry while the value for complexes 7and8 lie in therange203-212 indicating an octahedral geometry around copper ion.

Table 4. ESR parameters for copper(II) complexes

No.	Complexes	$g_{//}$	$g_{\perp}$	$g_{//}/A_{//}$	G	$g_{av.}$
2	$[H_2LCu_2(OC(O)CH_3)_4].3H_2O$	2.25	2.09	134	2.78	2.14
3	$[H_2LCu(OC(O)CH_3)_2].H_2O$	2.29	2.07	125	4.14	2.14
4	$[LCu_2Cl_2(H_2O)_2].H_2O$	2.26	2.1	127	2.60	2.15
5	$[H_2LCuCl_2].2H_2O$	2.32	2.05	130	6.4	2.14
6	$[LCu_2(NO_3)_2(H_2O)_2].H_2O$	2.17	2.09	134	1.9	2.12
7	$H_2LCu_2(SO_4)_2(H_2O)_4$	2.29	2.11	212	2.6	2.17
8	$[H_2LCu(SO_4)(H_2O)_2].2H_2O$	2.23	2.04	203	5.75	2.10

Biological Activity

The antibacterial and antifungal activities of the ligand and its metal complexes were screened on bacterial and fungal strains using the disk diffusion method. Most of the metal complexes were more active than parent ligand and the solution of metal ions. The inhibition zone diameter of the compounds is shown in Figures 2 and 3. It was reported that, some drugs have greater activity when administered as metal complexes than that as free organic compounds [40].The increased activity of the metal complexes can be explained on the basis of chelation theory [11]. In a complex, the positive charge of the metal is partially shared with the donor atoms present in the ligands, and there may be π-electron delocalization over the whole chelating system [41], this increases the lipophilic character of the metal chelate and favors its permeation through the lipoid layer of the membranes. There are other factors which also increase the activity, which are increased solubility, conductivity, coordination mode and bond length between the metal and the ligand. The variation in the effectiveness of different compound against different organisms also depends either on the impermeability of the cell of the microbes or differences in ribosomes of microbial cells [42]. The variation of biological activity of the complexes may be due to change in electronic configuration of the metal and the environment around the metal ion.

The order of the activity of the compounds against Staphylococcus aurousis (18)>(20)=(17)>(19)=(23)>(22)(Tetracycline)>(21)=(9)>(13)=(8)>(15)=(3)>(16)=(2)>(Ligand) [Figure 2]. The order of the activity against Escherichia coli is (23)=(22)>(Tetracycline) (17)>(16)=(21)>(19)>(13)>(8)=(3)=(20)>(18)=(9)>(2)>(15)>(Ligand)[Figure 2].

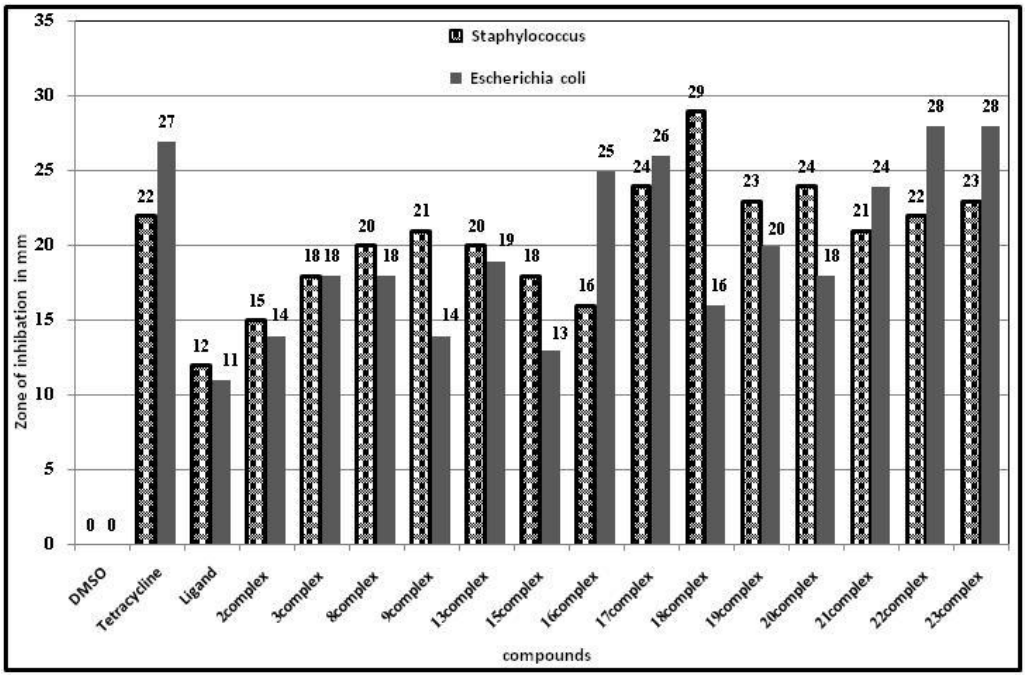

Figure 2. Antibacterial activity of the ligand and its metal complexes against bacteria (Staphylococcus aurous) and (Escherichia coli).

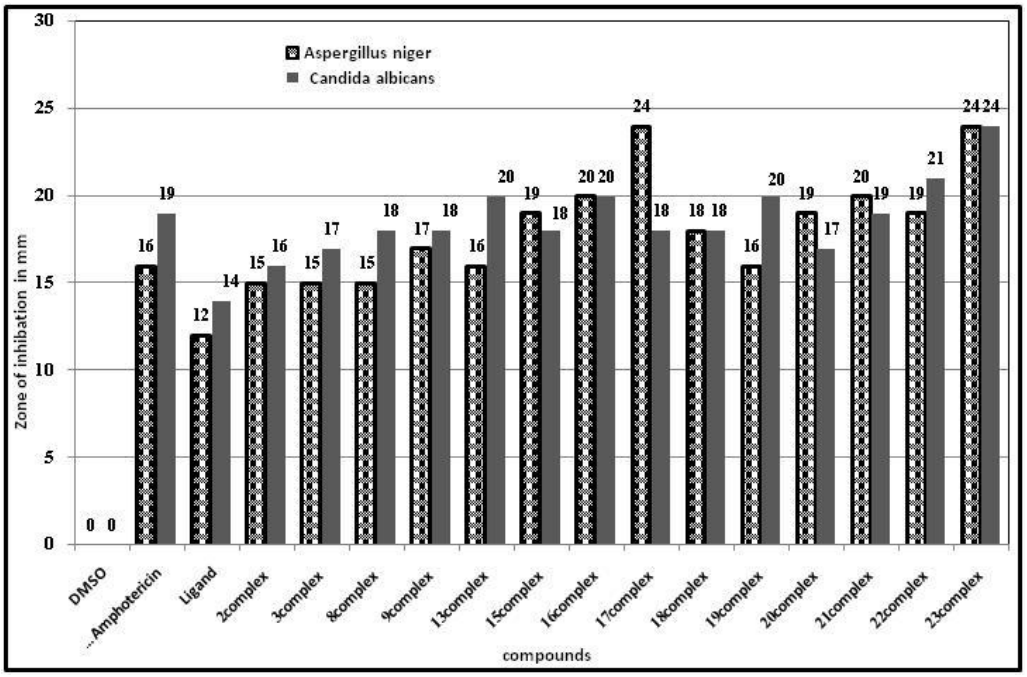

Figure 3. Antifungal activity of the ligand and its metal complexes against Fungus (Aspergillus flavus and (Candida albicans)).

The order of the activity against Aspergillusflavusis (23)=(17)>(21)=(16)>(20)=(22)=(15)>(18)>(9)>(13)=(19) =(Amphotricene B)>(8)=(3)=(2)>Ligand)[Figure 4]. However, the order of the activity against Candida albicans is (23)>(22)>(19)=(13)=(16)=(19)>(21)=(Amphotricene B)>(18)=(17)=(15)=(9)=(8)> (20)=(3)>(2)>(Ligand) [Figure 3]. From the above results, the activity of complexes against microorganism tested was significantly increased on coordination. Also we can deduce that the non-transition elements with completely filled d-orbital (Zn(II) and Cd(II) complexes show higher activity compared to the ligand and standard drugs than the transition elements with partly filled d-orbitals. Also the results show that small size anion is more active than big size anion.

CONCLUSION

The ligand and its corresponding Cu(II), Ni(II), Co(II), Cd(II), Mn(II), Zn(II), Fe(III) and Cr(III) complexes have been synthesized and spectrally characterized. In liquidstate (DMSO) the ligand present in Keto-enol form which was supported by the presence of NH and OH groups in the ^{1}H-NMR of the ligand but present only in keto form in solid state which is supported by the absence of any signals for ν(OH) in the IR spectrum of the ligand. The ligand acted either as neutral bidentate, neutral tetradentate or bibasic tetradentate ligand. All prepared complexes showed either octahedral or square planar geometries. Complexes 2, 4, 6-7, 9-16, 18, 20 and 22-23 showed magnetic moments lower than the spin-only value indicating spin-exchange interactions between metal ions. The antibacterial and antifungal activities of the compounds showed that, some of metal complexes exhibited a greater

inhibitory effect than the ligand, corresponding aqueous ions, and standard drugs as (Tetracycline) for bacteria, (Amphotericin B) for fungi.

REFERENCES

[1] Wade, P.W.;Hancock,R.D., "Crystallographic and molecular mechanics study of the copper perchlorate complex of a larger reinforced macrocycle", *J. Chem. Soc. Dalton Trans.*,(1990) 1323-1327.

[2] Melson,G.A., "In *Coordination chemistry of macrocyclic complexes*" Ed plenum, New York (1979).

[3] Matoda,K.-I.;Sakiyama, H.;Matsumoto, N.;Okawa,H.;Kida,S.,"Template Synthesis and Structure of a Dinuclear Lead(II) Complex of Novel Macrocycle Derived from 2,6-Diformyl-4-methylphenol and 1,9-Diamino-3,7-diazanonane", *Bull. Chem. Soc. Jpn.*, 65, (1992) 1176-1178.

[4] V.L.Goedken, J.J.Pluth, S.S.Panq,B.Bursten"Structure relations between the four-coordinate, S = 1, macrocyclic complex, [Fe($C_{22}H_{22}N_4$)], and the neutral ligand, $C_{22}H_{24}N_4$*" J. Am.Chem. Soc.*,1976,98, 8014-8021.

[5] El-Tabl A.S.,"Synthesis and Characterization of Cobalt(II)/(III), Nickel(II) and Copper(II) Complexes of New 14,15 and 16-Membered Macrocyclic Ligands" Bull. Korean. Chem. Soc.,25, (2004)1757-1763.

[6] Offiong,E.O.; Martelli,S., "Antibacterial activity of metal complexes of benzil and benzoin thiosemicarbazones" *IL Farmaco*, 49, (1994) 513-518.

[7] J.G. Collee, J.P. Duguid, A.G. Farser, B.D. Marmion "Practical Medical Microbiology" (eds)New York, Churchill Livingstone 1989.

[8] G. Svehla "Vo*gel's Textbook of Macro and Semi Micro Quantitative Inorganic Analysis*" 5th Edn, Longman Inc., New York (1979).

[9] L. Lewis, R.G. Wilkins "Modern coordination chemistry" *Interscience*, New York, 1960.

[10] El-Behery,M.;El-Twigry H.,"Synthesis, magnetic, spectral, and antimicrobial studies of Cu(II), Ni(II) Co(II), Fe(III), and UO_2(II) complexes of a new Schiff base hydrazone derived from 7-chloro-4-hydrazinoquinoline" *Spectrochim. Acta Part A*, 66, (2007)28-36.

[11] El-Wahab, Z.H.A.;Mashaly,M.M.;Salman,A.A.;El-Shetary,B.A.;Faheim, A.A., "Co(II), Ce(III) and UO_2(VI) bis-salicylatothiosemicarbazide complexes: Binary and ternary complexes, thermal studies and antimicrobial activity " *Spectrochim. Acta Part A*,60, (2004)2861-2873.

[12] Cukurovali, A.;Yilmaz, I.;Kirbag,S., "Spectroscopic Characterization and Biological Activity of Salicylaldehyde Thiazolyl Hydrazone Ligands and their Metal Complexes"*Trans. Met. Chem.*, 31, (2006)207-213.

[13] Youssef,N.S.;El-Zahany,E.;El-Seidy,A.M.A.;Caselli, A.; S.Cenini,"Synthesis and characterization of some transition metal complexes with a novel Schiff base ligand and their use as catalysts for olefin cyclopropanation*" J. Mol. Catal. A: Chem.*308, (2009)159-168.

[14] Teotia, M.; Gurthu, J.N.;Rama,V.B.,"Dimeric 5-and 6-coordinate complexes of tri and tetradentate ligands"*J. Inorg. Nucl. Chem.*, 42,(1980)821-831.

[15] Chen,C.-Y.;Chen, Q.-Z.;Wang, X.-F.;Liu,M.-S.;Chen, Y. F., " Synthesis, characterization, DNA binding properties, and biological activities of a mixed ligand copper(II) complex of ofloxacin*" Trans. Met. Chem.*, (34), (2009)757-763.

[16] Nakarnoto, K.,"Infrared and Raman Spectra of Inorganic and coordination compounds", Wiley Interscience, New York, 1986.

[17] Shauib,N.M.;Elassar,A.-Z.A.;El-Dissouky A.,"Synthesis and spectroscopic characterization of copper(II) complexes with the polydentate chelating ligand 4,4′-[1,4-phenylenedi(nitrilo)dipente-2-one" *Spectrochim. Acta Part A*, 63, (2006)714-722.

[18] Ferrari,M.B.;Fava,G.G.;Lanfranchi,M.;Pelizzi, C.;TarasconiP.,"Synthesis, spectroscopic and structural characterization of chlorobis(methyl pyruvate thiosemicarbazone)copper(I) and chlorobis(triphenylphosphine) (methyl pyruvate thiosemicarbazone)copper(I) toluene solvate (2/1)*" Inorg. Chem. Acta*,181 (1991) 253-262.

[19] Herzberg, G.,"*Infrared and Raman spectra of polyatomic molecules*" D. Van Nostrand Co., New York. 1956.

[20] Nakamoto,K.;Fujita, J.;Tanaka, S.;Kobayashi, M.,"Infrared Spectra of Metallic Complexes. IV. Comparison of the Infrared Spectra of Unidentate and Bidentate Metallic Complexes" *J. Am. Chem. Soc.* 79, (1957)4904-4908.

[21] Narang,K.K.;Sing, V.B.;"E.s.r. studies on acylhydrazine and hydrazone copper(II) sulfate complexes*" Trans. Met. Chem.*21, (1996)507-511.

[22] Geaey,W.J.,*"*The use of conductivity measurements in organic solvents for the characterization of coordination compounds"*Coord. Chem. Rev.*,7, (1971)81-122.

[23] Zhang,H.-Y.;Wu,K.-Z.;Zhang,J.-J.;Xu,S.-L.;Ren,N.;Bai,J.-H.;Tian, L.,"Synthesis, crystal structure and thermal decomposition kinetics of the complex $[Sm(BA)_3bipy]_2$"*Synthetic Metals,* 158, (2008)157-164.

[24] Wu,G.;Wang,X.;Li,J.;Zhao,N.;Wei,W.;Sun,Y.,"A new route to synthesis of sulphonato-salen-chromium(III) hydrotalcites: Highly selective catalysts for oxidation of benzyl alcohol to benzaldehyde" *Catal. Today*,131, (2008)402-407.

[25] Mostafa,S.I.;Ikeda, S.;Ohtani,B.,"Transition metal Schiff-base complexes chemically anchored on Y-zeolite: their preparation and catalytic epoxidation of 1-octene in the suspension and phase boundary systems" *J. Mol. Catal. A: Chem.*, 225, (2005) 181-188.

[26] Suzuki,M.;Koyama,H.;Kanatomi,H.;Murase,I.,"Copper(I) and Copper(II) Complexes of Tripod Ligands, Tris(2-alkylthioethyl)amine" *Bull. Chem. Soc. Jpn.*,53, (1980)1961-1964.

[27] El-Tabl,A.S.;Plass,W.;Buchholz,A.;Shakdofa,M.M.E., "Synthesis, spectroscopic investigation and biological activity of metal(lI) complexes with N_2O_4ligands *J. Chem. Research*, (2009) 582-587.

[28] Kumar,K.G.;John,K.S.,"Complexation and ion removal studies of a polystyrene anchored Schiff base" *React. Funct. Polym.*66, (2006)1427-1433.

[29] Nair,M.S.;Joseyphus, R.S., "Synthesis and characterization of Co(II), Ni(II), Cu(II) and Zn(II) complexes of tridentate Schiff base derived from vanillin and dl-α-aminobutyric acid " *Spectrochim Acta Part A*, 70, (2008)749-753.

[30] Mohamed,G.G.;El-Wahab,Z.H.A.,"Mixed ligand complexes of bis(phenylimine) Schiff base ligands incorporating pyridinium moiety: Synthe(sis, characterization and antibacterial activity*" Spectrochim. Acta Part A*,61, (2005)1059-1068.

[31] El-Tabl,A.S.;El-Enein,S.A.,"Reactivity of the new potentially Binucleating Ligand, 2-(Acetichydrazido-*N*-Methylidene-α-Naphthol)-Benzothiazol, towards Manganese(II), Nickel(II), Cobalt(II), Copper(II) and Zinc(II) salts" *J. Coord. Chem*,2004, 57, 281-294.

[32] A.B.P. Lever "Inorganic Electronic Spectroscopy" 2nd edn, Elsevier, Amsterdam, 1984.

[33] Singh,N.K.;Singh,S.B., "Complexes of 1-isonicotinoyl-4-benzoyl-3-thiosemicarbazide with manganese(II), iron(III), chromium(III), cobalt(II), nickel(II), copper(II) and zinc(II)*" Trans. Met. Chem.,* 26, (2001)487-495.

[34] Zhang,S.-W.;Liao, D.-Z.;Jiang,Z.-H.;Wang,G.-L.,*"*Synthesis and magnetic properties of trinuclear chromium(III)palladium(II)-chromium(III) complexes bridged by extended dioximato groups*" Trans. Met. Chem.,* 21, (1996)166-168.

[35] Youssef,N.S.;El-Zahany, E.;El-Seidy,A.M.A.,"Synthesis and Characterization of New Schiff Base Metal Complexes and Their Use as Catalysts for Olefin Cyclopropanation*" Phosphorus, Sulfur Silicon Relat. Elem*. 185,(2010)785-798.

[36] Chandra,S.;Kumar,U.,"Spectral and magnetic studies on manganese(II), cobalt(II) and nickel(II) complexes with Schiff bases" *Spectrochim. Acta, Part A,*61, (2005)219-224.

[37] R.N. Patel, N. Singh, V.L.N. Gundla"Synthesis, structure and properties of ternary copper(II) complexes of ONO donor Schiff base, imidazole, 2,2′-bipyridine and 1,10-phenanthroline" *Polyhedron,* 2006, 25, 3312-3318.

[38] Kivelson, D.;Neiman,R.,*"*ESR Studies on the Bonding in Copper Complexes" *J. Chem. Phys.* 35, (1961)149-155.

[39] A.W. Addison, in: K.D. Karlin, J. Zubieta (Eds.), Copper Coordination Chemistry Biochemical and Inorganic Perspectives, Adenine Press, New York, 1983.

[40] Shakir,M.;Azim,Y.;Chishti, H.-T.-N.;Parveen,S.,"Synthesis, characterization of complexes of Co(II), Ni(II), Cu(II) and Zn(II) with 12-membered Schiff base tetraazamacrocyclic ligand and the study of their antimicrobial and reducing power" *Spectrochim. Acta Part A,* 65, (2006)490-496.

[41] Sengupta,S.K.;Pandey,O.P.;Srivastava, B.K.;Sharma,V.K.,"Synthesis, structural and biochemical aspects of titanocene and zirconocene chelates of acetylferrocenyl thiosemicarbazones"*Trans. Met. Chem.,*23, (1998)349-353.

[42] Kurtoğlu, M.; Dağdelen, M. M.;Toroğlu, S.,"Synthesis and Biological Activity of Novel (*E,E*)-*vic*-dioximes*" Trans. Met. Chem.,* 31, (2006)382-388.

Smart Nanocomposites
Volume 2, Number 1
ISSN: 1949-4823

STRUCTURE, MAGNETIC AND ELECTRICAL PROPERTIES OF INMNAS LAYERS WITH MNAS INCLUSIONS

A. V. Alaferdov[a,b], Yu. A. Danilov[a,b], A. V. Kudrin[b], B. N. Zvonkov[b], O. V. Vikhrova[b], Yu. N. Drozdov[c] and S. Nicolodi[d]

[a]Faculty of Physics, N.I. Lobachevsky Nizhny Novgorod State University, Russia
[b]Physico-Technical Research Institute of N.I. Lobachevsky Nizhny Novgorod State University, Russia
[c]Institute for Physics of Microstructures, Russian Academy of Sciences, Nizhny Novgorod, Russia
[d]Institute of Physics, Federal University of Rio Grande do Sul, Porto Alegre, RS, Brazil

ABSTRACT

InMnAs layers, grown by pulse laser deposition at 320°C in the flux of hydrogen and arsine, represent a nanosystem with MnAs clusters. Ferromagnetic properties of the InMnAs layers up to room temperature were confirmed by the results of the anomalous Hall Effect and magnetization measurements. Resistivity dependence on temperature has semiconductor character. The dependences of the electrical and magnetic parameters of the layers on the Mn content were investigated.

INTRODUCTION

III-V semiconductor compounds are widely used for manufacture of high-speed electronic and optoelectronic devices. Recent field of application for these semiconductors is spintronics. Most known spintronic devices are spin field transistor, spin light-emitting diode and spin valve [1]. Characteristics of spintronic devices may be essentially improve using so-called magnetic semiconductors as alternatives to common metallic ferromagnetics. The magnetic semiconductors exhibit, among classic semiconductor properties, ferromagnetic behavior at temperatures below point of phase transition "ferromagnetic/paramagnetic" (Curie temperature, T_c). It is known that manganese doping of III-V compounds to the concentration of several atomic percent leads to appearance of ferromagnetic properties in these semiconductors. In these conditions, the Mn atoms serve two important functions: they represent uncompensated magnetic moments and acceptors, supplying free holes to valence

band. Electrically active Mn atoms substitute III group atoms in sites of crystalline lattice. The best known examples for magnetic semiconductors are (Ga,Mn)As and (In,Mn)As. Molecular-beam epitaxy is common for fabrication of (III,Mn)V semiconductor layers. The Curie temperatures for (Ga,Mn)As and (In,Mn)As are 110 and ~ 40 K, respectively [2].

Mechanism of ferromagnetism in the (III,Mn)V magnetic semiconductors remains a mystery. Because of this, it is important to compare properties of magnetic semiconductors obtained by different methods.

In this article we present results of investigations of crystal structure, magnetic and galvanomagnetic properties for the magnetic semiconductor (In,Mn)As, obtained by method of pulse laser deposition.

EXPERIMENTAL

The InMnAs layers with the thickness 120 – 270 nm were deposited at 320ºC in horizontal quartz reactor on GaAs (100) semi-insulating substrates. Process was performed in flux of hydrogen and arsine at pressure, which was somewhat lower the atmospheric one. Beam of YAG:Nd pulse laser was introduced into the reactor through the wall and fall on target composed of two parts – metallic Mn and undoped InAs. By changing ratio of the times of periodic sputtering of Mn and InAs {controlled quantity is $Y_{Mn} = t_{Mn}/(t_{Mn} + t_{InAs})$} we varied Mn content in the layers.

Studying the topography with Talysurf CCI 2000 device three-dimensional images of the surface topography and statistic values that characterize roughness of the layer surface (S_a - absolute value of mean deviation, S_q – standard deviation) were obtained.

The crystal quality and phase composition of the layers were studied by X-ray diffraction on a DRON-4 diffractometer with use of $CuK_{\alpha 1}$ radiation.

Magnetization measurements were performed at a room temperature with alternating gradient force magnetometer (AGFM) [3]. The principle of the method is based on the appearance of the force acting on the magnetic moment of the sample under the influence a magnetic-field gradient. A sensitivity of this technique is about 10^{-8} emu. Magnetic field was applied along the sample surface.

The Hall effect measurements were performed in magnetic fields up to 4000 Oe. Hall bar mesa structures, manufactured with the use of photolithography and etching, were implemented. The temperature dependences of the Hall effect were studied in the range 10 - 300 K using the closed-cycle cryostat Janis CCS-300S/202.

RESULTS AND DISCUSSION

Figure 1(a) represents results of topographical study for surface of the InMnAs layer (Y_{Mn} = 0.05). It can see that the surface is reasonably smooth ($S_q \approx 1.6$ nm). Only one elevated feature we observed in the field of vision (0.25 mm^2). The emergence of the large-scale irregularity on the surface is most likely dependent on the quality of the substrate treatment before applying the layers. There is no clear dependence of the roughness on Mn content in the layers, although the maximum value of roughness, S_q = 13 nm, was observed for the sample with maximum (Y_{Mn} = 0.26) Mn concentration.

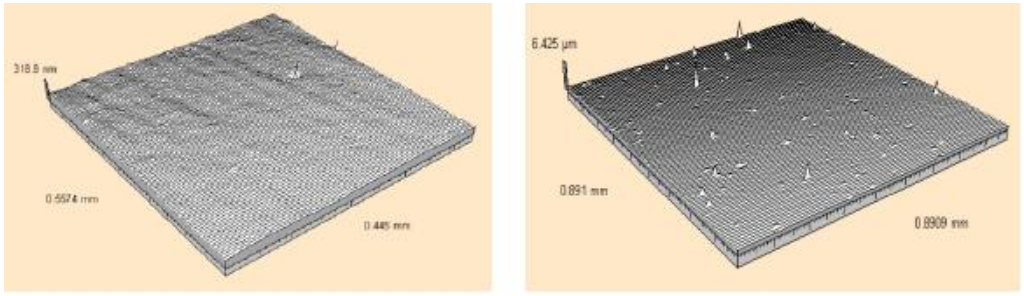

Figure 1. Topography of the surface: (a) InMnAs layer, fabricated in a flow of hydrogen and arsine (S_q = 1.6 nm), (b) GaMnAs layer, obtained by laser pulse deposition in vacuum (S_q = 30 nm).

It is of interest to compare the surface topography of these InMnAs structures with roughness of layers, obtained by laser sputtering in vacuum [4]. Figure 1(b) displays topography of surface for GaMnAs layer, deposited by the laser pulse vacuum deposition. We can see noticeably larger surface roughness (S_q = 30 nm) for GaMnAs layer as opposite to our deposition process. The reason may be that the atoms and clusters of material sprayed as a result of laser pulse action on the target, with significant energy (up to 300 eV [5]), move without collisions in vacuum and are incident on the substrate. This leads to significant damage of the layer and to deposition of atom clusters on surface. During the growth of layers in the flow of the gas-carrier, the particles emitted from the target rapidly lose energy due to collisions with gas molecules, and only the atoms are picked up by the gas and transferred to the substrate. As a consequence, the size of the irregularities on the surface of layers, obtained by laser pulse deposition in gas environment, is acceptable for the manufacture of device structures.

The crystal structure was investigated by X-ray diffraction. Spectra of θ/2θ scanning are presented in Figure 2. A comparison of patterns showed that spectrum for the samples containing InMnAs layer (curves 1 – 3) contains, in addition to the peaks associated with the GaAs substrate ((002) reflection) and InAs layer ((002) reflection) at 31.6 and 29.5°, respectively, maxima which lie close to positions of the peaks related to MnAs hexagonal phase (42.3 and 48.9°). The widths of these additional peaks are ≈ 4°, which is in agreement with the pattern of textured polycrystal. The X-ray diffraction of InMnAs sample as a whole is corresponded with good monocrystal quality of host layer material, which contains some incorporations of second phase (MnAs).

Figure 3 (a) displays dependence of sample magnetization on the applied magnetic field (curve 1). The hysteresis loop is observed in the fields below 1500 Oe. We can see also parts with a negative slope in higher fields. The latter feature characterizes the diamagnetic contribution of the GaAs substrate to the total magnetization. After extraction of the diamagnetic component related to the substrate (linear curve 2) we obtain a usual magnetization curve (curve 3). The saturation magnetization increases with the Mn content from 0.05 to 0.26.

Figure 3 (b) exhibits dependence of coercive field, deduced from untreated data by the subtraction of linear diamagnetic contribution, on the Mn content. The coercive field increases with Y_{Mn} from 70 to 340 Oe in above indicated range of manganese content.

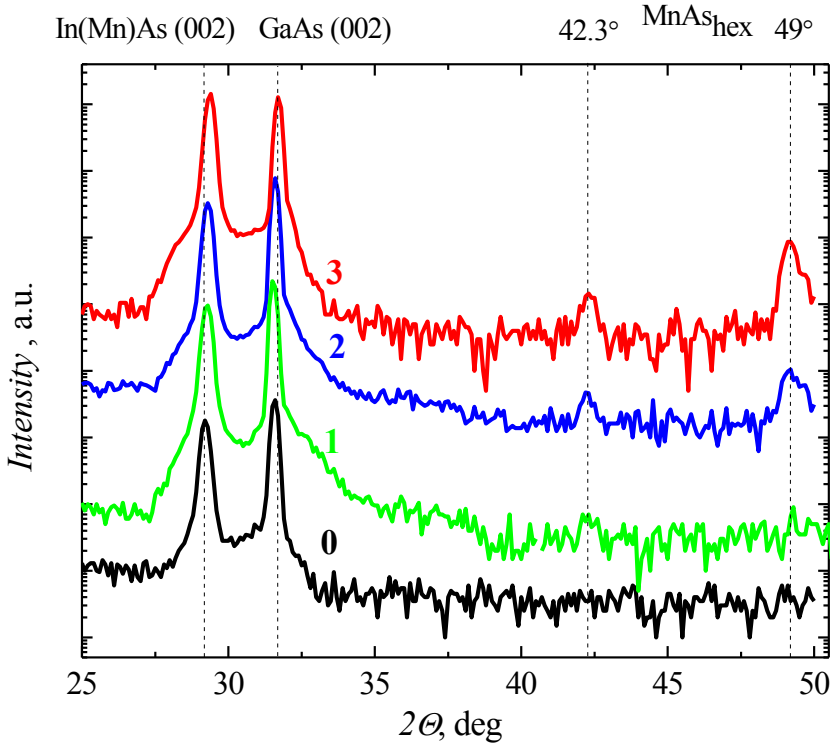

Figure 2. Spectra of the X-ray diffraction for the structures with InAs (curve 0) and InMnAs (curves 1 - 3) layers. Manganese content, Y_{Mn}: 1 – 0.09; 2 – 0.2; 3 – 0.26.

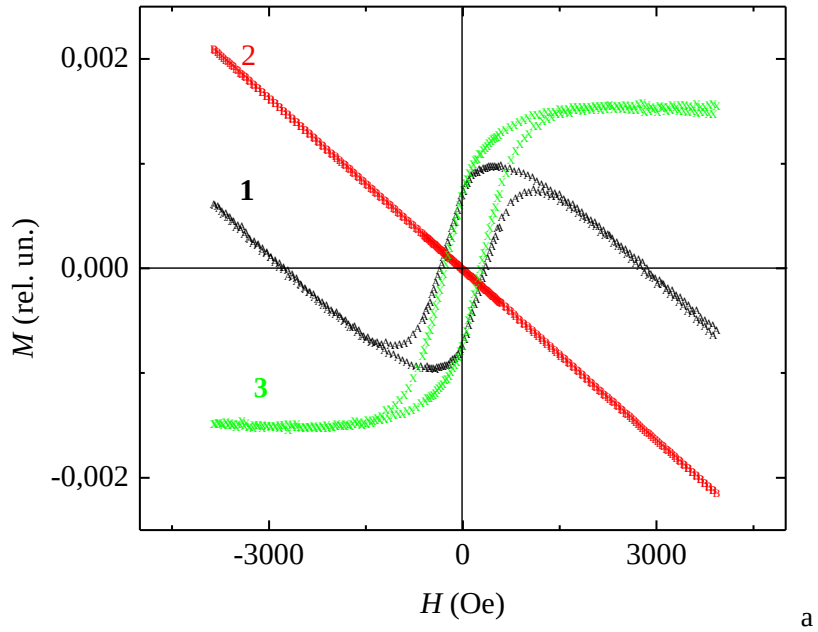

a

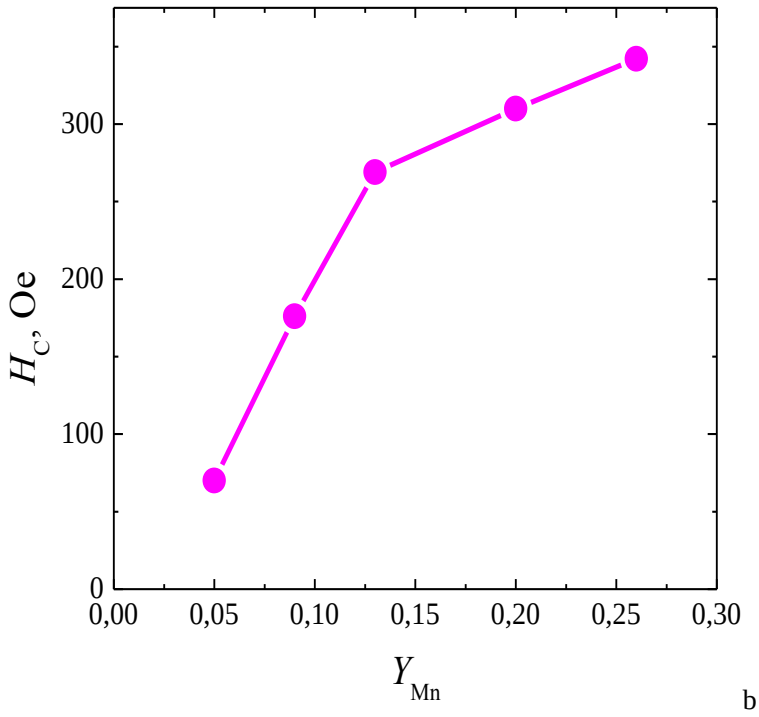

Figure 3. (a) - Magnetic field dependence of magnetization for structures InMnAs with the manganese concentration of Y_{Mn} = 0. 13, obtained by AGFM: 1 - the original experimental curve; 2 - a line that describes the diamagnetic contribution of the GaAs substrate; 3 – curve, corresponding to InMnAs layer (full curve minus diamagnetic signal from the GaAs substrate); (b) - The dependence of the coercive field on the content of manganese in the layers InMnAs.

Hall effect measurements provided following results. The intentionally undoped InAs layer, fabricated by the laser deposition method in use, revealed *n*-type conductivity with electron concentration of $\approx 6 \cdot 10^{17}$ cm^{-3} (at 300 K). Effective electron mobility was equal to 2250 cm^2/V·s (at the same 300 K temperature). This mobility value is ≈ 6 times less than corresponding value for bulk InAs with donor concentration (N_d) of $6 \cdot 10^{17}$ cm^{-3} [6]. Taking into account that electron mobility in InAs can be reduced up to above mentioned value by acceptor compensation with degree value (N_a/N_d) of ≈ 0.5, it may be deduced that laser deposited InAs is reasonably good semiconductor material.

The all Mn-doped InAs layers with Y_{Mn} in range of 0.05 - 0.26 had *p*-type conductivity. This fact is consistent with acceptor behavior of Mn in InAs. Sheet resistance of InMnAs layers was diminished from 3770 to 2200 Ohm/sq with increasing Y_{Mn} value from 0.05 to 0.09. However, further increasing of Mn content led to resistivity build-up (Figure 4a). The reason of similar behavior of resistivity is decreasing of electrical activity of incorporated Mn atoms that can be related to self-compensation of Mn acceptors by Mn interstitials which acts as double donors in InMnAs. Also decreasing of electrical activity of incorporated Mn can occurs if part of manganese spends to formation of MnAs clusters.

An essential feature of electrical properties of InMnAs layers is monotonic increase of resistivity with decrease of temperature (Figure 4a). This obviously points to semiconductor behavior of grown Mn-doped InAs layers.

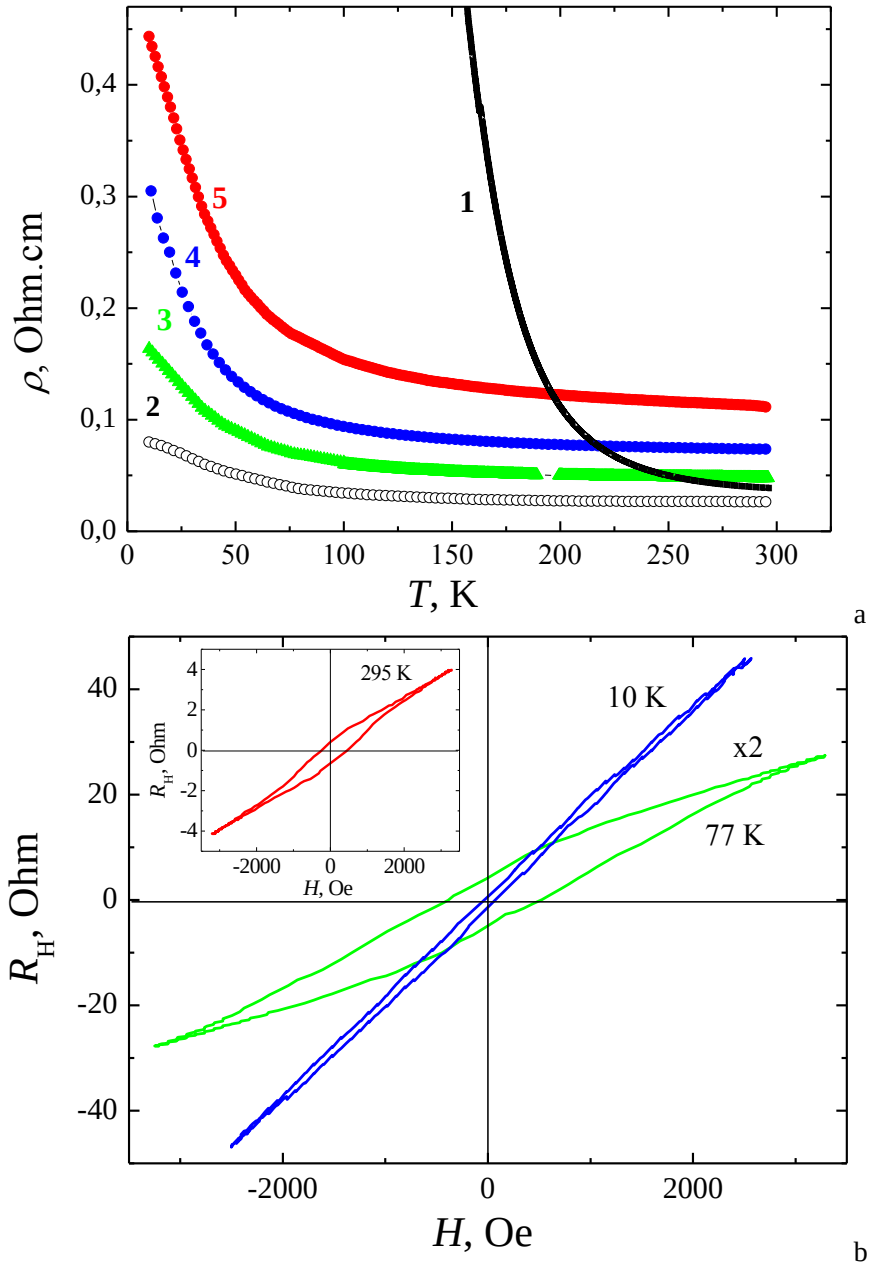

Figure 4. (a) - Temperature dependence of resistivity for InMnAs layers. Manganese content Y_{Mn}: 1 – 0.05; 2 – 0.09; 3 – 0.13, 4 – 0.2, 5 – 0.26; (b) – Dependence of the Hall resistance on magnetic field at 10 and 77 K for the sample with Y_{Mn} = 0.2. The insert shows dependence at 295 K.

Figure 4b shows the Hall resistance dependences on magnetic field applied perpendicular to the surface for InMnAs layer with Y_{Mn} = 0.2. The dependences from 10 to 295 K show clear hysteresis loop. Anomalous Hall effect with hysteresis loop was observed in the samples with Y_{Mn} > 0.05 (at room temperature - in the samples with Y_{Mn} = 0.13 - 0.26).

It is well known that Hall resistance in magnetic films can be is expressed by the follow equation

$$R_H(H) = \frac{R_0 \mu_0 H}{d} + \frac{R_S M}{d}, \quad (1)$$

where the R_0 is a coefficient of ordinary Hall effect, R_S is a coefficient of anomalous Hall effect (AHE), d is film thickness, μ_0 is the vacuum permeability, H and M are magnetic field and magnetization perpendicular to the film plane, respectively.

A separation of Hall resistance into two (normal and anomalous) components provides a means for determination of electrical parameters (hole concentration and Hall mobility) for electronic subsystem of InMnAs layer and magnetic characteristics for magnetic subsystem.

In particular, maximum hole concentration values ($6.4 \cdot 10^{18}$ cm^{-3} at 300 K and $2.8 \cdot 10^{18}$ cm^{-3} at 77 K) were obtained for the InMnAs layer with Y_{Mn} = 0.09. Room temperature Hall mobility values ranged from 95 to 33 $cm^2/V \cdot s$ at the variation of the Y_{Mn} value from 0.05 to 0.26. The 77 K mobility values differed little from one another (63 – 58 $cm^2/V \cdot s$ for Y_{Mn} = 0.09 – 0.26).

In should be note that manifestation of anomalous Hall effect at high temperatures is unusual phenomenon for InMnAs both in single phase and with MnAs inclusion. In particular, for InMnAs layers, grown by molecular beam epitaxy, AHE was observed at temperatures up to 90 K [7].

The InMnAs layers, fabricated by vacuum laser deposition, also demonstrated only low-temperature (< 40 K) anomalous Hall effect behavior [8]. In [9, 10] InMnAs layers were grown at 475 - 530°C by MOCVD epitaxy. Formation of MnAs clusters was not revealed despite high temperature of growth process. Direct measurements of magnetization demonstrated ferromagnetic properties of InMnAs layers up to 330 K. The authors assumed that the ferromagnetic properties of InMnAs layers, grown by MOCVD process, are determined by presence of Mn-Mn dimers.

In our case X-ray diffraction showed formation of second MnAs phase. Cross section transmission electron microscopy investigations on our samples revealed MnAs clusters with dimension of ≈ 20 nm in the vicinity of InMnAs/GaAs interface [11].

We suppose that in our InMnAs layers anomalous Hall effect related to presence of MnAs phase. One of reason for this assumption is the fact, that AHE disappears about 315 K which is close to Curie temperature for bulk MnAs. It is possible that interaction between charge carriers and MnAs inclusions leads to appearance of long-range magnetic order in InMnAs layers.

It is interesting that at low temperatures (< 70 K) in our samples dominates ordinary Hall effect (Figure 4b) that points to reduction of ferromagnetism. This behaviour of magnetic properties with temperature can be explained by disappearance of interaction between free holes and MnAs inclusions due to freezing carriers. This can confirm the assumption about determinative role of MnAs phase in origin of anomalous Hall effect in the InMnAs layers, grown by laser pulse deposition.

CONCLUSIONS

According to direct measurements of the magnetization, the layers InMnAs are ferromagnetic at room temperature since manganese concentrations ≈ 0.05. Some parameters

(for example, coercive field) of the magnetic subsystem were determined. With increasing concentration of manganese, coercive field values increase.

The study of galvanomagnetic properties revealed that layers InMnAs exhibit anomalous Hall effect with a loop hysteresis up to room temperature. The hole concentration and mobility values were calculated from the magnetic-field dependences of the Hall effect. With decreasing temperature the hole concentration decreases, which is typical for the usual semiconductors. With increasing the manganese content from 0.09 to 0.26 the resistance of the layers increases.

Observation of anomalous Hall effect up to room temperature in InMnAs layers is reason for believing that the technique of pulse laser deposition has the capability of producing magnetic semiconductors suitable for spintronics devices.

ACKNOWLEDGMENTS

This work was partially supported by the Presidium of the Russian Academy of Sciences, the Russian Foundation for Basic Research (grant no. 11-02-00645a), the Ministry of education and science of Russia (Federal Program “Development of the Potential of Higher School” (projects no.2.2.2.2/11107 and 2.1.1/12029) and Federal target program «Scientific and scientific-pedagogical personnel of the innovative Russia» in 2009-2013.

REFERENCES

[1] Žutić, I.; Fabian, J.; Das Sarma, S., “Spintronics: Fundamentals and applications”, *Rev. Mod. Physics*, 76, (2004) 323-410.

[2] Matsukura, F.; Ohno, H.; Dietl, T. “III-V Ferromagnetic Semiconductors”, *Handbook of Magnetic Materials.* Ed. Buschow, K.H.J. Elsevier, 14, (2002) 1-88.

[3] Flanders, P.J., “An alternating-gradient magnetometer”, *J. Appl. Phys*., 63(8), (1988) 3940-3945.

[4] Danilov, Yu.A.; Demidov, E.S.; Drozdov, Yu.N.; Lesnikov, V.P.; Podolskii, V.V.; Sapozhnikov, M.V.; Kasatkin, A.P., “Ferromagnetism in epitaxial layers of gallium and indium antimonides and indium arsenide supersaturated by manganese impurity”, *J. Magn. Magn. Mater*., 300, (2006) e24-e27.

[5] Gaponov, S.V.; Kluenkov, E.B.; Strikovskii, M.D.; Churin, S.A., “Effect of the flux-density and energy of laser plasma particleson the structural and electrophysical characteristics of epitaxial GaAs –layers”, *Inorganic Materials*, 25(10), (1989), 1476-1478.

[6] http://www.ioffe.ru/SVA/NSM.

[7] Schallenberg, T.; Munekata, H., “Preparation of ferromagnetic (In,Mn)As with a high Curie temperature of 90 K”, *Appl. Phys. Lett*., 89, (2006) 042507.

[8] Rylkov, V.V.; Aronzon, B.A.; Lagutin, A.S.; Podolsky, V.V.; Lesnikov, V.P.; Goiran, M.; Galibert, J.; Raquet, B.; Leotin, J. “Transport features in laser-plasma-deposited InMnAs layers in strong magnetic fields”, *JETP*, 108(1), (2009) 149-158.

[9] Blattner, A.J.; Wessels, B.W., “Ferromagnetism in (In,Mn)As alloy thin films grown by metalorganic vapor phase epitaxy”, *Appl. Surf. Sci*., 221, (2004) 155-159.

[10] Wessels, B.W., "Ferromagnetic semiconductors and the role of disorder", *New J. Physics*, 10, (2008) 055008.

[11] Gan'shina, E.A.; Golik, L.L.; Kovalev, V.I.; Kun'kova, Z.E.; Temiryazev, A.G.; Danilov, Yu.A.; Vikhrova, O.V.; Zvonkov, B.N.; Rubacheva, A.D.; Tcherbak, P.N.; Vinogradov, A.N.; Zhigalina O.M., "Resonant enhancement of the transversal Kerr effect in the InMnAs layers", *J. Phys.: Condens. Matter*, 22, (2010) 396002.

Smart Nanocomposites
Volume 2, Number 1
ISSN: 1949-4823

SMART TITANIUM DIOXIDE NANOCOMPOSITES FOR CELLULAR DELIVERY OF THE ANTISENSE PEPTIDE NUCLEIC ACIDS

Rinat N. Amirkhanov, Valentina F. Zarytova and Nariman V. Amirkhanov*

Institute of Chemical Biology and Fundamental Medicine,
Novosibirsk 630090, Russia

ABSTRACT

Peptide nucleic acids (PNAs) are one of the promising antisense drugs for the gene therapy. PNAs are DNA mimics with the peptide-like backbone [1]. PNAs form the most stable complementary duplexes with RNA among all known modified and non-modified oligonucleotides and have high exo- and endonuclease resistance [2, 3]. However, PNAs themselves cannot penetrate through cellular membranes [4]. Here we propose to use nanocomposites based on titanium dioxide (TiO_2) nanoparticles for the delivery of PNAs into living cells.After delivery of antisense PNA drugs into the cells there is still a problem with PNA molecules release from nanocomposite vehicles in cytoplasm inside of cells. Here we designed special nanocomposites on the basis of TiO_2 nanoparticles (4-6 nm in diameter) containing the hybrid PNA\DNA duplexes. The attachment of PNA\DNA duplexes to nanoparticles preliminary covered with polylysine (PL) occurs due to the electrostatic interaction between negatively charged internucleotide phosphate groups of DNA and positively charged amino groups of polylysine. It was demonstrated that the resulted TiO_2/PL/DNA/PNA nanocomposite can be delivered into the cells. Dissociation or release time of PNA from the DNA/PNA duplex attached to the nanocomposite was measured and easily could be regulated with the length of the overlap of complementary base pairs in the initially constructed DNA/PNA duplexes in nanocomposite TiO_2/PL/DNA/PNA. Thus, PNA/DNA complex with optimal overlap number or optimal half-release time of PNA from nanocomposite allows at least the half quantity of PNA still to remain in TiO_2/PL/DNA/PNA nanocomposite during the delivery and then able to be released from the nanocomposite after its delivery inside of the cells. These features of the constructed nanocomposites were demonstrated on the example of nanocomposites containing various overlap length of DNA/PNA duplexes (from 10 to 16 base pairs). It was found that the time of half-release of PNA from these TiO_2/PL/DNA/PNA nanocomposites changed from 10 to 70 min depended on overlap length of DNA/PNA duplexes in conditions close to physiological (35^{o}C in PBS buffer, pH 7.5). The greater the overlap of the DNA/PNA duplex in nanocomposite

* To whom correspondence should be addressed. E-mail: nariman@niboch.nsc.ru

TiO_2/PL/DNA/PNA, the longer the time of PNA release from this nanocomposite. Thus, the adjustable reversible method of PNA immobilization on TiO_2 nanoparticles was developed. Created PNA containing nanocomposites were capable to penetrate cell membranes without transfectants or other adverse procedures.

Keywords: TiO_2 nanoparticles, nanocomposites, polylysine, PNA, cell delivery, immobilization, release kinetics, poration mechanism, endosome escape.

INTRODUCTION

Design and construction of nanocomposites based on nanoparticles as vehicles for drug delivery of antisense oligonucleotides (AONs) into cells is relevant problem to molecular biology and modern medicine. Antisense technologies can be employed for genotherapy, which is based on the interaction of AONs with pathogenic nucleic acid (NA) target inside the cells [5] resulting in the arrest of a certain target and thereby in the prohibition of the expression of undesirable genes. Nevertheless, despite the promising progress of antisense technology there are still not any meaningful antisense drugs which have been manufactured after more than 40 years since the first publication of the idea [6]. The general obstacle is the absence of the effective and non-toxic methods for the delivery of AONs into the cells.

It was previously found that the titanium dioxide nanoparticles (TiO_2) can penetrate into eukaryotic cells [7]. Because of very small nano-sizes (5-50 nm in diameter) of nanoparticles they can penetrate through cell membranes by mechanism of poration without overt membrane disruption and damage of the cells [7]. Accordingly to literature data, the optimal size of the nanoparticles should not be more than 5-6 nm [8, 9]. In this case nanoparticles can cross the cell membrane by a direct mechanism — a route that delivers them to the main compartment of the cell without trapping them in endosomes while leaving the membrane undisrupted [8, 9]. *Poration mechanism* means penetrating of the particles through cell membranes by forming in the membrane a microscopic holes or pores due to high kinetic energy of the nanoparticles. For example, electroporation mechanism means penetrating of biomacromolecules by making holes in membrane with electric current. Nanoparticles like microscopic nano-bombs or nano-bullets attack and pierce the membrane making microscopic pinholes in membrane and go on inside of cell. If this energy is too high the cell membranes or cells themselves will be damaged irreversibly. If this energy is too low the particles cannot make the pores or pinholes in the membrane and typically will be internalized by cells into membrane-bound endosomes and fail to access the cytosolic cell machinery. In the case of TiO_2 nanoparticles they also can form micro or nanoholes in membranes by chemically oxidizing them with water-oxygen-hydroxyl radicals due to strong oxidation-reduction ability of TiO_2 particles themselves [7]. We assumed that nanosized TiO_2 particles can be used as vehicles for cellular delivery of the gene-directed drugs - antisense nucleic acids - with mechanism of poration excluding the capsulation them in endosomes and without necessity to escape from endosomes when they are already inside the cells.

Zeta potential of the surface of TiO_2 nanoparticles usually is negative at pH 7-8 at the physiological conditions [10]. This feature of the TiO_2 nanoparticle surface enables to attach positively charged polylysine (PL) molecules on the surface with very strong efficiency. Then the single or double stranded AON or siRNA molecules can be attached to the surface of such

polylysine modified TiO_2 nanoparicles to yield TiO_2/PL/AON or TiO_2/PL/siRNA nanocomposite. In principle, such TiO_2/PL/AON(siRNA) nanocomposites prospectively can be used as vehicles for cellular delivery of AONs or siRNAs.

Unfortunately, there is no way to release the free AON or siRNA molecules from the TiO_2/PL/AON(siRNA) composites in physiological conditions after their delivery into the cells because of very strong electrostatic interaction between positively charged TiO_2/PL composite and negatively charged DNA (or RNA) antisense oligonucleotides or siRNA molecules.

Usually antisense DNA or RNA is 20-25 nucleoside bases in the length and correspondingly has 20-25 negatively charged internucleotide phosphate residues. Such strong electrostatic interactions can be destroyed only with high ionic forces in high salt concentration (more then 1 M NaCl) or at very high or very low pH conditions (pH>10 or pH<3, which is much more or much less than physiological pH 7-8). Such conditions can be created artificially but cannot be reached or created inside of the cells. Thus DNA, RNA or siRNA molecules even after successfully delivery them into the cells cannot be released and cannot be able to interact with their nucleic acid or gene targets inside of the cells because of their unavailability to these targets. Moreover, the direct interaction between TiO_2/PL/AON nanocomposite and target mRNA might be unspecific because the specific Watson-Crick interaction between DNA or RNA antisense oligonucleotides and target mRNA is forced with unspecific electrostatic interactions between positively charged residues of PL and negatively charged internucleotide phosphate groups of the target mRNA.

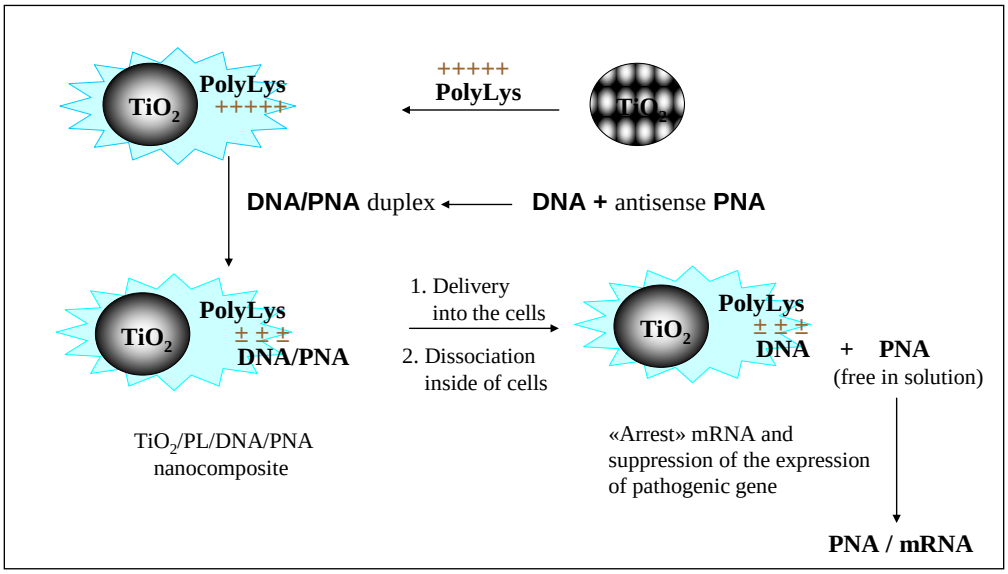

Figure 1. Design of TiO_2/PL-DNA/PNA nanocomposites as vehicle for delivery of antisense PNA molecules into the cells. PNA was reversibly immobilized to TiO_2 nanoparticles. In cytoplasm PNA molecules can be released from nanocomposite and interact with pathogenic mRNA inside the cells.

One of the ways of this problem solution might be using uncharged analogues of nucleic acids such as peptide nucleic acids (PNAs) [1]. PNAs are DNA mimics with the pseudo peptide backbone [1]. Unlike DNAs, PNAs do not have negatively charged sugar-phosphate

backbone and form more stable complementary duplexes with nucleic acids and have a high resistance to nucleases [2, 3]. These features make the PNAs the promising antisense and antigene drugs. However, PNAs themselves cannot penetrate through cellular membranes [4].

Here we propose to use nanocomposites based on TiO_2 nanoparticles containing PNA/DNA duplexes for PNA delivery into the cells (Figure 1). The attachment of the hybrid PNA/DNA duplexes to nanoparticles covered with polylysine occurs due to the electrostatic interaction between negatively charged internucleotide phosphate groups and positively charged amino groups in polylysine. We hypothesize that the resulted TiO_2/PL/DNA/PNA nanocomposite can be delivered into the cells followed by dissociation of the PNA from the duplex. The dissociated PNA then will bind to pathogen mRNA.

EXPERIMENTAL SECTION

TiO_2 nanoparticles were prepared by the low-temperature controlled hydrolysis of $TiC1_4$ (by dropwise addition of titanium(IV) tetrachloride to water cooled to 4°C) [11, 12]. The size of the TiO_2 nanoparticles prepared in these conditions is 4-6 nm [11]. Theoretically 4.5 nm-sized nanoparticles of TiO_2 consist of about 1,500 TiO_2 molecules per particle [13]. Thus we calculated and assumed that 1 mg of our prepared TiO_2 nanoparticles is equal to 8.3 nmoles of particles. Electron diffraction examination of TiO_2 particles prepared in these conditions shows that the only crystalline phase present is anatase [11, 12].

TiO_2/PL nanocomposite with molar ratio 1:2 of TiO_2 particles to PL was prepared by mixing of 0.2 ml of suspension of TiO_2 particles (5 mg/ml, 8.3 nmole/mg, 1 mg, 8.3 nmoles) and 0.084 ml of 0.2 mM poly-L-lysine Hydrobromide (Sigma Aldrich P7890, USA, average mol wt 22,700; 4.5 mg/ml, 0.38 mg, 16.6 nmole), in water or PBS, pH 7.4. Excess of unbound polylysine was removed by centrifugation and washing nanoparticles with PBS. TiO_2/PL nanoparticles then were suspended in water or PBS. The effectiveness of the binding of polylysine to TiO_2 particles was tested by immobilization of radioactive or non-radioactive DNA oligonucleotide to prepared TiO_2/PL composite. The number of bound oligonucleotides per particle was determined from the change in the optical absorption in the solution after adding TiO_2/PL particles and centrifugation. Typically, the change in the absorption after binding was consistent with about one or two bound oligonucleotides per particle (10-15 nmole of DNA per 1 mg of TiO_2 nanoparticles). Control unmodified TiO_2 nanoparticles bound only 0.5-1 nmole of DNA oligonucleotide per 1 mg of TiO_2 nanoparticles.

TiO_2/PL-DNA/PNA nanocomposite was prepared with the use of fluorescein (Flu) labeled PNA (Flu-PNA) by mixing of TiO_2/PL composite with preliminary prepared Flu-PNA/DNA hybrid duplex. Briefly 20 µl of TiO_2/PL suspension (TiO_2: 1 mg/ml, 8.3 nmole/ml, 20 мкг, 0.17 nmole; PL: 16.6 nmole/ml, 7.5 мкг, 0.33 nmole) in PBS mixed with 25 µl of PBS and incubated with 5 µl of 50 - 100 µM preliminary prepared Flu-PNA/DNA duplex in PBS for 5-10 min at 0^oC. The number of bound PNA per particle was determined from the change in the fluorescence activity in solution after adding TiO_2/PL particles and centrifugation. Typically, the change in the absorption after binding was consistent with 8-10 nmole of the bound Flu-PNA per 1 mg of TiO_2 nanoparticles. Control unmodified TiO_2 nanoparticles bound only 1-2 nmole of Flu-PNA/DNA duplex per 1 mg of TiO_2 nanoparticles.

Kinetic of PNA Dissociation from TiO_2/PL/DNA/PNA Nanocomposite Complex

For kinetic experiments TiO_2/PL/DNA/PNA nanocomposites with 5'-end fluorescein labeled Flu-PNA and 5'[^{32}P]-end radioactive labeled p*DNA was used. Series of 50 µl of TiO_2/PL/p*DNA/Flu-PNA nanocomposite probes (TiO_2: 20 мкг, 0.17 nmole, PL: 0.33 nmole, p*DNA: 0.24 nmole, Flu-PNA: 0.35 nmole) were diluted with 500 µl of preliminary heated (35oC) PBS and incubated for defined time (usually from 0 to 180 min) at 35ºC. After specified time each probes were immediately centrifuged (1 min at 14,000 rpm), and supernatant was separated from precipitate. Then radioactivity of DNA and fluorescence of Flu-PNA in supernatant was measured. From these date the percentage of unbound radioactive DNA oligonucleotide or percentage of dissociated fluorescent Flu-PNA was determined. Total radioactivity or fluorescence applied to the sample was taken for 100%. Finally the kinetic curves of the Flu-PNA dissociation from TiO_2/PL/p*DNA/Flu-PNA nanocomposite complex or PNA release kinetic diagram was drown. Some background level of radioactivity or fluorescence (about 30-50%) could be observed in the zero time point of the kinetic curves because of 1.5 – 2 times excesses of p*DNA and Flu-PNA was taken for preparing of TiO_2/PL/p*DNA/Flu-PNA nanocomposite complex.

RESULTS AND DISCUSSION

Initially for preparing of the TiO_2/PL/DNA/PNA nanocomposites, TiO_2 particles were covered by polylysine resulting in the formation of TiO_2/PL composite (Figure 1). Then the preformed PNA/DNA duplex was attached to the TiO_2/PL nanocomposite through electrostatic interaction between negatively charged phosphate groups of DNA and positively charged amino residues of polylysine. Binding PNA to DNA was based on Watson-Crick interactions between complementary bases in the hybrid PNA/DNA duplex.

The formation of TiO_2/PL/DNA/PNA nanocomposites was verified with the use of fluorescein (Flu) labeled PNA (Flu-PNA). For this purpose the preformed DNA/Flu-PNA duplex was mixed with the preliminary prepared TiO_2/PL composite. Then the formation of TiO_2/PL-DNA/Flu-PNA nanocomposites was confirmed by laser fluorescence confocal scanning microscopy (Figure 2).

For cell tracking of PNA molecules in composition of TiO_2/PL-DNA/PNA nanocomposite, PNA molecules were labeled with near infrared fluorescent dye (NIR664). Then TiO_2/PL-DNA/NIR-PNA nanocomposite was incubated with HeLa cells during 24 h, cells then were washed with cell culture media from excess of unbound particles for another 24 h and finally cell without fixation on slides were imaged with laser confocal microscopy. Nuclei of HeLa cells before imaging were stained with the blue-fluorescent *Hoechst* 33342 dye and cytosol was stained with the green-fluorescent *Cell Tracker Green* (Figure 3). As one can see from the Figure 3 all red color exactly overlaps with the green color, which definitely indicates that all PNA molecules concentrated exact inside the cells.

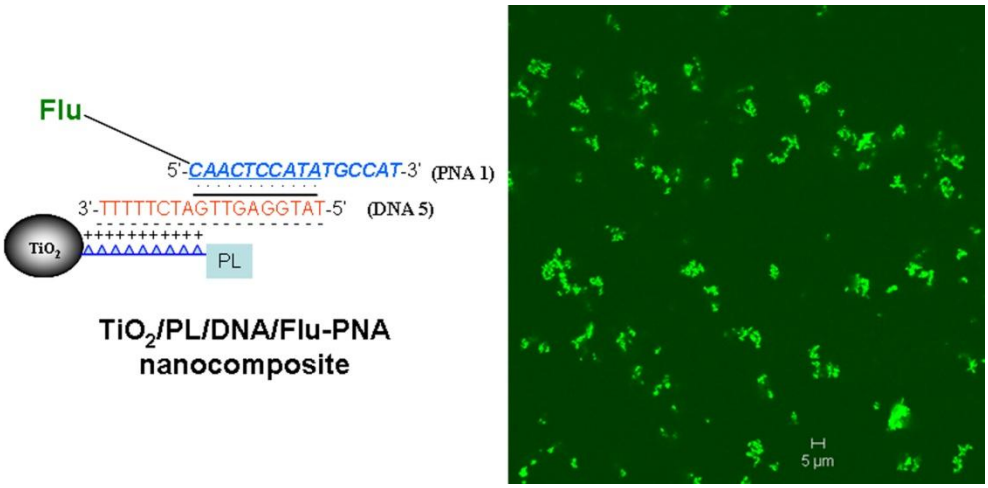

Figure 2. Laser confocal microscopy of TiO_2/PL-DNA/Flu-PNA nanocomposites: Concentrations of TiO_2 particles and PNA/DNA duplex are 0.2 mg/ml and 2 µM, respectively, in the buffer containing 0.14 M NaCl, 0.01 M phosphate, pH 7.5. Laser confocal microscopy was carried out using laser scanning microscope LSM 510 META (Zeiss, Germany). DNA bound to PL through electrostatic interactions (shown in the scheme in the left as "-" and "+"). PNA was bound to DNA through complementary Watson-Crick interactions (shown in the scheme as points).

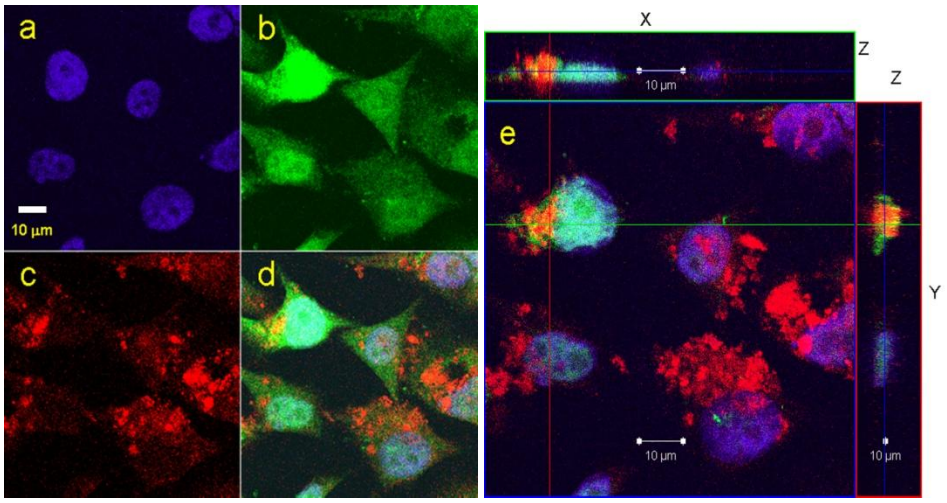

Figure 3. Laser confocal microscopy of HeLa cells treated with TiO_2/PL-DNA/NIR-PNA composite after incubation for 24 h followed by 24 h washing. Concentrations of TiO_2 particles and PNA/DNA duplex are 0.2 mg/ml TiO_2, 2 µM PNA/DNA, respectively, in 0.01 M Tris-HCl, 0.14 M NaCl, pH 7.5: a) nuclei were stained with the blue-fluorescent *Hoechst* 33342 dye; b) cytosol was stained with the green-fluorescent *Cell Tracker Green;* c) PNA contained the red-fluorescent dye *Near Infra Red (NIR-664);* d) overlay of a, b and c; e) overlay of a, b and c and 3D (X,Y and Z) sections.

There is no any red color outside of cells (outside of green color). Assuming that this is a confocal image with very thin slice (300 nm) and size of nuclei is about 10 µm and all slices

were obtained by cutting of the nuclei in the middle, certainly one can conclude that PNA molecules located inside the cells. Thus, PNA molecules in composition with TiO_2/PL-DNA/PNA nanocomposite were shown to penetrate through the eukaryotic cell membranes and accumulate inside cells without using a transfectant (Figure 3).

The possibility of PNA release from TiO_2/PL/DNA/PNA nanocomposite was demonstrated by using 5'-end fluorescein labeled Flu-PNA and 5'[^{32}P]-end radioactive labeled p*DNA. The release kinetics with various DNA/PNA duplexes were conducted at 35ºC that is at conditions close to physiological one. Before the kinetic starting the initial TiO_2/PL/DNA/PNA probes were prepared and kept as concentrated solution in low temperature at 0^{o}C. Then probes were quickly diluted in preliminary heated buffered solution at 35ºC. Here is important to mention that the binding between PNA and DNA in constructed TiO_2/PL/DNA/PNA nanocomposites is based on Watson-Crick interactions between complementary bases in the hybrid PNA/DNA duplex. Exactly because of complementary binding of DNA and PNA in the TiO_2/PL/DNA/PNA nanocomposite complex, PNA in this case had a great possibility to be released from the complex after dilution or changing temperature due to shift of complex association/dissociation equilibrium.

The typical dynamics of the Flu-PNA release from TiO_2/PL/p*DNA/Flu-PNA nanocomposite is presented in Figure 4. One can see that there is an increase of fluorescence in solution; however the level of radioactivity in the solution remains constant. These data testify that only Flu-PNA is released in solution, with p*DNA remaining in nanocomposite. Thus, it confirms that the release of PNA from nanocomposite induces with dissociation of p*DNA/Flu-PNA duplex in TiO_2/PL/p*DNA/Flu-PNA nanocomposite. That means that the time of PNA release from TiO_2/PL/DNA/PNA nanocomposite can be regulated with the altering of thermostability of the DNA/PNA duplex or by the changing of the base pair overlap length in the duplex. Utilizing this concept, four different DNA/PNA duplexes P1, P2, P3, and P4 containing various number of overlapping complementary base pairs (10, 12, 14, and 16) and, thereby, having the different thermostability (Table 1) were investigated. The time of half-release or time of half-dissociation ($\tau_{1/2}$) of PNA from TiO_2/PL/DNA/PNA nanocomposites was found for each of DNA/PNA duplexes P1, P2, P3, and P4 (Table 1). Table 1 and Figure 5 demonstrate that the $\tau_{1/2}$ values increase as well as with rising the duplex stability.

Table 1. Structure of PNA/DNA duplexes having various overlap length and thermostability

Duplex	Oligonucleotides	Structure of duplexes*	Overlap length, b.p.	T_m, ºC	$\tau_{1/2}$, min on TiO_2 particles
P1	PNA1 DNA5	5'-*CAA CTC CAT ATG CCA T*-3' 3'-pTTT TTC TAG TTG AGG TAT-5'	10	51.0	10.6
P2	PNA1 DNA6	5'-*CAA CTC CAT ATG CCA T*-3' 3'-TTT TTC TAG TTG AGG TAT AC-5'	12	60.5	14.1
P3	PNA1 DNA7	5'-*CAA CTC CAT ATG CCA T*-3' 3'-TTT TTC TAG TTG AGG TAT ACG G-5'	14	72.2	22.2
P4	PNA1 DNA4	5'-*CAA CTC CAT ATG CCA T*-3' 3'-CTA GTT GAG GTA TAC GGT ACA T-5'	16	73.8	70.7

*Used DNA and PNA oligonucleotides were with initially arbitrary sequences.

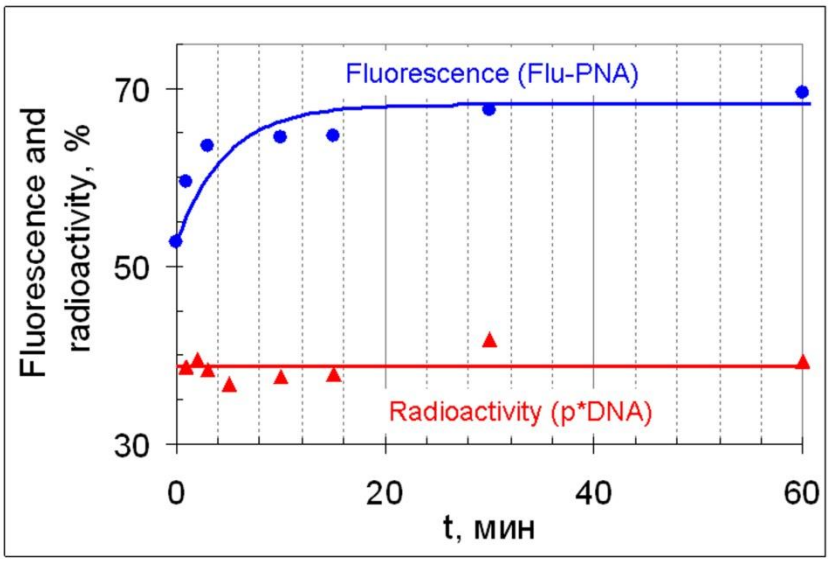

Figure 4. Kinetic curve of the Flu-PNA release from TiO_2/PL/p*DNA/Flu-PNA nanocomposite.

It was found that the time of half-release of PNA from these TiO_2/PL/DNA/PNA nanocomposites increases from 10 to 70 min depends on the overlap length of DNA/PNA duplexes (Figure 5). These date demonstrate that the changing of the PNA/DNA duplex stability allows to change the retention time of PNA in TiO_2/PL-DNA/PNA nanocomposites and, consequently, to control efficiency of PNA delivery into cell in the form of TiO_2/PL/DNA/PNA nanocomposite.

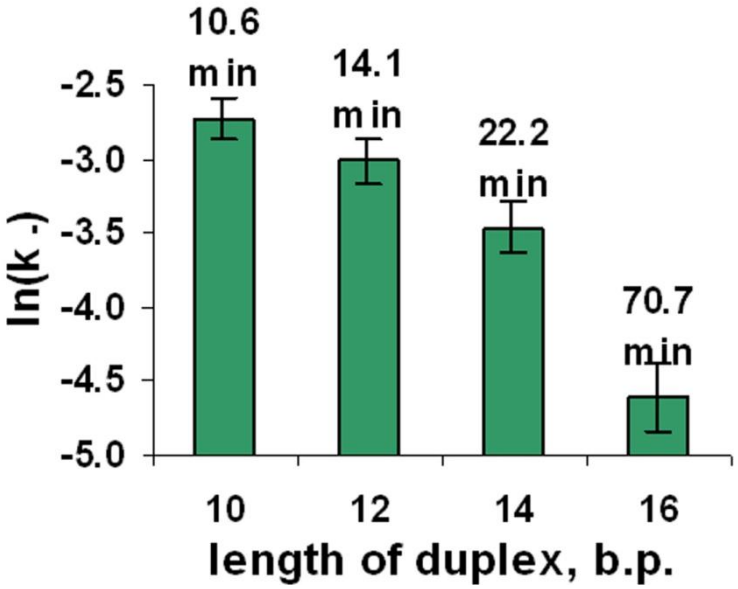

Figure 5. Dependence of PNA dissociation rate constant (ln(k -)) from TiO_2/PL-DNA/PNA nanocomposites complex on the number of complementary base pairs in DNA/PNA duplexes at 35^0C in 0.01 M Tris-HCl, 0.14 M NaCl buffer (error ±10 %).

CONCLUSIONS

We demonstrated that the PNA release rate from the TiO_2/PL-DNA/PNA nanocomposite could be easily regulated by changing the number of complementary base pairs in the duplex. It promoted the reversible and controllable PNA immobilization on TiO_2 particles. PNA molecules in TiO_2/PL-DNA/PNA nanocomposite were shown to penetrate through eukaryotic cell membranes and accumulate inside cells without using a transfectant. Thus, for the first time, we developed the reversible and controllable method of the PNA immobilization on nanoparticles and created PNA-based nanocomposites which capable to penetrate cell membranes without transfectants or other adverse procedures. Kinetic data and results obtained in this work can be useful for design and construction of nanocomposites with optimal DNA/PNA base pars overlap not only based on TiO_2 as well as many other nanoparticles widely used recently as drug delivery cargos.

In conclusion it is necessary to note that titanium dioxide is non-toxic and approved by the food testing laboratory of the United State Food and Drug Administration (FDA) in 1966. TiO_2 is considered to be a safe substance, and is harmless to human. It is commonly used in foodstuffs, domestic commodities, cosmetics and cultivation. Moreover, recently it was found that TiO_2 nanoparticles at low doses (up to 200 μg/mL) had no measurable toxic effect on the mammalian cells [14], bacteria [15] or animals [16]. In summary, all these date allow to anticipate a promising future for using TiO_2 nanoparticles as antisense nucleic acids drug delivery system.

ACKNOWLEDGMENTS

Authors acknowledge Dr. Sergey I. Baiborodin from Institute of Cytology and Genetics, SB RAS for his assistance in fluorescent confocal microscopy. This research was supported by the Siberian Branch of the Russian Academy of Science under the Integration grant programs (grant No. 61), Russian Foundation for Basic Research (grant No. 08-04-01045-a).

REFERENCES

[1] Nielsen, P. E. *Peptide Nucleic Acids: Protocols and Applications*. (2nd Edition). Ed. by P.E. Nielsen – horizon bioscience, 2004.

[2] Demidov, V.V., Potaman, V.N., Frank-Kamenetskii, M.D., Egholm, M., Buchard, O., Sönnichsen, S.H., Nielsen, P.E. Stability of peptide nucleic acids in human serum and cellular extracts. *Biochem. Pharmacol*. 1994, 48, 1310-1313.

[3] Hamilton, S.E., Iyer, M., Norton, J.C., Corey, D.R. Specific and nonspecific inhibition of transcription by DNA, PNA and phosphorothioate promotor analog duplexes. *Bioorg. Med. Chem. Lett*. 1996, 6, 2897-2900.

[4] Corey, D.R. Calcium liberates PNAs from endosomes. *Cancer Chem. Biol*. 2005, 12, 864-865.

[5] Kurreck J. (2003) Antisense technologies. Improvement through novel chemical modifications. *Eur. J. Biochem*. 270, 1628–1644.

[6] Belikova, A.M., Zarytova, V.F., Grineva, N.I. Synthesis of ribonucleosides and diribonucleoside phosphates containing 2-chloroethylamine and nitrogen mustard residues. *Tetrahedron Lett*. 1967, 37, 3557-3562.

[7] Cai, R., Hashimoto, K.. Itoh, K., Kubota, Y., and Fujishima, A. Photokilling of malignant cells with TiO_2 powder. *Bull. Chem. Soc. Jpn*. 1991, 64, P. 1268-1273.

[8] Xia, T., Rome, L., Nel, A. *Particles slip cell security. Nat. Mater.* 2008, **7**, P. 519 – 520.

[9] Verma, A., Uzun, O., Hu, Y., Hu, Y., Han, HS., Watson, N., Chen, S., Irvine, D.J., Stellacci, F. Surface-structure-regulated cell-membrane penetration by monolayer-protected nanoparticles. *Nat. Mater*. 2008, 7, 588–595.

[10] Kotsokechagia, T., Cellesi, F., Thomas, A., Niederberger, M., Tirelli, N.. Preparation of ligand-free TiO_2 (anatase) nanoparticles through a nonaqueous process and their surface functionalization. *Langmuir* 2008, *24*, 6988-6997.

[11] Serpone, N., Lawless, D., Khairutdinovt, R. Size effects on the photophysical properties of colloidal anatase TiO_2 particles: size quantization or direct transitions in this indirect semiconductor? *J. Phys. Chem.* 1995, 99, 16646-16654.

[12] Liu, J., Garza, L Zhang L., Dimitrijevic, N. M., Zuo X., Tiede, D. M., Rajh, T. Photocatalytic probing of DNA sequence by using TiO_2/dopamine-DNA triads. *Chemical Physics.* 2007, 339, 154–163.

[13] Paunesku, T., Rajh, T., Wiederrecht, G., Maser, J., Vogt, S., Stojicevic, N., Protic, M., Lai, B., Oryhon, J., Thurnauer, M., Woloschak, G. Biology of TiO_2-oligonucleotide nanocomposites. *Nat. Mater.* 2003, 2(5), 343-346.

[14] Jeng, H.A., Swanson, J. Toxicity of metal oxide nanoparticles in mammalian cells. *J. Environ. Sci. Health A Tox Hazard Subst. Environ. Eng*. 2006; 41(12), 699-711.

[15] Heinlaan, M., Ivask, A., Blinova, I., Dubourguier, H. C., Kahru, A. Toxicity of nanosized and bulk ZnO, CuO and TiO2 to bacteria Vibrio fischeri and crustaceans Daphnia magna and Thamnocephalus platyurus. *Chemosphere*. 2008, 71(7), 1308-1136.

[16] Liu, H., Ma, L., Zhao, J., Liu, J., Yan, J., Ruan, J., Hong, F. Biochemical toxicity of nano-anatase TiO2 particles in mice. *Biol. Trace Elem. Res.* 2009, 129(1-3), 170-180.

Smart Nanocomposites
Volume 2, Number 1
ISSN: 1949-4823

EXTENDED CONTINUUM APPROXIMATION FOR SHORT-RANGE INTERACTIONS OF NANOSCALE OBJECTS: PART I: THE ONE-DIMENSIONAL CASE

S. M. Balashov
Center for Information Technology Renato Archer – CTI,
Campinas, San Paulo, Brazil

ABSTRACT

New closed form expression for the potential of single atom interacting by Lennard-Jones potential with the finite set of atoms situated on the straight line in the continuum approximation is presented. The developed expression has better accuracy then based on the same approach traditional one, because continuum integral is compared with the discreet sum of parabolic approximation. It is shown that the proposed potential gives better accuracy in the region of the edges of straight line, the region where classic continuum approach gives poor approximation. The proposed potential can be used for simulation of dynamics of such objects as carbon nanotubes, graphene flakes, Langmuir-Blodgett films etc.

INTRODUCTION

Modeling of the behavior of such phenomena as absorption of atoms on the surface of the carbon nanotube or graphene [1], ordering of hydrocarbon chains in the Langmuir-Blodgett monolayer [2] or vibration of the single nanotube in the bundle of nanotubes [3] are based on the calculation of potential of interaction between different parts of such systems. For nanoscale objects short range Van der Waals forces play significant role in such calculations. To account for these forces the real atom (or group of atoms) is substituted by the force center – the point size object which interacts with the other objects by means of Lennard-Jones potential (LD-potential)

$$P_{m,n}(r) = 4\varepsilon\left\{\left(\frac{\sigma}{r}\right)^m - \left(\frac{\sigma}{r}\right)^n\right\} \tag{1}$$

where r – is the distance between interacting force centers. Physical meaning of other parameters can be found elsewhere [4]. General problem of such calculations is the necessity to summarize energy of interaction of big number of force centers. There are two main approaches for this summation. The first one is based on numerical summation over all force centers [5, 6]. This approach is similar to computer modeling of molecular structures. Normally it is necessary to use special software package and have substantial computer power [6, 7]. The advantage of this approach is that it is possible to analyze topologically complex structures. Another approach discussed in this article is so called continuum approach [1, 2, 8]. It is successfully used for one dimensional [2] and two dimensional cases [1, 8]. The advantage of this approach is that it gives closed form expression for energy of interaction of the entire set of force centers. This allows one to develop thermodynamic of such systems [9], calculate frequencies of vibration of nanoobjects [3], predict tilt angles of hydrocarbon chains in monolayer [2] etc.

The present paper addresses the problem of accuracy of using of the continuum approximation. It is shown that for successful use of it is necessary to modify the procedure of transformation of discreet sum into the integral. New closed form expression for energy of interaction of absorbed atom with the infinite hydrocarbon chain with improved accuracy is proposed. It is shown that, in contrast to previously developed procedures, the proposed expression gives more precise approximation in the area near to the edges of the hydrocarbon chain, which makes it suitable for analysis of absorption phenomena.

I. INTERACTION OF THE SEPARATE FORCE CENTER WITH THE SEMI-INFINITE FORCE LINE

Consider the separate force center (SFC) which interacts with the semi-infinite set of equally spaced force centers situated in the straight line by LD-potential (Figure 1). We call this set of force centers the semi-infinite force line (SFL). Energy for such interaction can be expressed as a function of the distance between the SFC and the SFL $\vec{p}$ and characteristic angle (CA) θ. The alternative pair of variables is the distance between the SFC and the first force center in the SFL $\vec{R}$ and θ.

Using (1) LD-potential of two interacting force centers can be written in the form

$$V_{m,n} = 4\varepsilon(\sigma^{2m}W_m - \sigma^{2n}W_n) \tag{2}$$

where

$$W_n = \sum_{k=0}^{\infty} \frac{1}{(\vec{r}_k)^{2n}} \tag{3}$$

The summation in (3) is taken over positions of all force centers in the SFL. It can be easily shown that

$$(\vec{r}_n)^2 = R^2 + 2Bn + n^2 d^2 \tag{4}$$

where

$$B = \vec{R}\frac{\vec{d}}{|\vec{d}|} = R\cos(\theta)$$

In accordance with the continuum approach the sum in (3) should be turned into integral substituting discreet variable *n* by the continuous variable *x*. This can be done using the transformation $d \to dx$ and $nd \to x$ [2]. After such transformation the sum (3) should be expressed through the integral

$$J_n = \int_0^\infty \frac{1}{(\vec{r}(x))^{2n}} dx = \int_0^\infty \frac{dx}{(R^2 + 2Bx + x^2)^n} \tag{5}$$

This integral was calculated analytically in [2]. In the present paper it is calculated in more compact approximate form (See Appendix A)

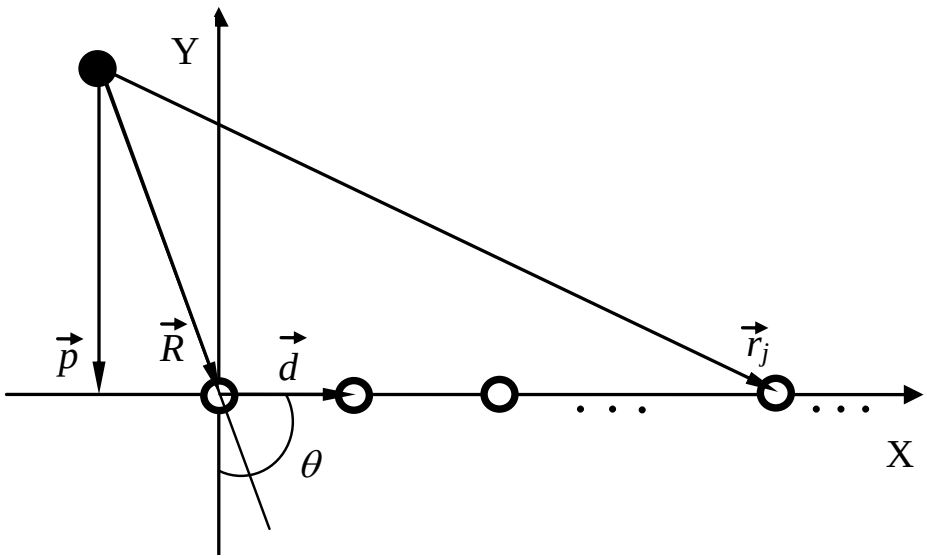

Figure 1. Geometry of interaction of the SFC (filled circle) with the SFL (opened circles). The first force center of the SFL is placed in the coordinate origin. $\vec{p}$ - is the distance between the SFC and the SFL. $\vec{R}$ - is the vector, connecting SFC with the first force center in the SFL. $\vec{d}$ is the vector equal to the distance between nearest force centers in the SFL. θ – is the characteristic angle equal to the angle between $\vec{d}$ and $\vec{R}$. $\vec{r}_j$ - is the distance between the SFC and j-th force center of the SFL.

$$J_n(p,\theta) = \frac{(2n-3)!!V_n(\theta)}{2^{n-1}p^{2n-1}(n-1)!} \quad (\theta \neq 0) \tag{6}$$

$$J_n = \frac{1}{(2n-1)R^{2n-1}} \quad (\theta = 0)$$

where

$$V_n(\theta) = \theta - \frac{\sin(2\theta)}{4}\left[\frac{2 - D_2\sin^2(\theta) - D_n\sin^{2n-2}(\theta) + \alpha\beta D_{n-1}\sin^{2n}(\theta)}{[1-\alpha\sin^2(\theta)][1-\beta\sin^2(\theta)]}\right] \tag{7}$$

$$D_n = \alpha^{n-1} + \beta^{n-1}$$

$$p = R\sin(\theta) \tag{8}$$

and $\alpha = \frac{1}{2.5}$, $\beta = \frac{1}{1.06}$.

The proposed formula gives accuracy better then 1% in all practical cases for $1 \le n \le 7$.

In the continuum approach the relation between integral (5) and discreet sum (3) can be illustrated graphically. To do this assume that (3) represents the area occupied by the appropriate set of rectangles each of which has the width equal to *d*. This area can be expressed as follows (figure 2):

$$S_n = d\sum_{k=0}^{\infty}\frac{1}{(\vec{r}_k)^{2n}} = dW_n \tag{9}$$

Normally [1, 2, 3] in continuum approximation it is assumed that area, which corresponds to integral (red curve in figure 2) is equal to the area S_n, which gives the relation

$$W_n = \frac{J_n}{d} \tag{10}$$

Currently this approximation both in one-dimensional [2, 9] and two-dimensional cases is widely used for estimation of energy of interaction of nanotubes [3, 8] and absorption of atoms by nanotubes [7]. As it can be seen from figure 2 this approximation can give significant error if the subintegral function decays fast enough. In the case of LD-potential this effect can play significant role for interaction between two objects with overall sizes having the same order of magnitude as the distance between them. Practically it means that absorption of the molecules on the edges of nanotubes, for example, can not be described by (10) with sufficient accuracy.

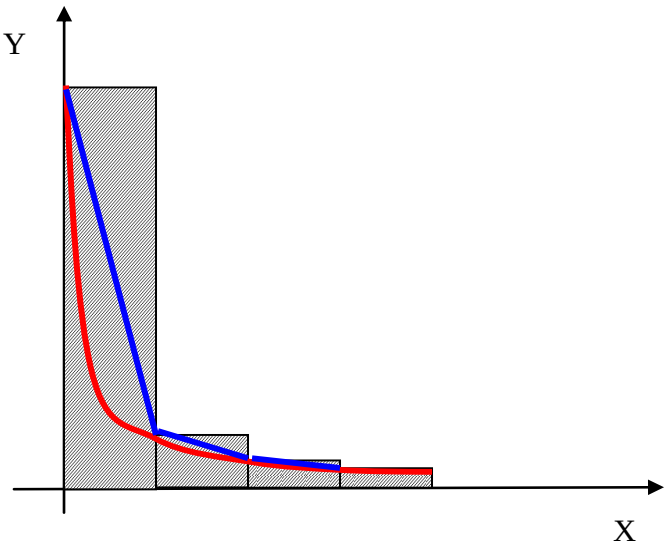

Figure 2. Relation between discrete sum and continues integral. Dashed rectangles represent area, which corresponds to S_n. The red smooth curve is the function, which is integrated in (5). The blue polyline corresponds to trapezoid approximation of (5).

To adapt the continuum approximation for the case of quickly decaying function we propose to use trapezoid or parabolic approximation of the area, which correspond to integral (5) instead of rectangular one used in (10). In the trapezoid approximation the area can be expressed as follows:

$$S_n = \frac{d}{2(\vec{r}_0)^{2n}} + d\sum_{k=1}^{\infty}\frac{1}{(\vec{r}_k)^{2n}} = dW_n - \frac{d}{2(\vec{r}_0)^{2n}}$$

which leads to the estimation

$$W_n = \frac{1}{2(\vec{r}_0)^{2n}} + \frac{J_n}{d} \tag{11}$$

In the parabolic approximation of the integral

$$S_n = \frac{d}{3}\left\{\frac{1}{(\vec{r}_0)^{2n}} + \frac{4}{(\vec{r}_1)^{2n}} + \frac{2}{(\vec{r}_2)^{2n}} + \frac{4}{(\vec{r}_3)^{2n}} + \frac{2}{(\vec{r}_4)^{2n}} + \ldots\right\} = \frac{J_n(p,\theta_0)}{d} \tag{12}$$

where θ_0 is the CA, which corresponds to the SFL, starting from the force center with zero index. As it can be seen in parabolic approximation the single equation (12) is not enough to

extract W_n from it. To perform this extraction we shall use one more equation for the calculation of S_n for the SFL, which starts from the force center with the index equal to one

$$S_n^1 = \frac{d}{3}\left\{\frac{1}{(\vec{r}_1)^{2n}} + \frac{4}{(\vec{r}_2)^{2n}} + \frac{2}{(\vec{r}_3)^{2n}} + \frac{4}{(\vec{r}_4)^{2n}} + \frac{2}{(\vec{r}_5)^{2n}} + \ldots\right\} = \frac{J_n(p,\theta_1)}{d} \tag{13}$$

where θ_1 is the CA, which corresponds to the SFL, starting from the force center with the index equal to one. Summarizing (12) and (13) we have

$$W_n = \frac{J_n(p,\theta_0) + J_n(p,\theta_1)}{2d} + \frac{5}{6(\vec{r}_0)^{2n}} + \frac{1}{6(\vec{r}_1)^{2n}} \tag{14}$$

It is worth pointing out that (10), (11) and (14) are the equations, which approximate the discreet sum (3) with quickly growing accuracy, thus, it is recommended to use (14) instead of (10) for numerical calculations.

II. INTERACTION OF THE SEPARATE FORCE CENTER WITH THE FORCE LINE OF FINITE LENGTH

We will call the finite set of N force centers situated on the straight line the finite force line (FFL). Interaction of the FFL with the SFC can be considered as the interaction of the SFC with SFL starting from the force center with zero index minus energy of interaction of the same SFC with the SFL, which start from the force center with the index N.

$$V_{m,n}(p,\theta_0,\theta_N) = 4\varepsilon\left\{\sigma^{2m}\left[W_m(p,\theta_0) - W_m(p,\theta_N)\right] - \sigma^{2n}\left[W_n(p,\theta_0) - W_n(p,\theta_N)\right]\right\} \tag{15}$$

θ_0 (θ_N) is the CA, which corresponds to the SFL, starting from the force center with the index equal to zero (N). Values of W_n should be taken from (10), (11) or (14) depending on the approximation. Due to short-range nature of Van der Waals forces contribution of the parts with θ_N into energy might be very small. The equation (15) provides suitable small parameter for accounting for the end effects

$$\gamma = \frac{W_n(p,\theta_N)}{W_n(p,\theta_0)} << 1$$

III. RESULTS AND DISCUSSION

As an example of use of the proposed approach we consider interaction of the single molecule of carbon with infinite hydrocarbon chain. The resulting energy of interaction for $V_{6,3}$ (12-6 LD-potential) for all three approximations is shown in figure 3. The hydrocarbon chain stars from x=0 and stretches in the positive direction of the X-axis. The distance between the chain and the molecule $p = 0.196$ nm and $\sigma = 0.392$ nm.

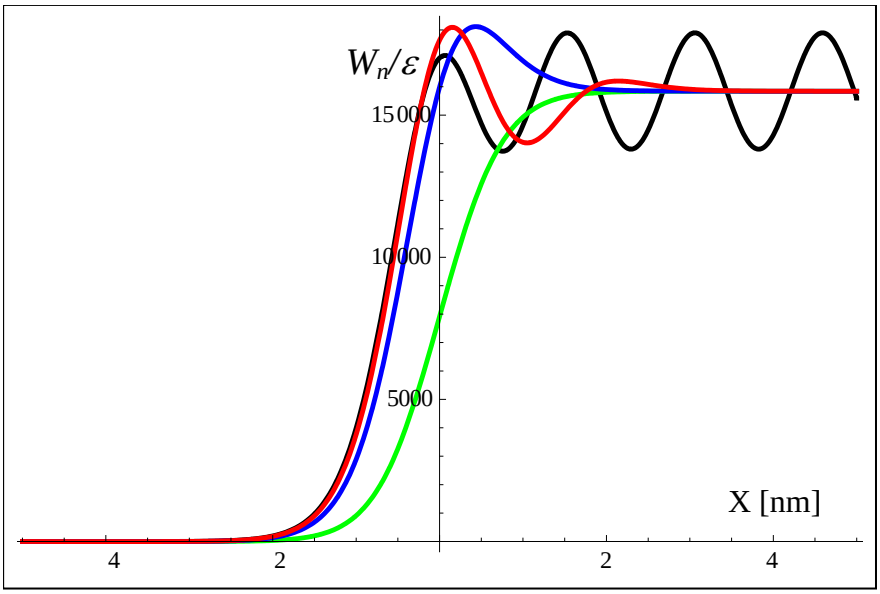

Figure 3. Energy of interaction of the single carbon atom with the infinite hydrocarbon chain. Black curve is discrete summation based on (3), green curve is the rectangular approximation (10), blue curve is the trapezoid approximation (11) and red curve is the parabolic approximation (14).

As it is clear from the analysis of curves all approximations have the same accuracy far from the edge of the hydrocarbon chain and the result corresponds to average energy, which is obtained during direct summation. Note that all approximations developed above don't reproduce the oscillation part of the potential far from the edge of the chain. This behavior was expected because the continuum approximation breaks discrete translation symmetry of the real chain substituting it by continuous translation symmetry of uniform rod.

The region around coordinate origin, which corresponds to the edge of the chain, is represented by different approximations with different accuracy. Commonly used [1, 2, 3] rectangular approximation (10) gives poor results in this region because it is this region in which area represented by rectangles in figure 2 has the biggest discrepancy with the integral approximation. The trapezoid approximation gives the better result in this area and, as it was expected the proposed parabolic approximation gives the best and quite satisfactory coherence with the discrete sum calculations. Note that this area has the biggest gradient, thus, it provides maximum contribution for the forces which disturb the system from equilibrium. Precise energy calculation in this region is very important during approximation

of frequencies of vibration of atoms, thus the proposed approximation appears to be the most adequate.

CONCLUSION

The proposed extension of commonly used continuum model for calculation of Van der Vaals energy of interaction of nanostructures gives better approximation to discrete model. It also introduces clear and simple small parameter, which can be used during numeric calculations.

The proposed method opens the way to account for oscillating part of potential, which can not be taken into account by ordinary continuum approximation. This method also can be used to model two dimensional objects as the set of one dimensional SFLs. These features of the proposed model will be discussed in the second part of this article which is to come in the next issue of this magazine.

APPENDIX A. CALCULATION OF THE MAIN INTEGRAL

Calculation of the integral, which is used to evaluate the interaction between SFC and SFL is based on the analytical expression of the integral [10]

$$\int \frac{dx}{(1+x^2)^n} = \frac{x}{(2n-1)} \sum_{k=1}^{n-1} \frac{(2n-1)(2n-3)(2n-5)...(2n-2k+1)}{2^k (n-1)(n-2)...(n-k)(1+x^2)^{n-k}} + \frac{(2n-3)!!}{2^{n-1}(n-1)!} \arctan(x)$$

which can be easily written in the form

$$\int \frac{dx}{(1+x^2)^n} = \frac{(2n-3)!!}{2^{n-1}(n-1)!} \left(\frac{x}{2} \sum_{m=1}^{n-1} \frac{2^m (m-1)!}{(2m-1)!!(1+x^2)^m} + \arctan(x) \right) \tag{A1}$$

The main integral can be expressed as follows:

$$J_n == \int_0^\infty \frac{dx}{(R^2 + 2Bx + x^2)^n} = \frac{1}{p^{2n-1}} \int_{B/p}^\infty \frac{dx}{(1+x^2)^n}$$

Substituting (A1) into this equation we have

$$J_n = \frac{(2n-3)!!}{p^{2n-1} 2^{n-1} (n-1)!} \left[\arctan\left(\frac{p}{B}\right) - \frac{B}{2p} \sum_{m=1}^{n-1} \frac{2^m p^{2m} (m-1)!}{(2m-1)!! R^{2m}} \right] \quad (\theta \neq 0) \tag{A2}$$

and

$$J_n = \frac{1}{(2n-1)R^{2n-1}} \quad (\theta = 0) \tag{A3}$$

Note that *p* should be taken from (7). The last two formulas correspond to analytical solution and are valid for arbitrary *n*. To make (A2) more simple we will approximate its sum by the geometric progression. It could be noticed that

$$\frac{2^m (m-1)!}{(2m-1)!!} \cong \alpha^{n-1} + \beta^{n-1} \quad (\alpha = \frac{1}{2.5}, \quad \beta = \frac{1}{1.06}) \tag{A4}$$

The accuracy of such approximation for integer $1 \le n \le 7$ is more than 1%, which is sufficient for all possible applications. The values of α and β were obtained by least square fitting of left part of (A4) by its right part. Substituting (A4) into (A2) and using standard formula for the sum of terms of geometric progression we finally obtain (6).

REFERENCES

[1] Y. Chan, J.M. Hill, "Modelling interaction of atoms and ions with graphene", *Micro and Nano Letters*, 5(5), (2010), 247-250.

[2] S.M. Balashov and V.A. Krylov, "The oscillator approach in the mean field model of the highly ordered Langmuir monolayer", *Thin Solid Films*, 239, (1994), 127-137.

[3] B.J. Cox, N. Thamwattana and J.M. Hill, "Mechanics of nanotubes oscillating in carbon nanotube bundles", *Proc. Royal Soc. A*, 464, (2008), 691-710.

[4] P. I. Dergunov, A.V. Klinger, A.V. Tvardovskii, A.A. Fomkin, "Use of the Lennard-Jones potential in modeling the absorption deformation of microporous carbon adsorbents", *Journal of Engineering Physics and Thermophysics*, 79(2), (2006) 276-282.

[5] I.V. Lebedeva, A.A. Knizhnik, A.M. Popov, O.V. Ershova, Yu. E. Lozovik and B.V. Potapkin, "Diffusion and drift of graphene flake on graphite surface", *J. Chem. Phys.*, 134, (2011), 104505-104519.

[6] V.V. Barkalin, A.S. Chashinski, "Adsorbtion properties of carbon nanotubes from molecular dynamics viewpoint", *Rev. Adv. Mater. Sci.*, 20, (2009), 21-27.

[7] O.N. Kalugin, V.V. Chaban, V.V. Loskutov, and O.V. Prezhdo, "Uniform diffusion of acetonitrile inside carbon nanotubes favors supercapacitor performance", *Nano Letters*, 8(8), (2008), 2126-2130.

[8] A.Y.T. Leung, and J.L. Kuang, "Nanomechanics of a multiwalled carbone nanotube via Flugge´s theory of a composite cylindrical lattice shell", *Phys. Rev. B*, 71, (2005), 165415-165424.

[9] S.B. Opps, B.G. Nickel, C.G. Gray and D.E. Sulivan, "The groud-state phase behavior of model Langmuir monolayers", *J. Chem. Phys*., 13(1), (2000), 339-348.

[10] M. Rizik, L. S. Gradstein, "Tables of sum, series, integrals and products", *Nauka*, Moscow, 1971.

Smart Nanocomposites
Volume 2, Number 1
ISSN: 1949-4823

INFLUENCE OF MAGNETIC FIELD DURING DEPOSITION OF THIN CONIMNP FILMS

C. D. M. Campos[a], A. Flacker[b,c], A. R. Vaz[b,c], S. A. Moshkalev[b] and E. G. O. Nóbrega[a]

[a]Faculdade de Engenharia Mecânica,
Universidade Estadual de Campinas,
13083-970, Campinas, Brazil
[b]Centro de Componentes Semicondutores,
Universidade Estadual de Campinas,
13083-870, Campinas, Brazil
[c]Centro de Tecnologia da Informação Renato Archer

ABSTRACT

Permanent magnets can produce large forces (mN) over long activation distances, which provide a significant advantage over the limited mN range force and short distance provided by electrostatic and thermal actuators. To achieve this advantage, the magnetic energy in the magnetized films should be maximized. On way to reach this objective is using magnets during electroplating. In this paper we analyze the effect of this alternative in films properties. Nevertheless the fracture occurence increased when films were deposited in the presence of magnetic field, roughness decreased and homogeneity increased.

INTRODUCTION

The rapid development of magnetic microelectromechanical systems (MEMS) including magnetic sensors, actuators and recording heads has motivated research on discovering and understanding new magnetic materials and fabrication techniques [1]. Electrodeposition has become a mature technique for MEMS fabrication because it has a fast deposition rate, does not require a vacuum system, is relatively low cost, is compatible with CMOS circuit fabrication, and can deposit a variety of materials [1].

Permanent magnets can produce large forces (mN) over long activation distances, which provide a significant advantage over the limited mN range force and short distance provided by electrostatic and thermal actuators. To achieve this advantage, the magnetic energy in the magnetized films should be maximized [1].

Electrodeposited thin films with anisotropic vertical magnetization are superior in achieving out-of-plane actuation than films with in-plane anisotropy. Thus, Horkans technique [2] applied to CoNiMnP [3] is attractive for magnetic MEMS devices, and this magnetic CoNiMnP cantilever actuator was first described as a candidate for perpendicular recording because of its significant out-of-plane anisotropy. According to the initial studies, perpendicular anisotropy in CoNiMnP films is due to the epitaxial growth of CoNiMnP in the vicinity of the seed layer interface.

This process produces a preferred crystallite orientation leading to columnar grains of magnetic material with the easy axis aligned perpendicularly to the substrate. Subsequent reports of electrodeposited CoNiMnP cover a range of methods and results. Liakopoulos et al. fabricated CoNiMnP magnet arrays for MEMS actuation.

Later, the same group reports on the effects of electroplating CoNiMnP under an applied external magnetic field, likely motivated by evidence that applying a magnetic field during plating can influence the preferred orientation of ferromagnetic deposits [4-6].

In this paper, we analyze the effect of magnetic field over film morphology by comparing images obtained from films made with and without magnetic field.

EXPERIMENTAL PROCEDURE

Metallic films were deposited over PA substrates, with dimensions of 25 x 25 x 0.5 mm, obtained according to the procedure described by NOBREGA and CAMPOS [7]. PA surface, after cure process, does not present good adherence with metal composites, so surface modification [7] is necessary in order to promote adhesion strength between metallic film and surface.

The strength depends on mechanical bonding with anchoring effects [8]. This treatment includes an initial pre-treatment with acid solution, followed by sensitization, activation and electroless deposition of thin layers of Ni-P.

Samples were pre-treated during 30s in a solution containing sulfuric (98%) and nitric (65%) acid in 19:1 ratio followed by wash in DI water.

Onto PA substrate, it was employed a sensitization step with SnCl2, followed by an activation step with $PdCl_2$ prior to plating [10]. After surface treatment, a non-commercial autocatalytic solution of electroless Nickel-Phosphorus (Ni-P), adapted from the solution published by Dubin et. al. [12-13], is used. The bath has $NiCl_2$, as nickel ion source, NaH_2PO_2 as reducing agent, $CH_3C_2O_2Na$ and NH_4Cl as complexing agent, $Pb(NO_3)_2$ for stabilization and NaOH (5N) is added for pH control. Deposition temperature was 60 ± 1 ºC and stirrer agitation was used.

The membrane treatment was the same for any sample. Samples were thickened by a non-commercial CoNiMnP bath, adapted from LIAKOPOULOS et. al. [4], described in Table I. Pure nickel anode was used, and magnets were placed by both sides of the bath equipment, with temperature controlled by hot plate. A paddle was used in order to achieve film homogeneity.

Flexure tests were made by flexing samples with ~2 mm curvature radius, and then evaluating changes in the films morphology with SEM.

Table I. Bath composition (upper part of the table) and process conditions (lower part of the table) for CoNiMnP deposition

Reagents	**Concentration (g/L)**
$CoCl^2.6H_2O$	24
$NiCl^2.6H_2O$	24
$MnCl^2.H_2O$	4
$NaH_2PO_2.H_2O$	4,5
Sodium Lauryl Sulfate	0.2
NaCl	23
H_3BO_3	25
Process conditions	**Value**
Temperature (ºC)	room
Current density (A/dm^2)	0.5 (0-1)

RESULTS

Figure 1 shows SEM images of both samples. Figures 1.a to 1.d show the sample surface, while the Figs. 1.e to 1.h show cross sections. In surface images the main observed property is the presence of hillocks and fracture frequency.

Samples fabricate in the presence of magnetic field presented more fractures after flexure tests, similarly to that observed in [8, 15]. This occurs because of the internal stress increase under magnetic field.

On the other hand, films fabricated without magnetic field presented more hillocks. Both phenomena may be related. As described in previous work [8], although this mechanism is not well understood at the moment, certain parallel can be made with an ion drift occurred in plasmas, when magnetic and electric fields are not parallel.

Without the magnetic field, the process is driven by a local electric field, normal to the surface. Then, nearly conformal deposition occurs onto the hillock surface as can be seen in Fig. 5e. In this case, surface roughness formed during electroless deposition is reproduced in the electroplating, as illustrated by the inset. On the other hand, when magnetic field is present, a Lorentz force causes a drift of charged particles in a direction normal to both electric and magnetic fields. The (E x B) drift should result in ions movement in the "downhill" direction near the surface, resulting in a film flattening. This flattening results in denser films and higher internal stress, increasing fracture occurrence.

Observing not-polished cross-sections it may be observed that the film is less homogeneous in films fabricated in the absence of magnetic field.

The effect of the presence of magnetic field during depositions on the properties of magnetic films was already described in literature [8]. The results found in this work were similar, with an increase of 2 times in coercivity and retentivity of films while maximum energy product increased 10 times.

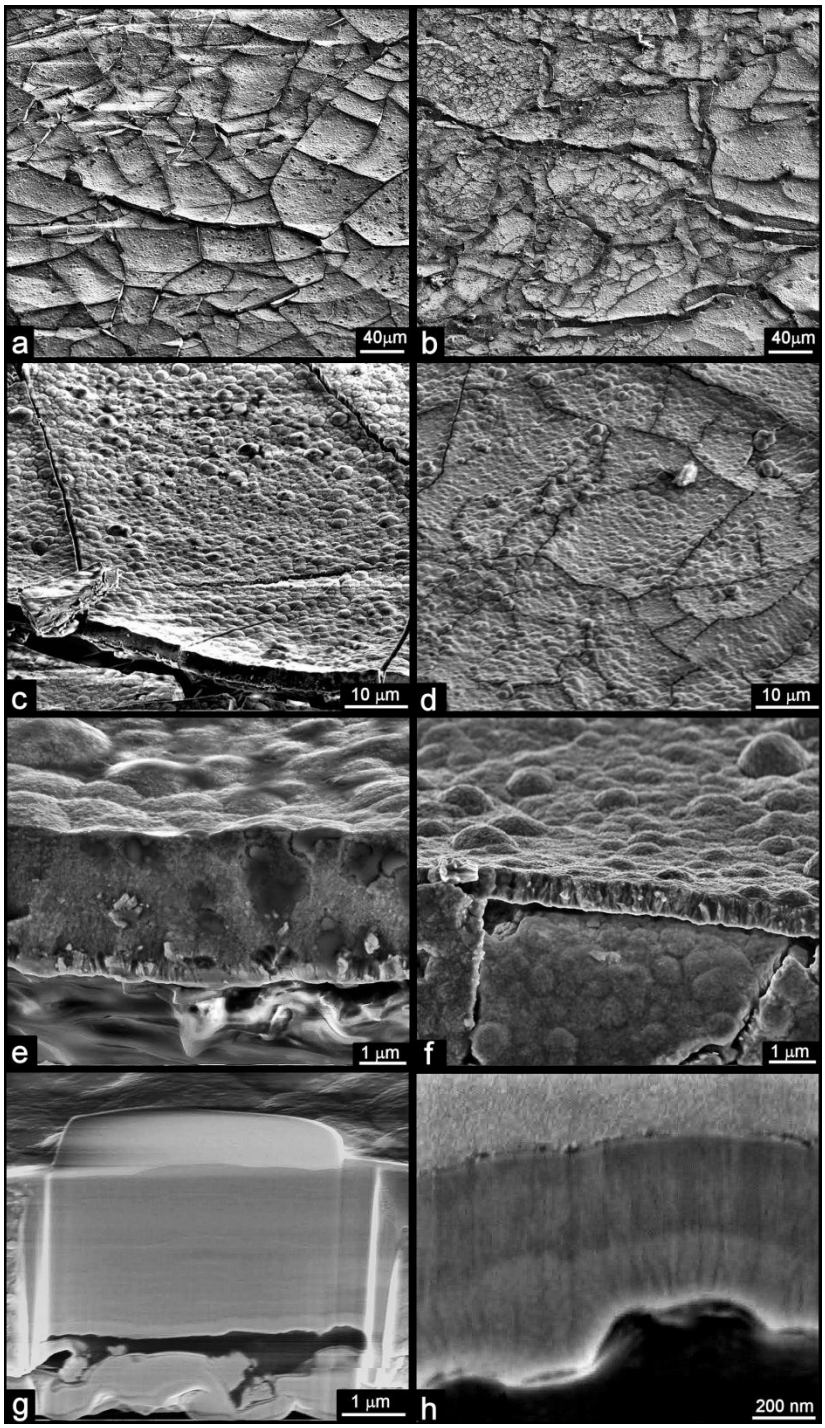

Figure 1. SEM images of metallic films a) surface obtained without magnetic field b) surface obtained at magnetic field c) surface without magnetic field d) surface at magnetic field applied e) cross section of no magnetic field f) cross section without magnetic field g) polished cross-section without magnetic field and h) polished cross section with magnetic field.

CONCLUSION

Based on the results in this work, it is possible to conclude that the magnetic field has significant influence on metal distribution over the substrate. When the film is deposited in the presence of magnetic field, considerable improvements in magnetic properties and surface uniformity were observed.

ACKNOWLEDGMENTS

The authors wish to thank the LMF-LNLS, LMBT-IFGW-Unicamp, DQA-IQ-Unicamp for the help in this project, and FAPESP for the financial support.

REFERENCES

[1] S. Guan, B. J. Nelson - *Journal of Magnetism and Magnetic Materials* – 292, 49, 2005.
[2] J. Horkans, D.J. Seagle, I. Chang, *J. Electrochem. Soc*. 137 (1990) 2056.
[3] H.J. Cho, C.H. Ahn, -*IEEE J. Microelectromech. Systems* – 11, 78, 2008.
[4] T. M. Liakopoulos, W. Zhang, and C. H. Ahn, *IEEE Trans. Magn*., 32, 5154, 1996.
[5] H. J. Cho, S. Bhansali, and C. H. Ahn, *J. Appl. Phys.*, 87, 6340 2000.
[6] M. D. Grapes, C. J. Morris – *J. Electrochem. Soc.*, 157, D642-D647, 2010.
[7] E.G.O. Nóbrega, C. D. M. Campos, A. Flacker, A. R. Vaz, S. Moshkalev – *J. Electrochem. Soc*. – 158, D 330-334, 2011.
[8] E. G. O. Nobrega, C. D. M. Campos – *ABCM Symposium Series in Mechatronics* – 3, 586, (2008).
[9] J. S. Costa, A; Flacker, F. Fruett – *ECS Trans.* – 23, 327, (2009).
[10] J. A. Cunningham – *Solid-state electron*. - 8, 735, (1965).
[11] J. w. Severin, R. Hokke, H. Van Der Vel, G. With – *J. Electrochem. Soc*. – 140, 682, 1983).
[12] V. M. Dubin, D. Lopatin, V. G. Sokolov –*Thin Solid Film* – 226, 94, (1993).
[13] V. M. Dubin, S. D. Dobson, D. Rose, G. Hodes – *Thin Solid Films* – 387, 155, 2001).
[14] Brenner, G. E. Ridell – *J. Res. Nat. Bur. Standards* – 39, 385, (1947).
[15] R. K. Mayes – *Plat. Surf. Finishing* – 118, 60, (1999).

Smart Nanocomposites
Volume 2, Number 1
ISSN: 1949-4823

MICROCAPSULES IN COATINGS– RECOVERING A SCRATCH TO A PATCH

Kiran Bhat Kashi and Victoria J. Gelling
North Dakota State University,
Fargo, ND, 58102, USA

ABSTRACT

This review will present a comprehensive view of the use of microcapsules in coatings. Beginning with the general self healing strategy, this paper will discuss the traditional repair methods used in polymers. It will then continue to summarize the recent advances in the field of smart materials pertaining to applications in coatings. The review summarizes the work of many research groups across the globe and presents the recent advances in the coatings industry with the incorporation of these smart microcapsules capable of performing various protective functions to increase the life time of the coatings chosen for the selected area of application.

1. INTRODUCTION

Man's dependence on materials has been everlasting, which is evident from the representation of these materials in the names of the ages such as the Bronze Age, Iron Age etc., thus making material science one of the oldest and the most dynamic disciplines of science. Such dependence on materials has not only led to inventions that satisfy human needs but also has raised expectations for materials that do much more. One such expectation is the ability to autonomously respond to changing conditions. The advent of nanotechnology appears to be one of the ways to meet this rising expectation [1]. 'Smart' or responsive materials are materials that respond to external stimuli. The stimulus can be electrical, magnetic, light, pH etc. The inspiration for responsive materials has been derived from complex biological processes in humans and animals [2-4] and mimicking these natural processes [5]. One such example is the micro-vascular style delivery of the healing agent which continuously monitors the 'health' of the system [6].

Smart materials are divided into various classifications depending on the type of stimuli they respond to and the action that they perform in response. One such application of responsive materials is in self healing of organic coatings. "Self healing can be defined as the ability of a material to heal (recover) damages automatically and autonomously without

external intervention" [7]. Microencapsulation, a process by which a micron sized solid particles, liquids or gases are incorporated an inert shell enables the isolation and protection of the material from the environment[8, 9]. Encapsulation techniques have long been used for a vast array of applications. In 1930s Barrett Green studied colloidal chemistry[10] and created the first gelatin microcapsules by coacervation technique which was later used to create a colorless dye based paper which upon application of mechanical pressure using a pen would release visible color[11]. The use of polymers as encapsulating materials came to existence in the early 1960s, when the need for materials to act as a rate controlling device or a container began to gain importance [12]. Release technology is classified into various types depending on the kinetics and mode of release. The various types are (a) Erodible devices that disappear; (b) Membrane encapsulated reservoir devices; (c) Matrix devices; (d) Reservoir devices without a membrane [12]. The pharmaceutical industry has been the pioneer in the use of this technique to protect drugs from the acidic environment of the stomach and target the drug to a specific area in the body, or provide sustained release of the same [13-15]. The food industry uses microcapsules to encapsulate flavors, retain aroma, increase product shelf life and protect ingredients from oxidation [16, 17].

A coating is generally defined as material which when applied to a surface appears as a continuous film. However, the application of such a protective layer on a material of choice is also considered coating. Paints are dispersions of various types of binders, volatile components, pigments and additives, formulated for a specific application. Coatings are multilayered systems which generally contain a top coat and a primer[18]. Coatings are mainly applied to surfaces for decorative and protective purposes. Functional coatings are coatings with the same properties as that of regular coatings with additional capabilities[19]. These additional capabilities include antifouling [20], self cleaning[19, 21, 22], scratch resisting[23, 24], antibacterial[25], antigrafitti[26], and anticorrosive[27, 28] functions. Incorporation of various components into coatings makes such coatings functional. By definition, metal rich primers are functional coatings too. However, functional coatings also have the additional feature of sensing damage. Functional coatings also fall under the category polymer composites.

2. FRACTURE MECHANICS IN POLYMERS

Polymer composites have found use in many structural materials and damage due to chemicals, heat, environment etc is a common occurrence. Crack propagation is the most common method of failure and mechanics of failure has been modeled and researched [29-31].

For a crack to propagate, the energy supplied to the system must be greater or equal to the energy required to create new surfaces on the material [32]. The crack growth models that have been developed are mostly based on the parameter called K_I [33, 34]. In case of the model which involves the crack opening failure growth, K_I is related to the crack depth, material geometry and the applied stresses. The crack growth takes place when the maximum stress intensity factor is reached (K_{IQ}). During fatigue-type damage, crack propagation is related to both the change in K_I and the maximum stress intensity factor (K_{Imax}) during cycling. Thus, for a surface to self-heal the fractured surfaces need to be resealed or crack growth be impaired.

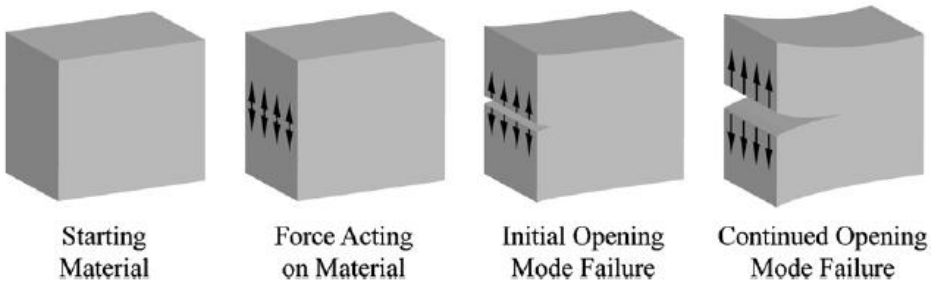

Figure 2.1. Mode I failure mechanism [32].

Extrinsic crack growth retardation used in self healing generally involves the dissipation of energy away from the propagating crack tip via a mechanical change behind the crack tip. Traditional methods used for healing or repairing include, patching, welding, and *in situ* curing of new resins.

2.1. Welding

Welding is the rejoining of fractured surfaces or fusing new materials to the damaged regions of a polymer composite. The physical property of the material is expected to be restored to the virgin state and chain entanglements helps to achieve the same[35]. The process of welding involves various transitions and rearrangements. Once the rearrangements are complete the two surfaces are fused together and are said to be welded. The various factors that need to be taken into account to ensure proper welding are the welding temperature[36, 37], surface roughness[38], chemical bonding between the surfaces[39] and the presence of solvents[40, 41]. The use of welding not only has applications for thermoplastic resins but also has been explored for themosets [42-45].

2.2. Patching

Patching is another technique in which the damaged area is replaced using a new material. The new material is attached via mechanical fastening or adhesive bonding. The approaches used in case of patching include superficial patches[46] or superficial patches after the removal of the damaged material[47]. The extent of recovery is dependent on the adhesion at the interface of the patch and the original material[48] and the thickness of the patch[49].

2.3. In Situ Curing of a Resin

This technique is very similar to patching however it can be understood as a variant of patching in which a new resin is injected into the damaged area. The uncured resin diffuses into the matrix and holds the patch in place.

Thermoplastics are repaired using fusion bonding and adhesive bonding. Both the methods work very similar to welding and patching. The traditional repairs that have been

used are used for external and more accessible damages instead of damages caused due to internal micro-cracks. The self healing polymers thus find applications in this area.

3. MATERIAL DESIGN

Degradation, be it natural or artificial, of materials is inevitable. Commonly used design principles include damage prevention and damage management. On a plot of damage level vs. time, for current man made materials, the rate of damage formation is either zero or positive at all times.

$$\frac{d(damage)}{dt} \geq 0 \ (for\ 0 < t < lifetime)$$

The approach where the materials are designed in such a way that they have a higher yield point and the rate of damage is less are the goals of the damage prevention approach [50]. The alternative approach to that of damage prevention is the damage management approach. It is based on the concept that the formation of the damage is not problematic as long as the damage is counteracted by a so called "healing" step which restores the material back to its pristine state.

Figure 3.1(a) shows a single stage healing which repairs the damage created and introduces a negative *d(damage)/dt* and the Figures 3.1(b) and (c) show two and multiple recoveries respectively. However, even though the damage level decreases after each recovery step, the recovered state is not where the pristine material would be. It can also be said that the material is self healing but only for a finite time. The negative damage formation could be mathematically described as,

$$\frac{d(damage)}{dt} < 0 \ (for\ t_i < t < t_{i+\Delta t})$$

The final material properties and material lifetime hence depends on the rate of damage formation and rate of recovery. Self healing is essentially a process in which new matter would have to be created in place of the matter that has been removed due to various failure mechanisms. Thus the mobility of the called healing agents must be a parameter that needs to be taken into consideration. Moreover, not only should the healing agents be able to reach the site of damage but also be able to heal the site through various processes such as chemical reaction, absorption etc. Thus to have such a system, the presence of a trigger or a stimulus becomes essential. Another major area to focus is the range or the area around which the self healing is pronounced. The damage recovery at different size scales provides insights into the area and the recovery efficiency. There are several types of stresses in a system, which eventually lead to crack formation.

Damage recovery in coatings follows a micro-meso-macro hierarchy. Since damage recovery in organic coatings involves material transport, the material needed for recovery purposes can be transferred from the bulk of the coatings or from the bulk of the three interfaces (air, substrate or filler).

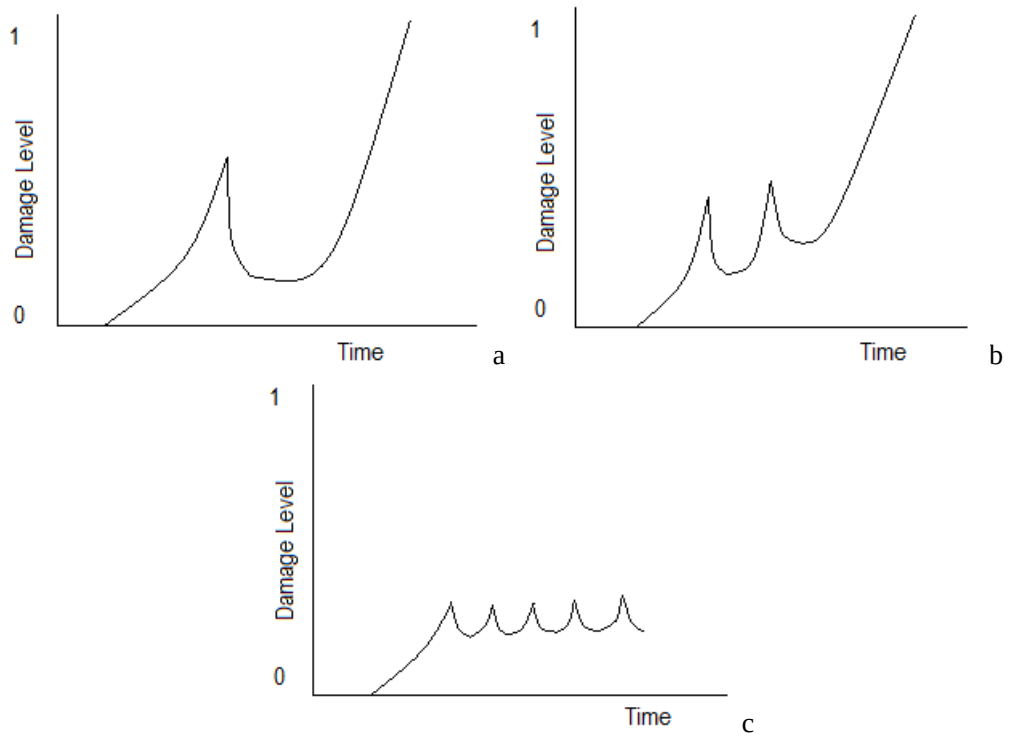

Figure 3.1. Schematic of three types of self healing materials [50].

Polymeric materials in general permit limited material transport and hence the material transport across a layer of organic coating is minimal. Also the timing of recovery becomes important, as the increase in the damage scale requires more material to restore it to the initial state. Thus, the idea is to be able to minimize the scale and hence minimize the amount of material required. This concept is also referred to as preemptive healing. Figure 3.2 summarizes the various length scales and the ease of recovery at various stages.

The quantitative methods to calculate the healing efficiency proposed by Wool and O' Connor [52] has been summarized by the following equations.

$$R(\sigma) = \frac{\sigma_{healed}}{\sigma_{initial}}$$

$$R(\varepsilon) = \frac{\varepsilon_{healed}}{\varepsilon_{initial}}$$

$$R(E) = \frac{E_{healed}}{E_{initial}}$$

$$R(I) = \frac{I_{healed}}{I_{initial}}$$

$$Healing\ efficiency(\eta) = \frac{Property\ value_{healed}}{Property\ value_{initial}} \times 100$$

where R, σ, ε, E and I are the recovery ratios relating to fracture stress, elongation at break, fracture energy and molecular parameters respectively. A comparison between an ideal and a

more practically achievable self healing material shows that we have a long way to go before such materials could be available to use in day to day life.

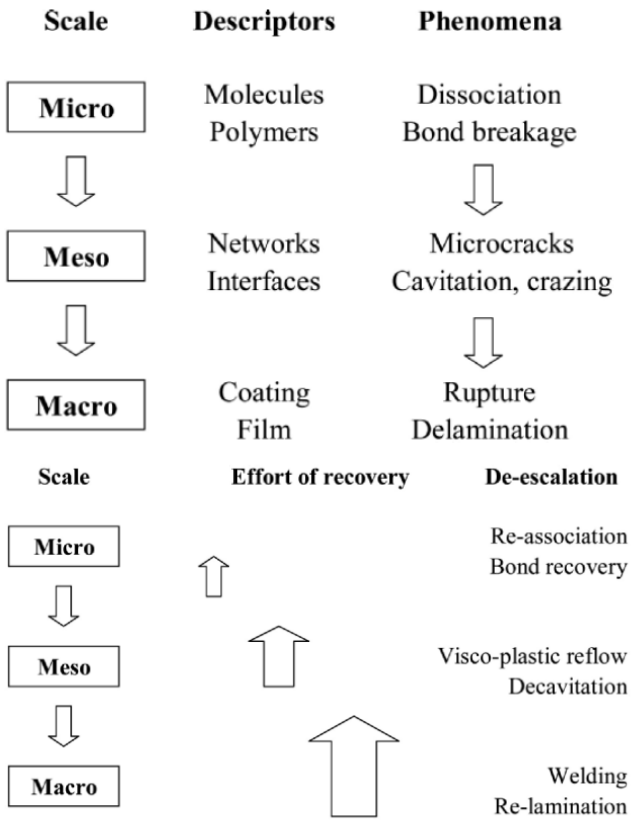

Figure 3.2. Damage escalation and Damage recovery in a self healing composite [51].

Table 1. Properties of ideal self healing materials [51]

Ideal self healing materials	More practical self healing material
Heals damage multiple times	Atleast a single recovery
Heals defects of any size	Applicable to small defects
Complete recovery of the material	Partial damage recovery
Autonomous healing	External assistance required for healing
Equal or superior properties as compared to the current materials	More or less equal to the current materials
Cheaper than current materials	Cost is more yet acceptable

4. pH STIMULUS

The encapsulation technique also finds an application in the area of corrosion inhibition. The use of microcapsules for corrosion inhibition is gaining a lot of importance. When a

metal corrodes there are two reactions that occur simultaneously - oxidation and reduction. The oxidation site is where the electron is released and the reduction reaction takes places where the released electron is consumed. The site where the oxidation occurs is also referred to as an anode and the reduction site is called cathode. Referring to these sites in terms of pH we can say that the anode is acidic and the cathode is basic. This principle is used in designing of the pH sensitive microcapsules [53]. The use of materials that undergo bond cleavage in the presence of hydroxyl ions is one of the key for the pH responsiveness. The incorporation of a corrosion inhibitor in such microcapsules causes the cathodic reactions to slow and hence inhibits corrosion.

Self assembly of opposite charged polyelectrolytes is often times used for the fabrication of thin films by Layer-by-Layer (LbL) technique[54, 55]. Recently, polyelectrolyte assemblies have been employed as containers to store the corrosion inhibitor in protective coatings. The distinct advantages of using this technique is the isolation of the inhibitor and providing on demand release of the inhibitor in response to changing environmental conditions. There also other more obvious disadvantages to this too, compatibility with the coating is one and the second is distribution within the coating. Change in local pH as a trigger is again preferred because corrosion reactions generally involve change in pH in the anodic and cathodic areas [56]. Zheludkevich et al. [57-59] demonstrated the use of SiO_2 particles coated with poly(ethylene imine)/poly(styrene sulfonate) (PEI/PSS) as nanocontainers embedded in a epoxy functionalized ZrO_2/SiO_2 sol–gel coating. They also demonstrated the used of halloysite nanotubes with corrosion inhibitors. The corrosion performance of the synthesized PEI/PSS nanocontainers was evaluated visually and using Electrochemical Impedance Spectroscopy. To begin with aluminum 2024 samples were coated with the sol-gel matrix with benzotriazole (corrosion inhibitor) dissolved directly in the sol–gel matrix and the nanocontainers. It was observed that the coatings containing the nanocontainers displayed better corrosion resistance against sodium chloride solutions of various concentrations when immersed for 14 days.

EIS results of the Aluminum 2024 samples after 190 h of immersion in 0.005 M NaCl show that the undoped hybrid coatings with different concentrations of the nanocontainers show similar behavior beyond 0.1 Hz and the measured capacitance was found to be similar as well. The sample containing the highest concentration of the nanocontainers showed almost pure capacitive behavior at low frequencies and, hence appeared to demonstrate good corrosion protection even after long immersion times. The lower nanocontainer concentration coatings showed a good corrosion performance however, formation of resistances at low frequencies show active defect formation. The undoped sol-gel coatings show the lowest corrosion resistance. It was also seen that two other samples prepared with direct impregnation of benzotriazole showed lower resistances.

The SVET method was also used to measure the influx of cations and anions on the surface. Figure 4.3 shows the SVET map of undoped ZrO_X/SiO_X film and the ZrO_X/SiO_X film with maximum nanocontainers. After 24 h of immersion, artificial defects (200 µm dia.) were introduced on the coatings.

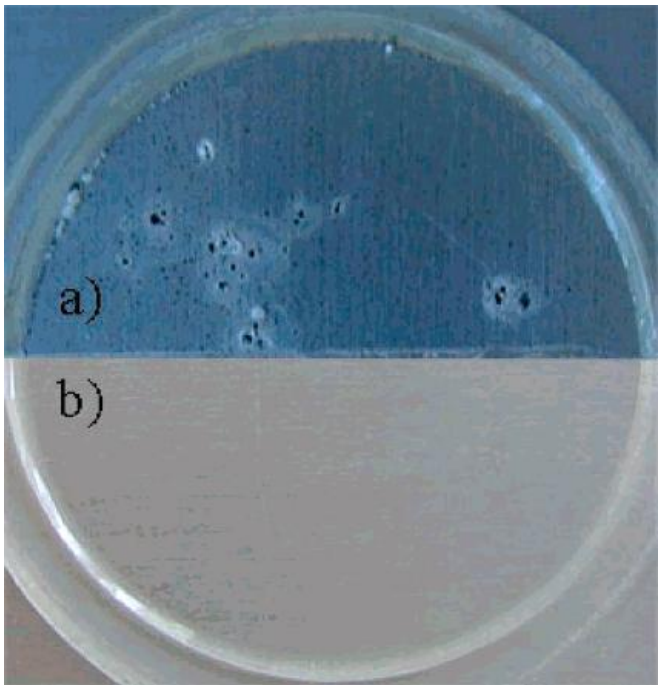

Figure 4.1 Aluminum 2024 alloy coated with sol-gel coatings containing (a) benzotriaole 14 days immersion in 0.005 M NaCl (b) nanocontainers 14 day immersion in 0.5 M NaCl[57].

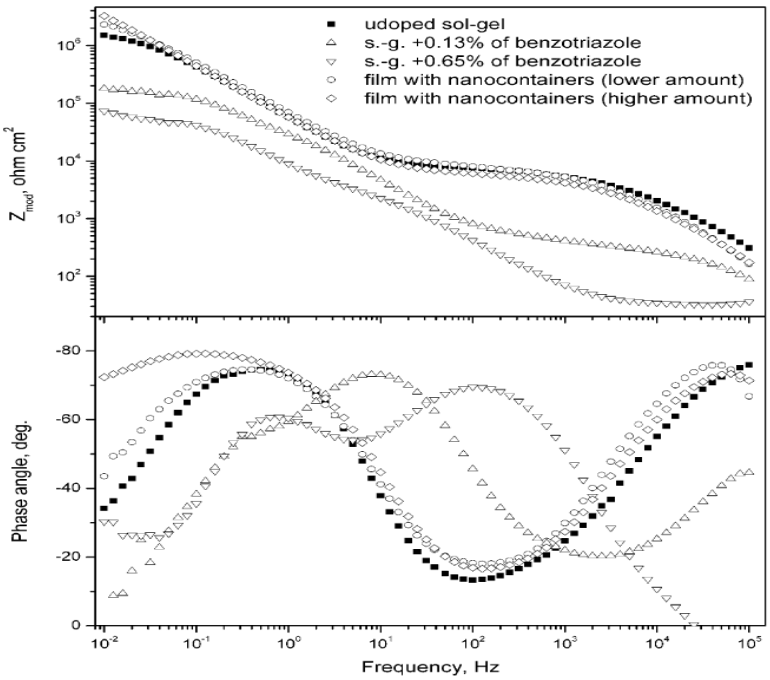

Figure 4.2. Impedance spectra of different sol-gel films after 190 h of immersion in 0.005 M NaCl.[57].

A well defined cathodic activity was observed in the area of the defect which became more intense with immersion time in case of the undoped ZrO_X/SiO_X film. However in case of the ZrO_X/SiO_X film doped with nanocontainers some cathodic activity was observed after 24 h of the defect formation. 2h later the defect was found to have been passivated and the defect remained "healed" even after 48 h.

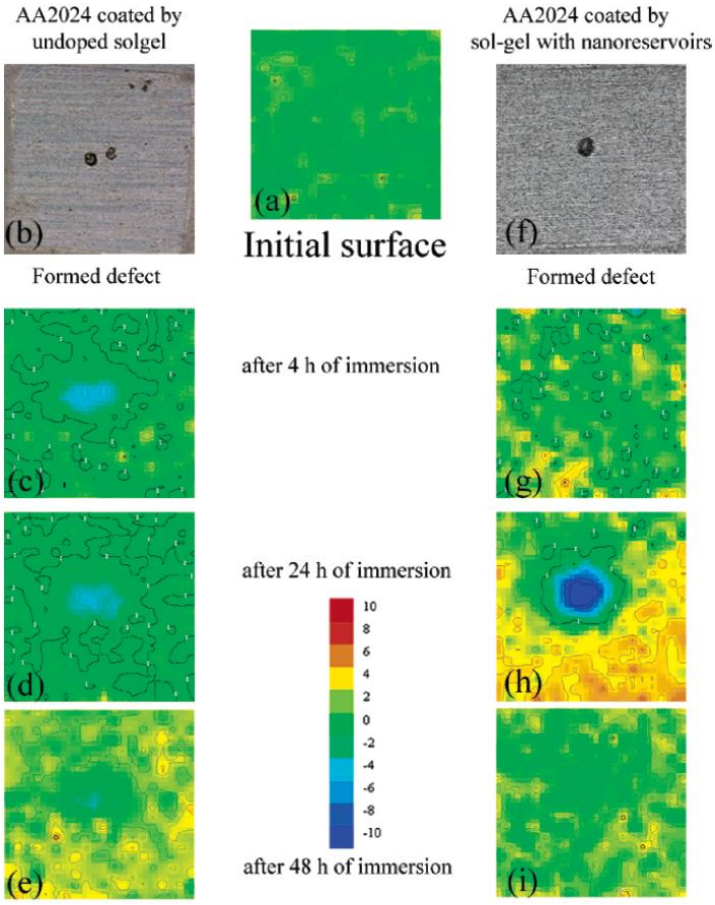

Figure 4.3. SVET maps of ionic currents measured above AA2024 panels with undoped sol- gel (a,c,d,e) and with pretreatments impregnated by nanocontainers (g-i). The maps were obtained before defect formation (a) and for 4 h (c,g), 24 h (d,h) and 48 h (e,i) after defect formation. Scanned area: 2 mm X 2 mm[57].

Multi-walled carbon nanotube (MWCNT) embedded microcapsules have also been fabricated by LbL self assembly technique and their electrochemical behavior evaluated[60]. The use of MWCNT is favorable due to its low cost compared to single walled carbon nanotubes. Figure 4.4 illustrates the fabrication of the MWCNT embedded microcapsules.

Cyclic voltammetry was conducted on the (PSS/PAH) MWCNT on a glassy carbon (GC) electrode using a phosphate buffer at pH 6.86 at different scan rates and a well defined reversible voltammogram was obtained at -0.05 V. An increase in scan rate lead to shifting of the peaks a little and redox current linearly scaled with the increase in the scan rate. Since the (PSS/PAH) in the GC electrode could not exhibit redox peaks, the observed peaks were

attributed to the MWCNT. The change in the behavior of the MWCNT with changing pH was also studied and was understood that by increasing the pH the peak potential decreased due to the decrease in the concentration of protons at higher pH.

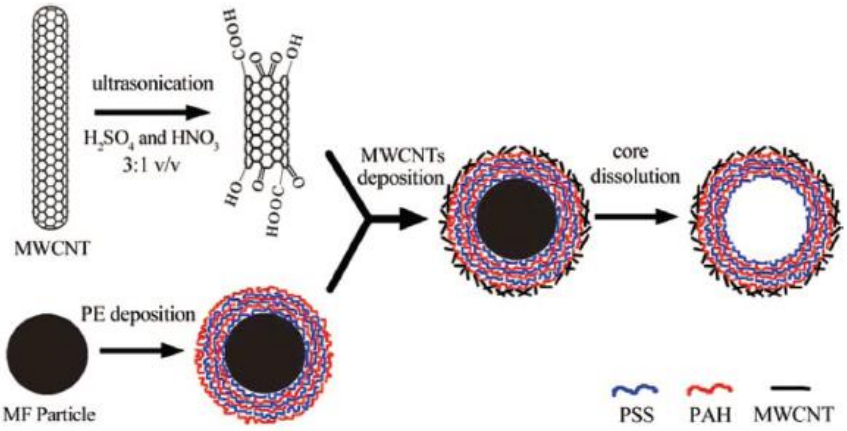

Figure 4.4. Representation of LbL assembly of MWCNT embedded microcapsule. PAH – poly(allylamine hydrochloride), PSS – Poly(sodium 4-styrenesulfonate)[60].

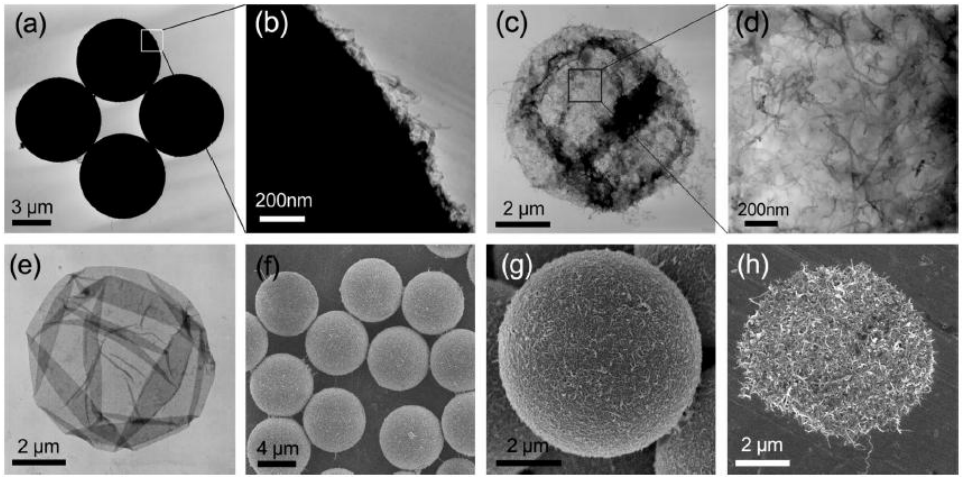

Figure 4.5. TEM images of (PSS/PAH)/MWCNT microcapsules before (a,b) and after (c,d) dissolving the core, (e) hollow (PSS/PAH) microcapsules. SEM images of (PSS/PAH)/MWCNT microcapsules before (f,g) and after (h) dissolving the core at different magnifications[60].

Thiourea has also been used as an inhibitor and has been encapsulated in glutin and polyvinyl alcohol (PVA)[61]. Polarization and EIS were performed on the samples after the addition of the microcapsules every 6 h. The release rate was measured using UV vis spectrophotometer and it was seen that the release time for microcapsules that were sealed once with gluten (#1) was 12 h, the time for the microcapsules sealed once with PVA was 18 h and the time for the ones that were sealed twice with PVA was found to be 48 h. Thus the use of PVA delayed the release rate over glutin. With the EIS study, it was observed that the diameter of the curve in the Nyquist plot increased with time and reached a stable value once

all the inhibitor was released. The corrosion rate decreased with release of the microcapsules and remained constant after the complete release of the inhibitor.

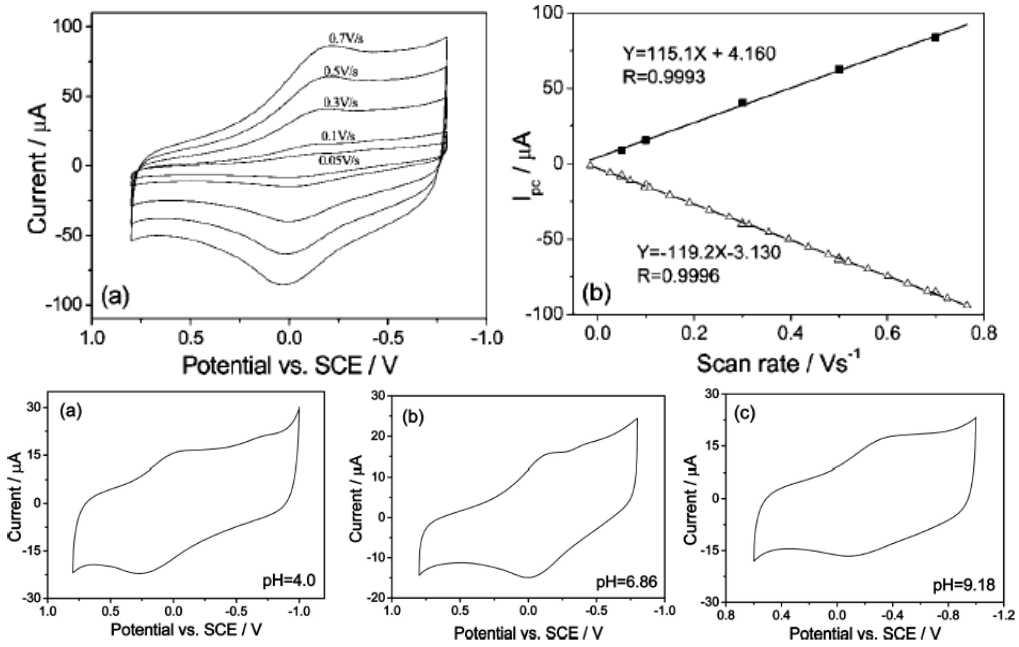

Figure 4.6. Cyclic Voltammogram of (PSS/PAH)/MWCNT microcapsules at different scan rates. Reductions and oxidation peaks as function of scan rates and (a,b,c) as function of pH at 0.1 V/s [60].

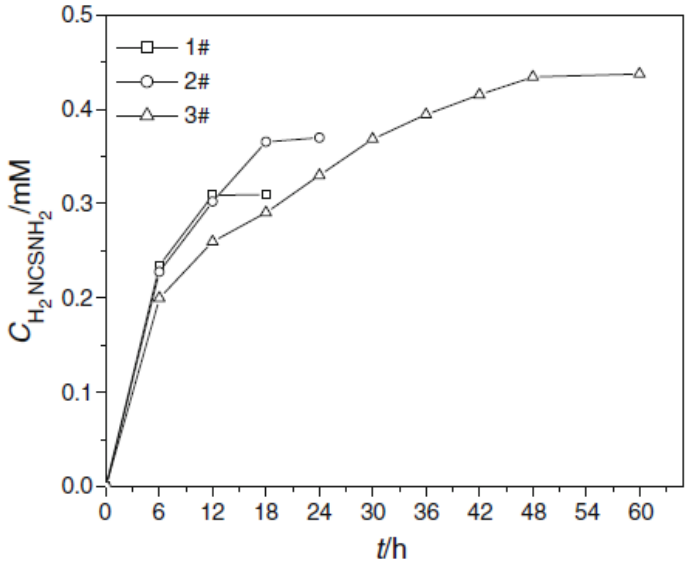

Figure 4.7. Concentration of thiourea and time in 0.12 L 0.1 M sulfuric acid solution as measured using UV spectrophotometric method [61].

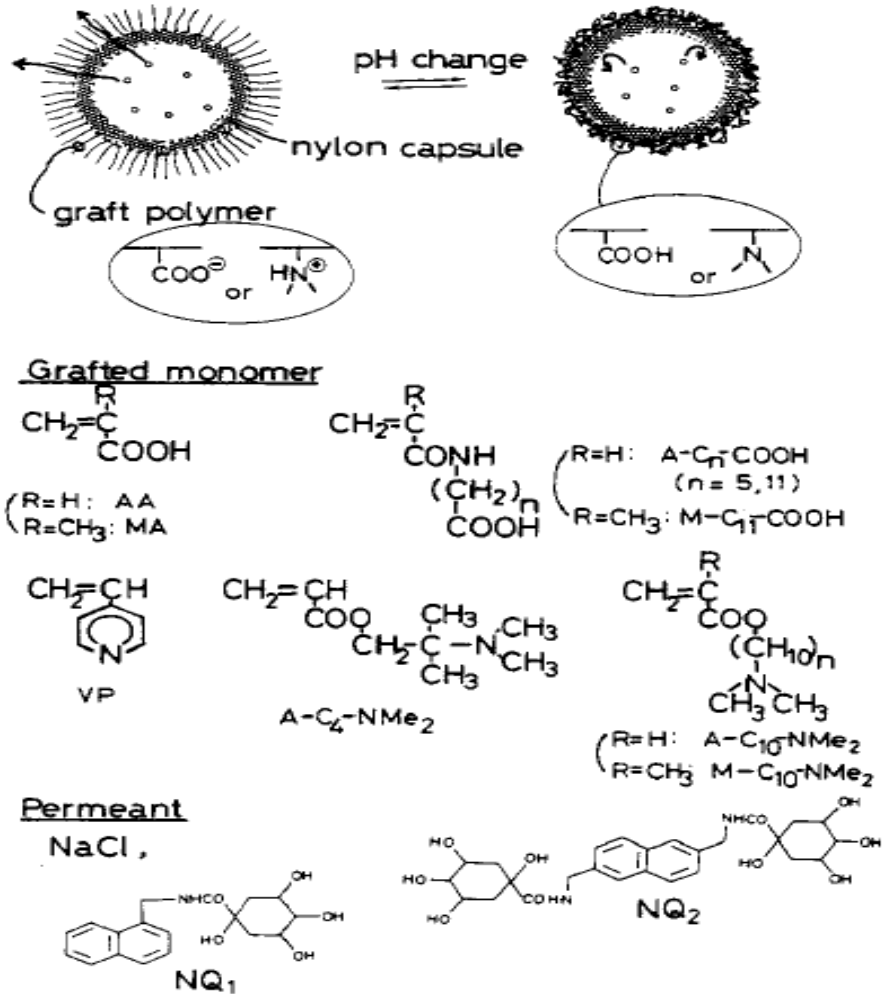

Figure 4.8. Schematic of the structure and functional nylon capsules [62].

Other functional capsule membranes have be also been designed that have capabilities to release large dyes in response to the changing pH of the outer medium[62]. Porous nylon capsule membrane with surface grafted-polyelectrolytes have been designed which respond to external pH[62]. The grafts act as permeation valves change in their conformation in response to the pH. The permeation of NaCl and water soluble naphthalene molecules was studied. Large nylon 2, 12 capsules were synthesized using ethylenediamine and 1,10-bis(chlorocarbonyl)decane by interfacial polymerization and the vinyl groups were grafted on to the surface. The permeation measurement was made by detecting the electrical conductance of the surrounding solution. The plot of specific conductance of different types of capsules shows the effect of grafting on the permeation rate. It was shown that the poly(vinly pyridine) (PVP) grafted capsules displayed faster NaCl permeation in pH 2 over a basic environment of pH 12. When poly(methacrylic acid) was grafted a reverse of what was observed for PVP grafted capsules was seen. The PVP grafted capsule membrane formed a higher barrier to NaCl permeation in the neutral pyridine form (pH >7) of the grafted polymer and not in the cationic pyridinium form (pH<6). The permeability of PMA grafter capsule

was decreased when the polymer was in the neutral carboxylic acid form (pH <5) and anionic carboxylate form (pH>6). The ungrafted original capsule did not show any signs of permeation at the whole pH 2-12 range. When the graft polymer is in the ionized form, the polymer chains are repelled by charge repulsion between ionic side chains or by hydrophilic properties which allow easy permeation of NaCl.

However, when the graft polymer is in the neutral form, the porous membrane was found to be covered by the entangled polymer, hence reducing the permeation significantly. It was concluded that the permeability controlled pH can be selected by the graft homo- or copolymers having dissociative side chains. The amount of NaCl permeation was also found to be dependent on the hydrophobicity of polymers. The valve of the graft polymers was also found to be dependent on the temperature[63] or redox reaction [64] in addition to the pH changes. One very similar study was done on a biomimetic membrane capsule used for drug delivery [65].

Akamatsu et al. [66] developed a novel method to obtain pH responsive core shell microcapsule reactors using plasma graft polymerization. The pH responsive gating function was achieved using a copolymer of N isopropylacrylamide and acrylic acid. The microcapsules that were formed were filled with glucose oxidase using the "bottle in" method. The responsiveness desired was achieved using the gating functionality of the copolymer formed in the pores of the shells using the plasma grafting technique. Figure 4.3 illustrates the mechanism of operation of the microcapsule reactors. The polymer in the pores, act as pH gates. The polymer hydrates at pH 5 and dehydrates at pH 4. Thus the microcapsules are designed such that they have a high rate of reaction at a high pH due to the increase in the diffusivity across the membrane. The FTIR spectra of the samples that were made showed characteristic peaks at 1650 and 1550 cm^{-1} which are characteristic of N isopropylacrylamide (NIPAM) and at 1720 cm^{-1} which is characteristic of acrylic acid (AA) confirming the formation of the copolymer of NIPAM and AA.

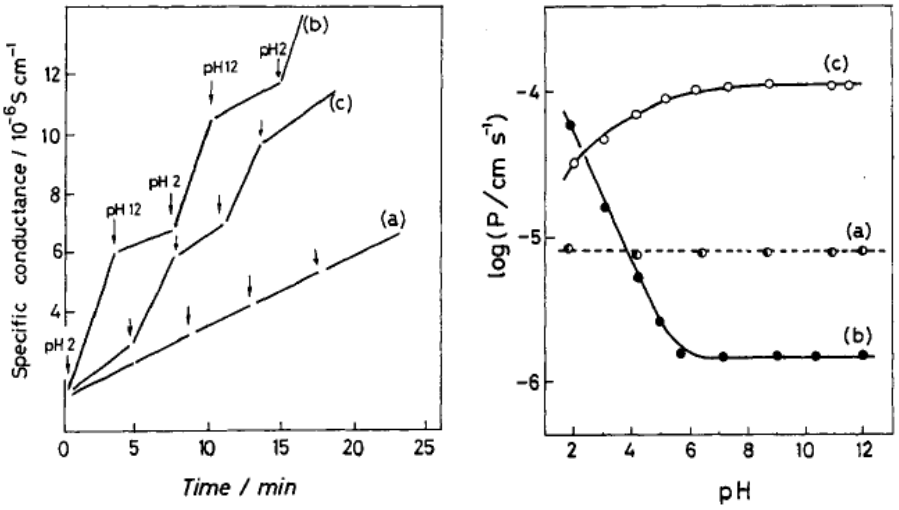

Figure 4.8. (a) pH sensitive permeation of NaCl responding to ambient pH changes at 25°C (b) pH-rate profiles of NaCl permeation at 25 °C. In both the plots (a) ungrafted capsules (b) PVP capsules (c) OMA capsules [62].

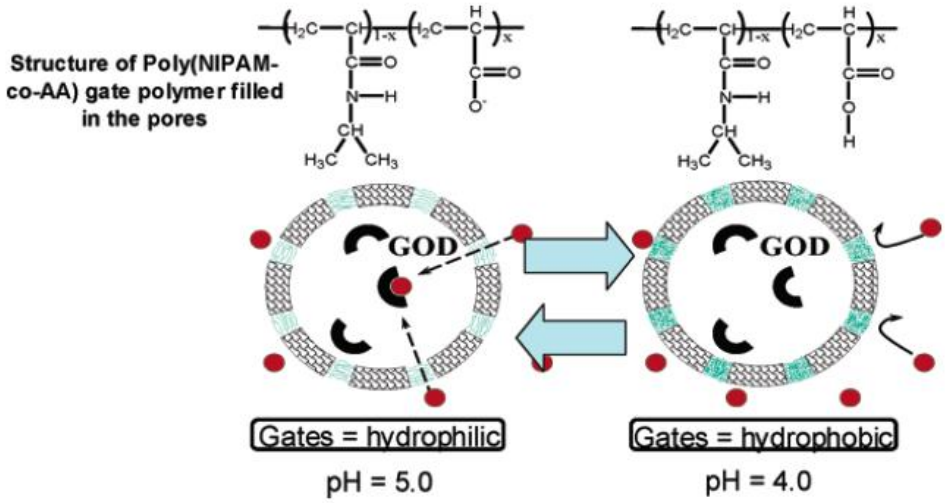

Figure 4.9. Schematic representation of the pH responsive microcapsules containing glucose oxidase (GOD) [66].

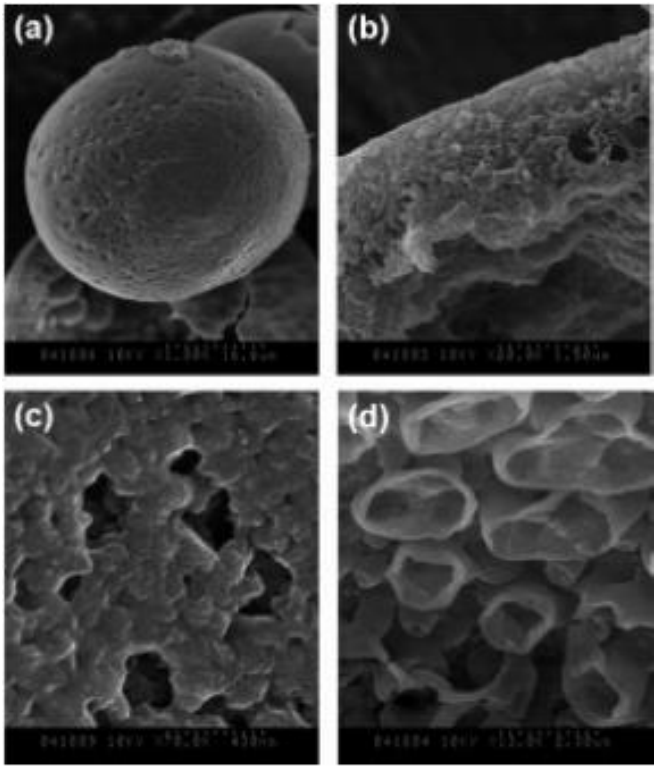

Figure 4.10. FE- SEM micrographs of core shell microcapsules showing (a) the general morphology (b) cross section (c) outer surface and (d) inner surface [66].

The performance of these microcapsule reactors was done by monitoring the amount of oxygen as it is the substrate of the reaction and it was seen that at a fixed temperature (40°C)

the reaction rate at pH 5 was 2.7 times higher than at pH 4. It can be explained by the fact that at pH 5 the pH responsive NIPAM - co – AA was in its hydrophilic state allowing the glucose to pass through the shell walls and the GOD reactions to take place and at pH 4 due to the hydrophobic state of the copolymer, the penetration of glucose through the pores was not assisted and hence the GOD reaction did not take place.

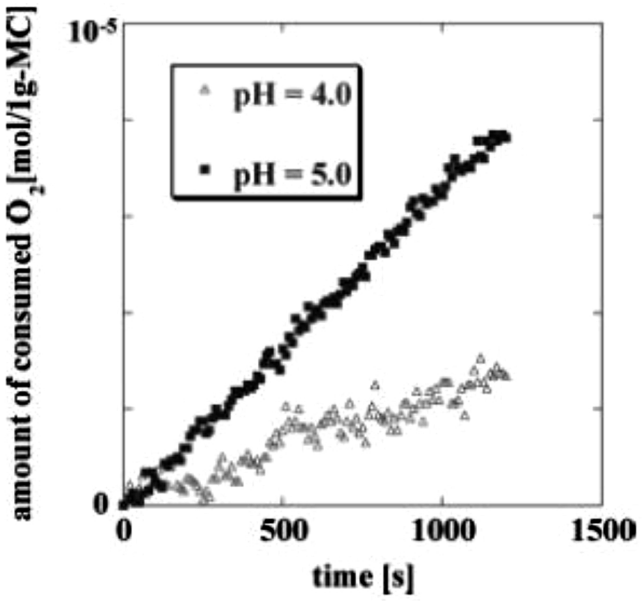

Figure 4.11. Amount of oxygen consumed by the pH responsive microcapsules [66].

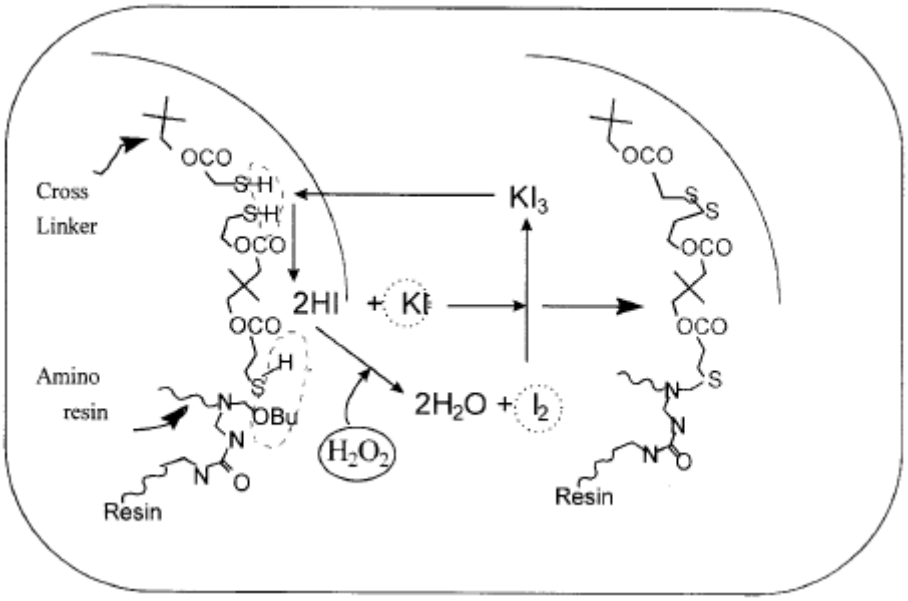

Figure 4.12. Schematic diagram illustrating disulfide linkages used in pH sensitive microcapsules [67].

Another chemistry that has been developed for pH sensitivity is the thiol chemistry[67]. Shirley et al. developed variable release microcapsules to encapsulate insecticides such as chloropyrifos or lambda- cyhalothrin or an herbicide butylate. The disulfide linkages undergo hydrolysis in the presence of hydroxyl groups. This is utilized in the variable release microcapsules.

5. MECHANICAL STIMULUS

Structural polymers are bound to be damaged due to formation of cracks and the location of such cracks is generally where the detection is difficult and repair almost impossible. The size and the length scales of such cracks also vary depending on the nature of stresses. The use of rubbery particles or rigid inorganic fillers to enhance the fracture toughness was one the ways used to enhance the toughness of the composites without losing the mechanical properties [68, 69]. The addition of such components to an existing coating adds more complexity to the coating. Brown et al.[70] showed that there was a 126% increase in the fracture toughness by the addition of glass microspheres into a matrix. Shukla et al. [71] showed a 200% rise in the fracture toughness using aluminum silicate microspheres. The use of microcapsules in a polymer matrix not only strengthens the matrix but also provide space for some kind of a healing agent. Polymeric microcapsules are mostly prepared using miniemulsion polymerization [72, 73] where submicron sized oil droplets are dispersed into a water phase. The majority of the self healing composites use urea formaldehyde walls and dicyclopentadiene as the liquid healing agent. The surface roughness added to the microcapsules synthesized using miniemulsion polymerization allows the dispersion of these into polymer matrices. The particle sizes of the synthesized microcapsules vary from 10–1000 μm with inner membranes that are 160–220 nm[74].

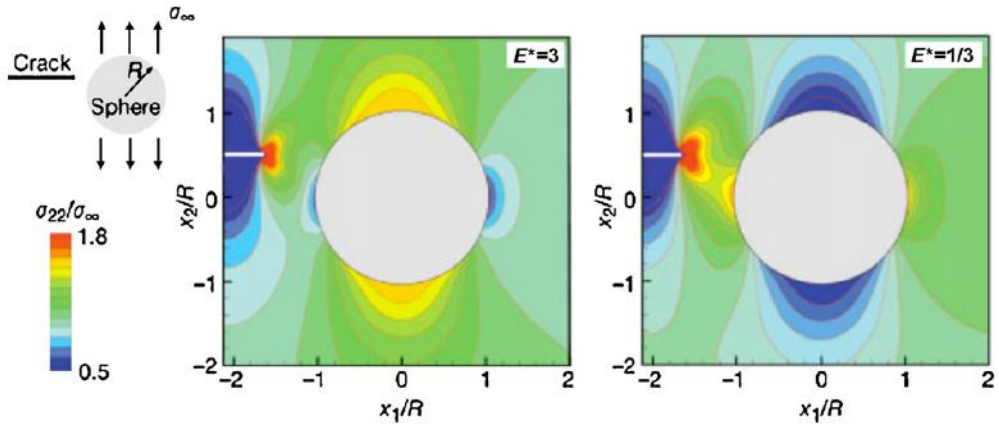

Figure 5.1. Stress state in the vicinity of a planar crack as it approaches a spherical filler particle embedded in a linearly elastic matrix. The image on the left corresponds to an inclusion three times stiffer than the surrounding matrix, and the image on the right corresponds to an inclusion three times more compliant than the surrounding matrix [76].

The trigger for the release of the healing agent is through mechanical rupture. It is also important that the microcapsules are fabricated with the sufficient wall thickness and with

optimum mechanical properties. Keller and Sottos determined the effect of the stiffness of the microcapsules and the stiffness of the surrounding medium and found that the stiffer the microcapsule walls more is the tendency of the crack to deflect away from the capsule [75]. It was also determined that more complaint shell wall tends to attract the crack towards the microcapsules.

The size of the microcapsules also plays an important role in the performance of the system. It determines the amount of healing agent available and also the toughness of the system. The microcapsule size is controlled by the rate of agitation during the encapsulation process. It has been reported that smaller the size of the microcapsules greater is the toughness of the system at lower concentrations[70]. In terms of the amount of healing agent delivered and the recovery efficiency it found that larger the microcapsules, more was the recovery due to a larger volume of the healing agent delivered to the system[77]. Since there is a tradeoff between the size and the amount of healing agent available, Brown et al. determined that the amount of best healing agent was delivered at 10 wt % of 386 μm sized microcapsules which translates to 4.5 mg of healing agent delivered per unit crack area. Blaiszik et al. [78] reported nanosized capsules as small as 220 nm made using ultrasonication and miniemulsion techniques.

The rate of healing and the kinetics of healing are very important as well because if the rate of crack growth is faster than the healing process itself then no healing would occur. Also since the healing is based on a catalyst aiding the reaction, if the rate of healing polymerization was faster than catalyst dissolution then recovery at isolated regions was observed. However, if the healing agent cured slowly and sufficient time was given, then maximum recovery of mechanical strength was seen[79]. The adhesion effects and the long term recovery effect was seen in case of carefully designed microcapsules [80].

One of the most thoroughly studied systems is the Dicyclopentadiene(DCPD)/Grubbs' catalyst system. Ring opening metathesis polymerization is initiated by the ruthenium (IV) catalyst which is responsible for the recovery of the damaged areas. White et al. designed such a system in 2001[76] which has been studied extensively.

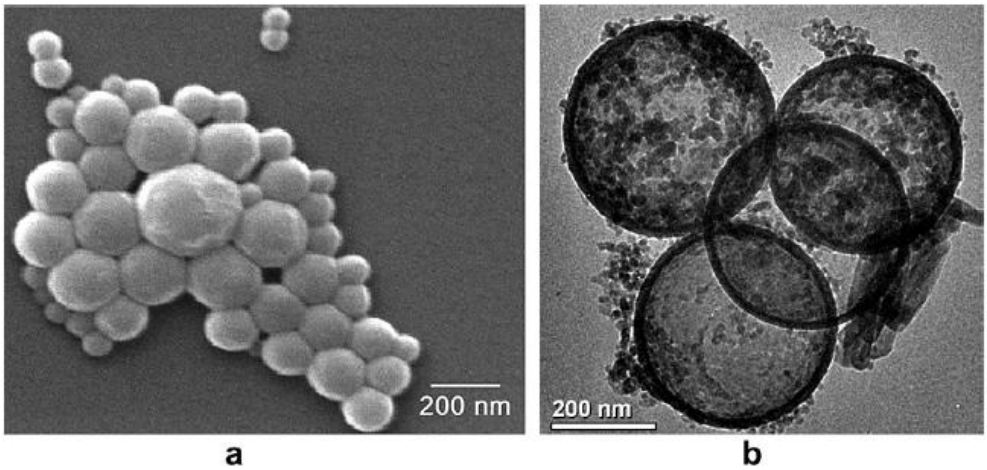

Figure 5.2. (a) SEM image of nanocapsules produced using hexadecane costabilizer (b) TEM image showing the core – shell morphology [78].

According to the system, the DCPD is incorporated in urea formaldehyde based microcapsules which are incorporated in a composite. When damage occurs, the crack propagates through the specimen and ruptures the microcapsules. Liquid healing agent would then flow through the crack via capillary action and upon contact with the catalyst would polymerize and fill up the crack restoring the mechanical strength of the material. In this study White et al. observed an increase in the load bearing capacity of neat epoxy. Initially, they also observed that there was a recovery of 75 % of the virgin fracture load. The testing that was used by this group was a tapered double cantilever beam, (TDCB) illustrated in the Figure 5.3. Three samples were made – reference samples, self activated samples and self healing samples. The reference sample was the one in which manual injection of the polymer was made. The reference sample showed about 51% recovery which was then optimized to 99% [81].

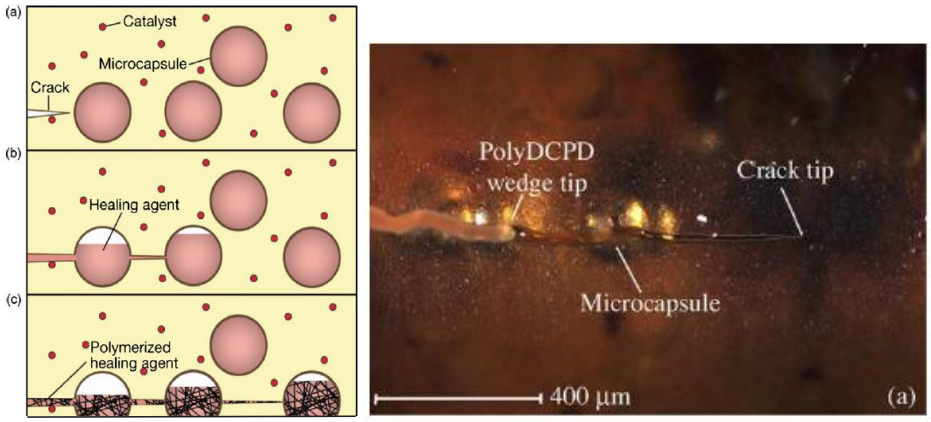

Figure 5.3. (a) Autonomous healing concept proposed by White et al.[76] (b) Optical micrograph image of the healing concept in action[82].

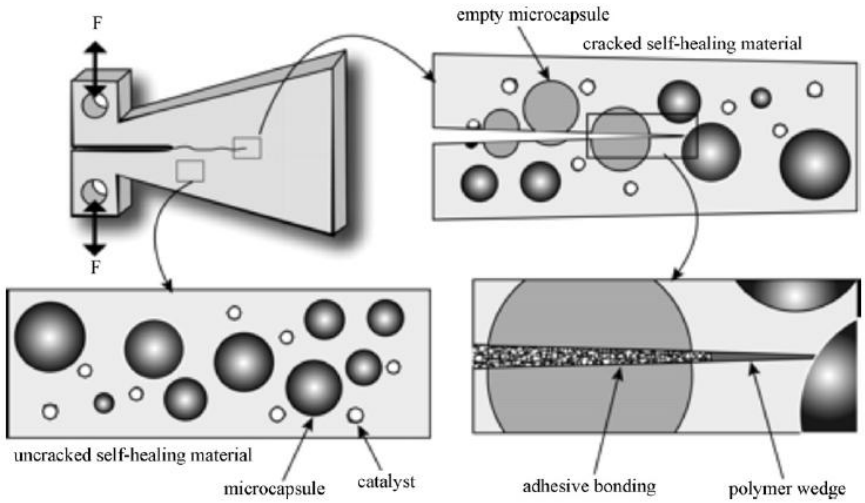

Figure 5.4. Schematic representation of the test parameters and the self healing process with in composite materials [79].

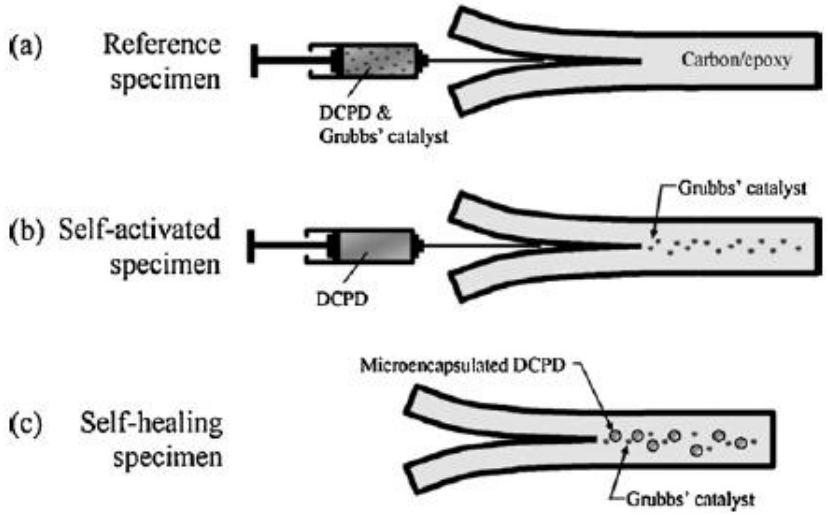

Figure 5.5. (a) Reference specimen where the premixed healing agent and the catalyst are injected into the damaged area (b) Self activated specimen where the catalyst is embedded into the epoxy and the DCPD is injected into the damaged area (c) self healing specimen where both the catalyst and the healing agent are embedded into the epoxy [81].

The self activated samples initially showed 20% recovery which was later optimized to 73% and the self healing autonomous samples showed 38% recovery and later were optimized to 66% after heating at 80 °C[81]. All the percent recoveries observed were average percent recoveries.

The fracture toughness of the epoxy coating is also something to be considered, the addition of the DCPD and the Grubbs' catalyst was found to increase the fracture toughness up to 15%. The use of other monomers in the microcapsules walls was also explored by Sun and Zhang [83]. They used melamine formaldehyde resin, urea formaldehyde resin and gelatin-gum arabic coacervate. They found that the gelatin microcapsules did not show breakage upon compression whereas the melamine formaldehyde and the urea formaldehyde microcapsule showed clear signs of rupture when compressed. Lie et al. explored the other monomers inside the capsule shell[84]. They tested a blend of two monomers as the healing agent while maintaining the desired mechanical properties as achieved by White et al. The polymerization was found to be faster with the addition of ethylene norbornene and was found to be completed using lesser amounts of the catalyst. Different catalysts have also been explored as far as the DCPD polymerization is considered by Wilson et al.[85]. An ideal catalyst is required to have rapid dissolution in the healing agent, fast initiation of polymerization, thermal stability, high processing and working temperature and chemical inertness to the surrounding matrix. The rate constants of the first generation Grubbs' catalyst was 1.45E-4 s^{-1} and 4.3E-3 s^{-1} for the second order Grubbs' catalyst and the rate was too fast to be measured for Hoveyda - Grubbs' catalyst. The robustness of the catalyst when exposed to the epoxy polymer matrix was also tested. The first generation Grubbs' catalyst was found to turn from purple to brown showing catalyst deactivation. The second generation Grubbs' catalyst showed color change from brown to green whereas the Hoveyda- Grubbs' catalyst was found to show no color change. The second order Grubbs' catalyst showed better thermal stability and hence better healing at 125°C.

Alternative to ruthenium catalysts have also been investigated but have found to be expensive and have limited availability. Kamphaus et al.[86] investigated tungsten (VI) catalyst as an alternative to ruthenium catalysts however the tungsten based catalysts showed lower fracture toughness and also the healing efficiency was found to be 20 % for an autonomous healing sample with 12 wt% WCl_6.

Other routes have also been explored due to the cost associated with the Grubbs' catalyst and the thermal stability. Cho et al. [87]have explored the possibility of poly(dimethylsiloxane) (PDMS) based self healing materials. The siloxane based healing agent was phase separated in the matrix while the catalyst was encapsulated throughout an epoxy matrix. This ensures an even distribution of the healing agent throughout the matrix and the catalyst has a better stability in the system. This system also uses the same idea proposed by White et al. [80].

By manual injection technique the upper limit of the healing was determined to be 24% for 3.6 wt % microcapsules. Following up with this study, Keller et al.[88, 89] proposed a new matrix that consisted of the PDMS instead of epoxy. The system that he proposed consisted of two separate types of microcapsules (1) high molecular weight vinyl functionalized PDMS and platinum catalyst complex (2) PDMS copolymer with active sites that would link to the vinyl functionalized PDMS. With this system 75% healing efficiency was obtained with 10 wt% resin and 5 wt% initiator capsules. Interestingly, some samples showed an efficiency of 100% or greater because of the fact that the matrix was similar to the healing agent and hence the crack could propagate via different pathways.

Following the same train of thought, scientist has also tried incorporating epoxy/hardener microcapsules into an epoxy matrix. Yin et al.[90] were the first to try the epoxy hardener system which contained an uncured epoxy resin and imidazole-metal hardener. 30 – 70 micron size particles were obtained and urea formaldehyde was used as the shell wall material. Even though the incorporation of the two in an epoxy matrix increased the fracture toughness, the system in use was not fully autonomous.

The imidazole metal hardener requires a temperature range of 130°C. However, the healing efficiency for this system was found to be 111 % using 10 wt % epoxy microcapsules and 2 wt% latent hardener. Yaun et al. [91] designed a fully autonomous system with epoxy resin as the healing agent and mercaptan as the hardener.

The maximum healing was found to occur when the ratio of the microcapsules was kept at 1:1 and was found to level off with the addition of 5 wt% microcapsules. Efficiencies of over 100 % were achieved and reason for this was found to be similar to that of the PDMS based microcapsules. It was also seen that the healing could be achieved at a lower temperatures of the order of 0 – 10 °C with an efficiency of 86% thus broadening the operating temperature range of these capsules. The diameter of the particles that have been synthesized could also be controlled by adjusting the pH, concentration of the surfactants, the time and the heating rates during the microencapsulation process[92]. More chemically resistant and stable polythiol capsules have also been encapsulated in melamine formaldehyde [93]. Isocyanates are the latest addition to the chemicals that have been encapsulated which can react when exposed to humid or wet environments to mimic healing. Isophorone diisocyanate has been encapsulated and has shown stability over time [94]. Healing by many solvents [40, 41, 95, 96] has also been one of the not so explored areas.

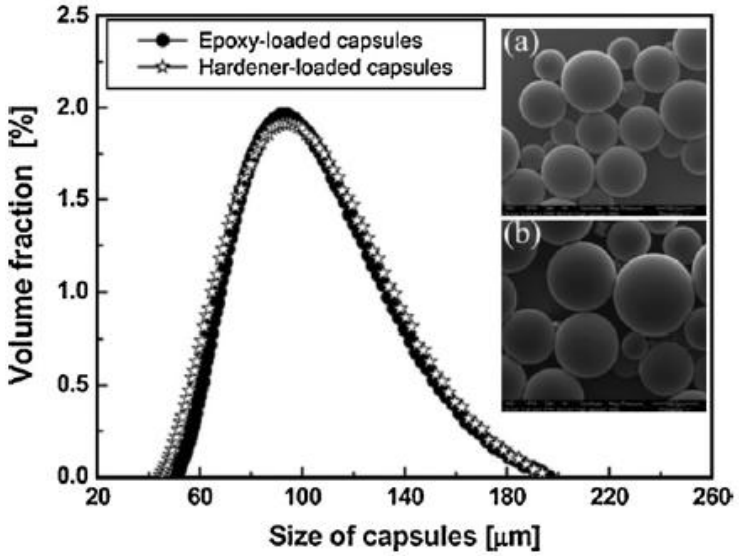

Figure 5.6. Size distributions and SEM images of (a) epoxy loaded capsules (b) mercaptan loaded capsules [91].

Lin et al. showed that solvent could be used to promote healing during the wetting and diffusion stages. Wetting here means the swelling of the bulk polymer and the interlocking of the polymer chains across the defect. It was determined that by dissolving the polymer in various solvents the glass transition temperature could be lowered allowing the material to heal at a lower temperature. Caruso et al. [97] incorporated solvent capsules in a polymer matrix and determined that the healing efficiency was directly proportional to solvent polarity in the dielectric constant range on 32-47. It was also determined that the solvents were difficult to incorporate in the urea formaldehyde capsules however chlorobenzene was successfully incorporated and showed efficiencies of the order of 86% for 20 wt% of the capsules. Microcapsules with oil core have been synthesized fairly on a large scale and researched extensively. However, another challenge in the field of incorporation is formation of water core microcapsules. Loxley et al.[98] synthesized poly (methylmethacrylate) microcapsules with water to be core liquid. The water core microcapsules are fairly difficult to synthesize as the spreading coefficients are to be taken into account while formulating the emulsion. The various particle morphologies can be obtained with different spreading coefficients. Torza and Mason [99] have investigated the equilibrium morphology adopted by droplets of immiscible liquids (phases 1 and 3) when brought in contact with a mutually immiscible liquid (phase 2). The three possible combinations as stated by them are as follows,

$$S_1 < 0\,; S_2 < 0; S_3 > 0 \quad (1)$$
$$S_1 < 0\,; S_2 < 0; S_3 < 0 \quad (2)$$
$$S_1 < 0\,; S_2 > 0; S_3 < 0 \quad (3)$$

where S is the spreading coefficient of the given phase. If the conditions in eq. 1 are satisfied then core shell morphology were obtained, the eq. 2 gave rise to “acorn” shaped particles and the eq. 3 gave two separate droplets.

The technique used for the encapsulation of water in the cores of the polymer capsules is achieved using a technique known as internal phase separation. An o/w emulsion was prepared which consists of the oil phase, the mixture of the polymers, high boiling poor solvent and the low boiling poor solvent.

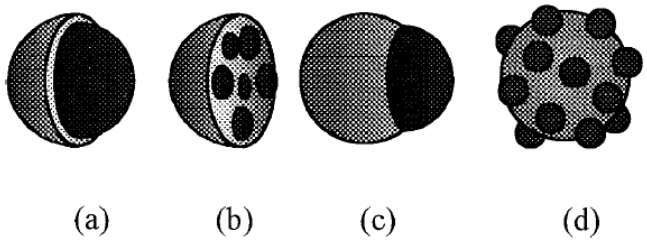

Figure 5.7. Four possible two phase morphologies (a) core shell (b) occluded (c) acorn (d) hetroaggregate [98].

A suitable emulsifier was used to disperse the mixture and form an emulsion. The mixture is then subjected to reduced pressure and elevated temperature to remove the good solvent. Thus polymerization takes place around the non-solvent and hence encapsulates it. Tiarks et al. [72] used the similar technique and reported the formation of nano sized particles. Since water can be encapsulated a large array of water soluble compounds could also be potentially incorporated using this technique.

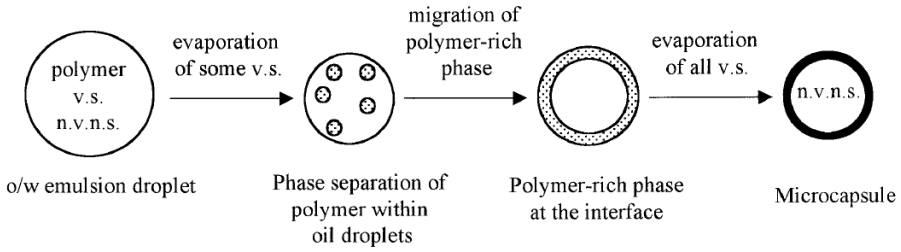

Figure 5.8. Schematic steps involved in the internal phase separation process. N.v.n.s – nonvolatile nonsolvent v.s- volatile solvent [100].

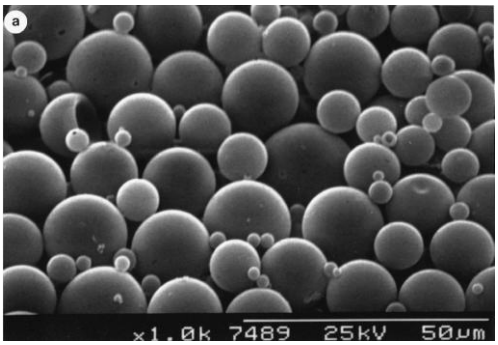

Figure 5.9. Electron micrographs of microcapsules produced from pre emulsions containing no acetone in the oil phase [98].

6. PHOTO STIMULUS

Photoinitiated cycloaddition reactions which undergo cyclization upon irradiation of a certain wavelength of light and cleavage upon irradiation with certain other smaller wavelength of light are used in the photo initiated damage recovery. Chung et al. [101] incorporated cinnamoyl groups into a polymer system leading to photochemically induced healing systems. The polymer networks can also be crosslinked via photochemical cycloaddition of the cinnamoyl groups to form cyclobutane dimers. Due to the high ring stain in the cyclobutane groups, it was assumed to break when the crack propagated within the specimen. When wavelengths greater than 310 nm was shined on the specimen the cyclobutane crosslinks were formed hence restoring the mechanical strength of the specimen. IR spectroscopy was used to confirm the same. The highest efficiency that was around 14% and it was found to increase to 26% when both photochemical and thermal healing was used together.

Another interesting development recently reported by Pastine et al. [102] was the phototriggerable microcapsules. The phototriggerable microcapsules contained optothermally active species, such as carbon nanotubes, which could rapidly heat up the liquid content and cause rupture due to increase in the internal pressure. The microcapsules in the range of 100-1000 microns were synthesized which could be released optothermally by using a laser irradiation to release the incorporated toluene. The duration of exposure was a low as 0.02 s.

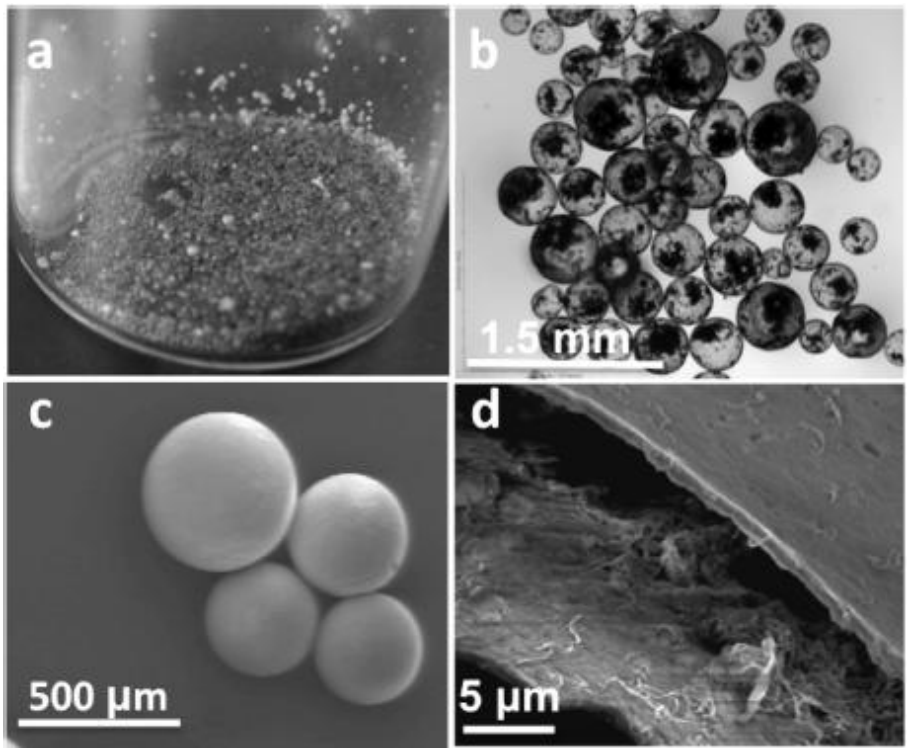

Figure 6.1. Toluene filled microcapsules containing 1 wt% CNT. (a) Optical image of the scintillation vail (b) Optical image of the microcapsules in oil (c) SEM image of the microcapsules (d) SEM images of crushed microcapsules with visible interiors[102].

SUMMARY

Self healing using microcapsules has become one of the most interesting and ever growing areas of research with new and more interesting publications every year. Microencapsulation has proved to be a successful and useful technique in the fields of pharmaceuticals sciences and has found many applications in the field of organic coatings as well. Even though the technology has been explored a lot in many fields of science the area of organic coatings still remains untouched. Thus, the use of this technique for many different applications such as anticorrosives, mechanical strength healants etc. are still to be explored. While some methods in this field are very well studied and understood there are new ones that need to be understood. Some of the well known methods are now looking at optimization and commercialization whereas the ones that have been discovered now will someday be commercialized. The use of various stimuli to trigger and use of various materials to make cheaper and more versatile microcapsules are the driving forces of this field of science. Some of the challenges such as thermal stability and ease in application are areas that require attention. As researchers deepen their understanding of various techniques and broaden the number of attainable materials the field of encapsulation grows.

ACKNOWLEDGMENTS

The authors would like to thank Army Research Labs (Contract Nos. W911NF-04-2-0029 and W911NF-09-2-0014) for funding.

REFERENCES

[1] Baer, D.R., P.E. Burrows, and A.A. El-Azab, Enhancing coating functionality using nanoscience and nanotechnology. *Progress in Organic Coatings*, 2003. 47(3-4): p. 342-356.

[2] Weiner, S. and H.D. Wagner, THE MATERIAL BONE: Structure-Mechanical Function Relations. *Annual Review of Materials Science*, 1998. 28(1): p. 271-298.

[3] Lloyd, P., Requirements for smart materials. Proceedings of the Institution of Mechanical Engineers, *Part G: Journal of Aerospace Engineering*, 2007. 221(4): p. 417-478.

[4] Zhou, B.L., Some progress in the biomimetic study of composite materials. *Materials Chemistry and Physics*, 1996. 45(2): p. 114-119.

[5] Shyni, V., L. Ashish, and M. Raghunath, Metal-ion-mediated healing of gels. *Journal of Polymer Science Part A: Polymer Chemistry*, 2006. 44(1): p. 666-670.

[6] Toohey, K.S., et al., Self-healing materials with microvascular networks. *Nat Mater*, 2007. 6(8): p. 581-585.

[7] Dr. Swapan Kumar, G., Self-Healing Materials: Fundamentals, Design Strategies, and Applications. Self-Healing Materials, 2009: p. 1-28.

[8] Monique Seiller, Anne-Marie Orecchioni, and M.-C. Martini, in *Microencapsulation*: *Methods and Industrial Applications*, S. Benita, Editor. 1996, Marcel Dekker. p. 707-745.

[9] Park, S.-J., Y.-S. Shin, and J.-R. Lee, Preparation and Characterization of Microcapsules Containing Lemon Oil. *Journal of Colloid and Interface Science*, 2001. 241(2): p. 502-508.
[10] Fanger, G.O., What good are microcapsules? *Chemtech*, 1974. 4: p. 397-405.
[11] Bakan, J.A., Process for making capsules and method of making premix used therein. 1969, *The National Cash Register Company*: United States, US pat.no. 3436355.
[12] Paul D, R., Polymers in Controlled Release Technology, in Controlled Release Polymeric Formulations. 1976, *American Chemical Society*. p. 1-14.
[13] Jae Hyung Park, M. Ye, and K. Park, Biodegradable Polymers for Microencapsulation of Drugs. *Molecules*, 2005. 10: p. 146-161.
[14] Farahidah, M. and F.v.d.W. Christopher, Engineering biodegradable polyester particles with specific drug targeting and drug release properties. *Journal of Pharmaceutical Sciences*, 2008. 97(1): p. 71-87.
[15] Tamber, H., et al., Formulation aspects of biodegradable polymeric microspheres for antigen delivery. *Advanced Drug Delivery Reviews*, 2005. 57(3): p. 357-376.
[16] Gharsallaoui, A., et al., Applications of spray-drying in microencapsulation of food ingredients: An overview. *Food Research International*, 2007. 40(9): p. 1107-1121.
[17] Sanguansri, P. and M.A. Augustin, Nanoscale materials development - a food industry perspective. *Trends in Food Science and Technology*, 2006. 17(10): p. 547-556.
[18] Swapan Kumar, G., Functional Coatings and Microencapsulation: A General Perspective, in *Functional Coatings*, G. Dr. Swapan Kumar, Editor. 2006. p. 1-28.
[19] Martin, W., W. Anja, and R. Oliver, Coatings with self-cleaning properties. *Macromolecular Symposia*, 2002. 187(1): p. 459-468.
[20] Pérez, M., et al., Core-shell pigments in antifouling paints. *Surface Coatings International Part B: Coatings Transactions*, 2003. 86(4): p. 259-262.
[21] Edwin, N., O. Markus, and S. Bernhard, Lotus-Effect- surfaces. *Macromolecular Symposia*, 2002. 187(1): p. 677-682.
[22] Yuyang Liu, et al., Artificial lotus leaf structures from assembling carbon nanotubes and their applications in hydrophobic textiles. *J. Mater. Chem*., 2007. 17: p. 1071 - 1078.
[23] Amerio, E., et al., Scratch resistance of nano-silica reinforced acrylic coatings. *Progress in Organic Coatings*, 2008. 62(2): p. 129-133.
[24] Sangermano, M., et al., Scratch resistant tough nanocomposite epoxy coatings based on hyperbranched polyesters. *Polymer*, 2009. 50(24): p. 5647-5652.
[25] Rudifer Baum, et al., *Coating material with biocide microcapsules*, T. GmbH, Editor. 2008. p. 7.
[26] Kuhr, M., et al., Coatings on plastics with the PICVD technology. *Thin Solid Films*, 2003. 442(1-2): p. 107-116.
[27] Kumar, A., L.D. Stephenson, and J.N. Murray, Self-healing coatings for steel. *Progress in Organic Coatings*, 2006. 55(3): p. 244-253.
[28] Sauvant-Moynot, V., S. Gonzalez, and J. Kittel, Self-healing coatings: An alternative route for anticorrosion protection. *Progress in Organic Coatings*, 2008. 63(3): p. 307-315.
[29] Brown, H.R., V.R. Deline, and P.F. Green, Evidence for cleavage of polymer chains by crack propagation. *Nature*, 1989. 341(6239): p. 221-222.

[30] Michel, J., J.A. Manson, and R.W. Hertzberg, A simple viscoelastic model for fatigue crack propagation in polymers as a function of molecular weight. *Polymer*, 1984. 25(11): p. 1657-1666.

[31] Morgan, R.J. and J.E. O'Neal, The microscopic failure processes and their relation to the structure of amine-cured bisphenol-A-diglycidyl ether epoxies. *Journal of Materials Science*, 1977. 12(10): p. 1966-1980.

[32] Osswald T and M. G., Failure and damage of polymers, in *Material science of polymers for engineers*, Osswald T and M. G., Editors. 2003, Hanser Publishers: Munich. p. 447-519.

[33] Sauer, J. and G. Richardson, Fatigue of polymers. *International Journal of Fracture*, 1980. 16(6): p. 499-532.

[34] Bloyer, D., R. Ritchie, and K. Venkateswara Rao, Fatigue-crack propagation behavior of ductile/brittle laminated composites. *Metallurgical and Materials Transactions A*, 1999. 30(3): p. 633-642.

[35] Yousefpour, A., M. Hojjati, and J.-P. Immarigeon, Fusion Bonding/Welding of Thermoplastic Composites. *Journal of Thermoplastic Composite Materials*, 2004. 17(4): p. 303-341.

[36] Boiko, Y.M., et al., Healing of interfaces of amorphous and semi-crystalline poly(ethylene terephthalate) in the vicinity of the glass transition temperature. *Polymer*, 2001. 42(21): p. 8695-8702.

[37] Shen Jane-Sang , Harmon Julie P. , and S. Lee, Thermally-induced crack healing in poly(methyl methacrylate). Journal of materials research 2002. 17(6): p. 1335-1340.

[38] Kim, H.J., K.-J. Lee, and H.H. Lee, Healing of fractured polymers by interdiffusion. Polymer, 1996. 37(20): p. 4593-4597.

[39] Avramova, N., Study of the healing process of polymers with different chemical structure and chain mobility. *Polymer*, 1993. 34(9): p. 1904-1907.

[40] Hsieh, H.-C., T.-J. Yang, and S. Lee, Crack healing in poly(methyl methacrylate) induced by co-solvent of methanol and ethanol. *Polymer*, 2001. 42(3): p. 1227-1241.

[41] Wang, P.P., S. Lee, and J.P. Harmon, Ethanol-induced crack healing in poly(methyl methacrylate). *Journal of Polymer Science Part B: Polymer Physics*, 1994. 32(7): p. 1217-1227.

[42] Stubblefield, M.A., et al., Development of heat-activated joining technology for composite-to-composite pipe using prepreg fabric. *Polymer Engineering and Science*, 1998. 38(1): p. 143-149.

[43] Chen, J.-S., C.K. Ober, and M.D. Poliks, Characterization of thermally reworkable thermosets: materials for environmentally friendly processing and reuse. *Polymer*, 2002. 43(1): p. 131-139.

[44] Chen, J.-S., et al., Controlled degradation of epoxy networks: analysis of crosslink density and glass transition temperature changes in thermally reworkable thermosets. *Polymer*, 2004. 45(6): p. 1939-1950.

[45] Yang, S., et al., Reworkable Epoxies: Thermosets with Thermally Cleavable Groups for Controlled Network Breakdown. *Chemistry of Materials*, 1998. 10(6): p. 1475-1482.

[46] Paul, J. and R. Jones, Repair of impact damaged composites. *Engineering Fracture Mechanics*, 1992. 41(1): p. 127-141.

[47] Soutis, C., D.M. Duan, and P. Goutas, Compressive behaviour of CFRP laminates repaired with adhesively bonded external patches. *Composite Structures*, 1999. 45(4): p. 289-301.
[48] Zimmerman, K. and D. Liu, An experimental investigation of composite repair. *Experimental Mechanics*, 1996. 36(2): p. 142-147.
[49] Tse, P.-C., K.-J. Lau, and W.-H. Wong, Stress and failure analysis of woven composite plates with adhesive patch-reinforced circular hole. *Composites Part B: Engineering*, 2002. 33(1): p. 57-65.
[50] Zwaag, S., An Introduction to Material Design Principles : Damage Prevention versus Damage Management, in *Self Healing Materials*. 2008. p. 1-18.
[51] Zwaag, S., Self Healing Polymer Coatings, in *Self Healing Materials*. 2008. p. 142-143.
[52] R. P. Wool and K.M. O'Connor, A theory crack healing in polymers. *Journal of Applied Physics*, 1981. 52: p. 5953 - 5964.
[53] Kiran Bhat Kashi, et al., *Responsive microcapsules for corrosion inhibition*, in 2009 DoD Corrosion Conference. 2009, NACE: Washington D.C, US. p. 10.
[54] Decher, G., Fuzzy Nanoassemblies: Toward Layered Polymeric Multicomposites. *Science*, 1997. 277(5330): p. 1232-1237.
[55] Decher, G., J.D. Hong, and J. Schmitt, Buildup of ultrathin multilayer films by a self-assembly process: III. Consecutively alternating adsorption of anionic and cationic polyelectrolytes on charged surfaces. *Thin Solid Films*, 1992. 210-211(Part 2): p. 831-835.
[56] Yasakau, K.A., et al., Mechanism of Corrosion Inhibition of AA2024 by Rare-Earth Compounds. *The Journal of Physical Chemistry B*, 2006. 110(11): p. 5515-5528.
[57] Zheludkevich, M.L., et al., Anticorrosion Coatings with Self-Healing Effect Based on Nanocontainers Impregnated with Corrosion Inhibitor. *Chemistry of Materials*, 2007. 19(3): p. 402-411.
[58] Shchukin, D.G., et al., Active Anticorrosion Coatings with Halloysite Nanocontainers. *The Journal of Physical Chemistry* C, 2008. 112(4): p. 958-964.
[59] Shchukin, D., et al., Layer-by-Layer Assembled Nanocontainers for Self-Healing Corrosion Protection. *Advanced Materials*, 2006. 18(13): p. 1672-1678.
[60] Cui, J., Y. Liu, and J. Hao, Multiwalled Carbon-Nanotube-Embedded Microcapsules and Their Electrochemical Behavior. *The Journal of Physical Chemistry* C, 2009. 113(10): p. 3967-3972.
[61] Kuang, F., et al., Microencapsulation technology for thiourea corrosion inhibitor. *Journal of Solid State Electrochemistry*, 2009. 13(11): p. 1729-1735.
[62] Okahata, Y., H. Noguchi, and T. Seki, Functional capsule membranes. 26. Permeability control of polymer-grafted capsule membranes responding to ambient pH changes. *Macromolecules*, 1987. 20(1): p. 15-21.
[63] Okahata, Y., H. Noguchi, and T. Seki, Thermoselective permeation from a polymer-grafted capsule membrane. *Macromolecules*, 1986. 19(2): p. 493-494.
[64] Yoshio Okahata, Katsuhiko Ariga, and T. Seki, Redox-sensitive permeation from a capsule membrane grafted with viologen-containing polymers. *J. Chem. Soc., Chem. Commun.*, 1986: p. 73.
[65] An, Z., H. Möhwald, and J. Li, pH Controlled Permeability of Lipid/Protein Biomimetic Microcapsules. *Biomacromolecules*, 2006. 7(2): p. 580-585.

[66] Akamatsu, K. and T. Yamaguchi, Novel Preparation Method for Obtaining pH-Responsive Core−Shell Microcapsule Reactors. *Industrial and Engineering Chemistry Research*, 2006. 46(1): p. 124-130.
[67] Ian Malcolm Shirley, et al., *Variable Release Microcapsules*. 2002, Syngenta Ltd: United States.Us Pat. No.6485736.
[68] Azimi, H.R., R.A. Pearson, and R.W. Hertzberg, Fatigue of hybrid epoxy composites: Epoxies containing rubber and hollow glass spheres. *Polymer Engineering and Science*, 1996. 36(18): p. 2352-2365.
[69] Bagheri, R. and R.A. Pearson, Role of particle cavitation in rubber-toughened epoxies: 1. Microvoid toughening. *Polymer*, 1996. 37(20): p. 4529-4538.
[70] Brown, E.N., S.R. White, and N.R. Sottos, Microcapsule induced toughening in a self-healing polymer composite. *Journal of Materials Science*, 2004. 39(5): p. 1703-1710.
[71] Cardoso, R.J., A. Shukla, and A. Bose, Effect of particle size and surface treatment on constitutive properties of polyester-cenosphere composites. *Journal of Materials Science*, 2002. 37(3): p. 603-613.
[72] Tiarks, F., K. Landfester, and M. Antonietti, Preparation of Polymeric Nanocapsules by Miniemulsion Polymerization. *Langmuir*, 2001. 17(3): p. 908-918.
[73] Asua, J.M., Miniemulsion polymerization. *Progress in Polymer Science*, 2002. 27(7): p. 1283-1346.
[74] E. N. Brown, et al., In situ poly(urea-formaldehyde) microencapsulation of dicyclopentadiene. *Journal of Microencapsulation*, 2003. 20(6): p. 719-730.
[75] Keller, M. and N. Sottos, Mechanical Properties of Microcapsules Used in a Self-Healing Polymer. *Experimental Mechanics*, 2006. 46(6): p. 725-733.
[76] White, S.R., et al., Autonomic healing of polymer composites. *Nature*, 2001. 409(6822): p. 794-797.
[77] Rule, J.D., N.R. Sottos, and S.R. White, Effect of microcapsule size on the performance of self-healing polymers. *Polymer*, 2007. 48(12): p. 3520-3529.
[78] Blaiszik, B.J., N.R. Sottos, and S.R. White, Nanocapsules for self-healing materials. *Composites Science and Technology*, 2008. 68(3-4): p. 978-986.
[79] Jones, A.S., et al., Life extension of self-healing polymers with rapidly growing fatigue cracks. *Journal of the Royal Society Interf*ace, 2007. 4(13): p. 395-403.
[80] Brown, E.N., S.R. White, and N.R. Sottos, Retardation and repair of fatigue cracks in a microcapsule toughened epoxy composite - Part I: Manual infiltration. *Composites Science and Technology*, 2005. 65(15-16): p. 2466-2473.
[81] Kessler M R., Sottos N R., and W.S. R., Self-healing structural composite materials. Composites Part A : *Applied science and manufacturing*, 2003. 34: p. 743-753.
[82] Brown E N., S.R. White, and N.R.Sottos., Retardation and repair of fatigue craacks in a microcapsule toughened epoxy composite : *Part II : In situ self - healing. Compositedd science and technology*, 2005. 65: p. 2474-2480.
[83] Sun G. and Zhang Z., Mechanical strength of microcapsules made of different wall materials. *International journal of pharmaceutics*, 2002. 242(1-2): p. 307-311.
[84] Liu, X., et al., Characterization of diene monomers as healing agents for autonomic damage repair. *Journal of Applied Polymer Science*, 2006. 101(3): p. 1266-1272.
[85] Wilson Gerald O., et al., Evaluation of Ruthenium Catalysts for Ring-Opening Metathesis Polymerization-Based Self-Healing Applications. *American Chemical Society*, 2008. 20(10): p. 3288-3297.

[86] Kamphaus, J.M., et al., A new self-healing epoxy with tungsten (VI) chloride catalyst. *Journal of the Royal Society Interface*, 2008. 5(18): p. 95-103.
[87] Soo Hyoun Cho, et al., Polydimethylsiloxane- based self healing materials. *Advanced Materials,* 2006. 18: p. 997-1000.
[88] Keller M W., White S R, and Sottos N R., A self healing poly(dimethylsiloxane) elastomer. *Advanced Funtional Materials*, 2007. 17: p. 2399-2404.
[89] Keller M W., White S R., and N. R. Sottos, Torsion fatigue response of self-healing poly(dimethylsiloxane) elastomers. *Polymer*, 2008. 49(3136-3145).
[90] Yin, T., et al., Self-healing epoxy composites - Preparation and effect of the healant consisting of microencapsulated epoxy and latent curing agent. *Composites Science and Technology*, 2007. 67(2): p. 201-212.
[91] Yuan, Y.C., et al., Self-Healing Polymeric Materials Using Epoxy/Mercaptan as the Healant. *Macromolecules*, 2008. 41(14): p. 5197-5202.
[92] Yuan, L., et al., Preparation and characterization of poly(urea-formaldehyde) microcapsules filled with epoxy resins. *Polymer*, 2006. 47(15): p. 5338-5349.
[93] Yuan, Y.C., M.Z. Rong, and M.Q. Zhang, Preparation and characterization of microencapsulated polythiol. *Polymer*, 2008. 49(10): p. 2531-2541.
[94] Jinglei Yang, et al., Microencapsulation of Isocyanates for Self-Healing Polymers. *Macromolecules*, 2008. 41: p. 9650-9655.
[95] Lin, C.B., S. Lee, and K.S. Liu, Methanol-Induced crack healing in poly(methyl methacrylate). *Polymer Engineering and Science*, 1990. 30(21): p. 1399-1406.
[96] Wu, T. and S. Lee, Carbon tetrachloride-induced crack healing in polycarbonate. *Journal of Polymer Science Part B: Polymer Physics*, 1994. 32(12): p. 2055-2064.
[97] Caruso, M.M., et al., Solvent-Promoted Self-Healing Epoxy Materials. *Macromolecules*, 2007. 40(25): p. 8830-8832.
[98] Loxley, A. and B. Vincent, Preparation of Poly(methylmethacrylate) Microcapsules with Liquid Cores. *Journal of Colloid and Interface Science*, 1998. 208(1): p. 49-62.
[99] Torza, S. and S.G. Mason, Three-phase interactions in shear and electrical fields. *Journal of Colloid and Interface Science*, 1970. 33(1): p. 67-83.
[100] Atkin, R., et al., Preparation of Aqueous Core/Polymer Shell Microcapsules by Internal Phase Separation. *Macromolecules*, 2004. 37(21): p. 7979-7985.
[101] Chung, C.-M., et al., Crack Healing in Polymeric Materials via Photochemical [2+2] Cycloaddition. *Chemistry of Materials*, 2004. 16(21): p. 3982-3984.
[102] Pastine, S.J., et al., Chemicals on Demand with Phototriggerable Microcapsules. *Journal of the American Chemical Society*, 2009. 131(38): p. 13586-13587.

Smart Nanocomposites
Volume 2, Number 1
ISSN: 1949-4823

ULTIMATE RESOLUTION ACHIEVABLE WITH FOCUSED ION BEAMS: COMPARING COMPUTER SIMULATIONS WITH PRACTICAL PROCESS

***L. G. Turatti*[a,b], *J. W. Swart*[a,b,c], *A. R. Vaz*[a,c] and *S. A. Moshkalev*[a]**

[a]Center for Semiconductor Components – CCS,
State University of Campinas - Unicamp, Campinas,
SP 13083-870, Brazil
[b]School of Electrical and Computer Engineering - FEEC,
Department of Semiconductors, Instruments and Photonic - DSIF,
State University of Campinas -Unicamp, Campinas,
SP 13083-970, Brazil
[c]Center for Information Technology Renato Archer,
Campinas, SP, Brazil.

ABSTRACT

Simulation results for Ga ion beam interaction with thin membranes of different materials (C, Si, Pt) are presented. Experiments with ion beam irradiation were carried out at different doses with suspended 50-100 nm thick multi-layer graphene (MLG) flakes. Cross-sectioning using focused ion beam milling revealed that material removal occurs in areas 60-80 nm wide at the beam lateral dimension of 20 nm, being consistent with the results of TRIM simulations. Further studies with thinner MLG samples are in progress to achieve better ion beam processing resolution.

1. INTRODUCTION

Many nanodevices can be fabricated using focused ion beams (FIB) on thin membranes where ion beam-solid interaction occurs in a limited volume potentially enabling fabrication at smaller dimensions. In the FIB based nanofabrication, secondary processes resulting from collision cascades of incident ion in a solid play a critical role in the achievable patterning resolution. These processes effectively result in lateral spreading of the beam energy over areas much wider than the incident beam, affecting the resolution obtained in milling, ion

induced etching and deposition processes. Fabricated structures thus usually have lateral dimensions from tens to hundreds of nanometers, compared to a sub-10 nm diameter of the ion beam.

The loss of beam processing dimensionality occurs for substrates thicker than the projected ion range in the solid. For substrates thinner than the ion range, most of effects that deteriorate the FIB pattering resolution can be avoided [1].

In addition to beam-solid interaction, other effects, such as incident ions or sputtered particles scattering or redeposition, may limit the minimum dimensions that can be achieved. In the process of nanowires fabrication by FIB induced metal deposition, scattering of incident ions in the flanks of growing nanowire is one of the reasons of a so called halo effect when a thin conductive film is deposited around the nanowire. The halo area width can reach 500 nm in the case of Pt FIB deposition (smaller halo effect is observed for W deposition) [2]. This may result in a considerable leakage between closely placed parallel wires fabricated for nanocontacting purposes [3]. In milling, redeposition of sputtered material onto the walls of milled holes or trenches makes difficult obtaining vertical walls and does not allow producing narrow holes. Materials for experiments designed to achieve an ultimate resolution in FIB processing should include light materials as C, Si and their compounds.

Ultrathin graphite layers (or multi-layer graphene, MLG) are obtained usually from highly ordered pyrolytic graphite (HOPG) by exfoliation. An alternative method for controlled deposition of thin graphite layers over metal electrodes from liquid solutions is based on ac di-electrophoresis [4,5].

This method has been successfully employed first for deposition of carbon nanotubes and more recently, thin graphene or graphite oxide layers [5]. MLG is especially interesting as a template because of its crystallinity (smaller scattering possible due to channeling) and high in-plane conductivity, the latter can help to eliminate a possible effect of layer charging during the FIB processing. A number of studies using ultrathin substrates for FIB processing has been reported [1, 6, 7]. The results obtained so far clearly demonstrate the potential of this approach to improve the FIB patterning resolution.

In the present study, simulations of ion beam interaction with thin solid membranes using well known TRIM [8] code have been realized for C, Si and Pt, the latter is an example of a heavy material. Experimental studies have been performed with MLG layers and Ga ion beam energies of 30 keV.

2. SIMULATION RESULTS

Simulations using TRIM were performed to study the interaction of Ga ions with thin amorphous C, Si and Pt target layers with different thickness and different ion energy (from 10 to 30 keV), and doses up to 10^7 ions. Zero beam diameters were chosen, to show clearly the lateral dimensions of the ion-solid interaction volume.

Examples that demonstrate the effect of material on the interaction volume (penetration depth and lateral expansion) are shown in Figure 1, for ion doses of 10^4. It can be seen that for a Pt target, much of the ion energy is deposited near the surface (shorter ion range, stronger scattering), resulting in wider features (~40 nm wide) that can be produced by milling or deposition processes. Deeper ion penetration and more narrow interaction area are characteristics of C and Si targets.

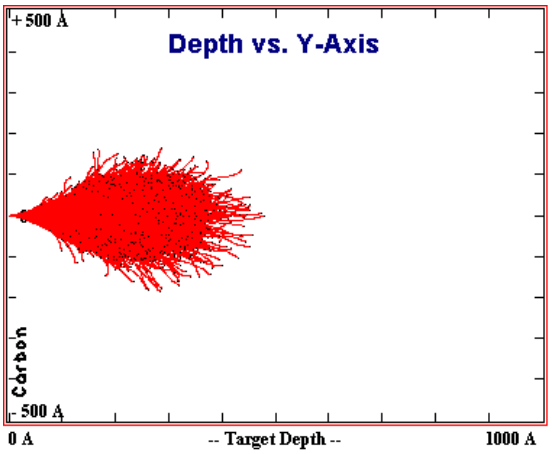

(a)

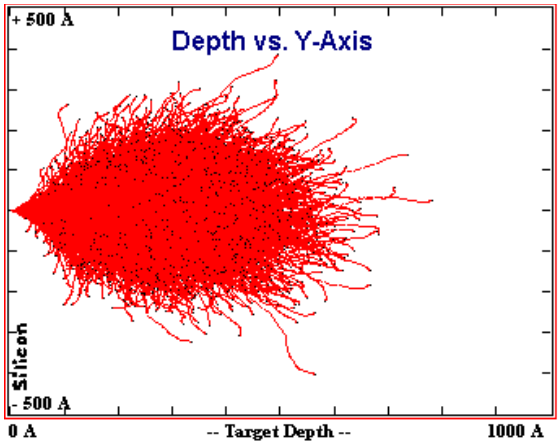

(b)

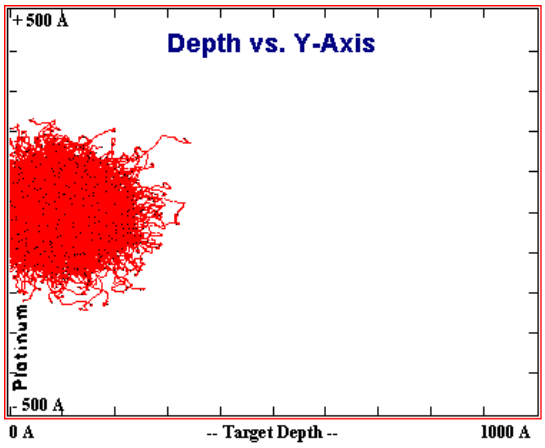

(c)

Figure 1. Results of TRIM simulations for 30 keV Ga ion beam, dose of 10^{4} ions, C (a), Si (b) and Pt (c) targets.

For carbon, where predominantly small angle scattering occurs for high energy incident ions, broadening of the interaction area is the smallest (~25-30 nm). The effect of the membrane thickness on the interaction volume is shown for carbon in Figure 2.

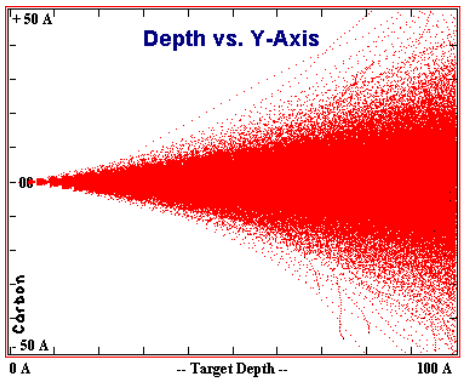

(a)

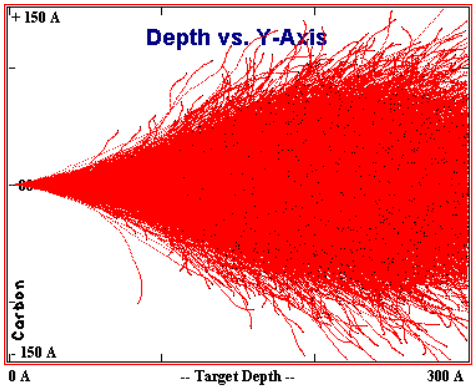

(b)

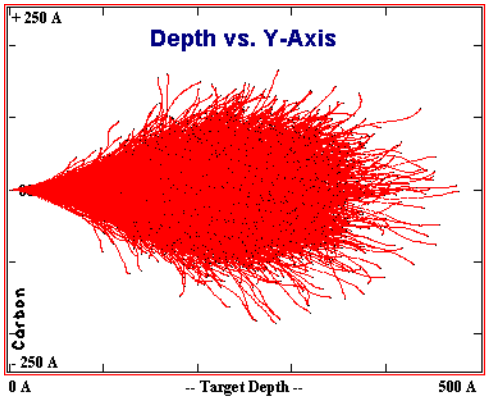

(c)

Figure 2. Results of TRIM simulations for 30 keV Ga ion beam, dose of 10^{4} ions, C target, membrane thickness of 10 nm (a), 30 nm (b) and 50 (c) nm. Note that vertical scales are different (5, 15 and 25 nm, respectively).

It can be seen that as the thickness is reduced from 50 to 10 nm, the interaction area reduces dramatically, with lateral dimensions below 10 nm for 10 nm thick membrane. For thin 10 nm membranes, the difference between light and heavy materials is more visible.

3. EXPERIMENTAL

The FIB system used here is a Dual Beam Nova 200 Nanolab from FEI Co. that combines a FIB with a scanning electron microscope (SEM). Ion beam diameter is ~7 nm at 30 keV Ga ion energy. For experimental tests, suspended multi-layer graphene (MLG) flakes with 50-100 nm thickness were used. The suspensions of MLG flakes in DMF (dimethylformamide) were prepared from natural graphite (Nacional de Grafite Ltda.) by mild sonication and centrifugation. Then, flakes were controllably deposited over metal (W) electrodes using ac-dielectrophopresis method [4,5]. W electrodes were previously formed over Si substrates by a conventional lithography and lift-off technique. Then gaps between electrodes (~1μm wide, 5 μm deep) were cut by FIB (Figure 3a). An example of a suspended MLG can be seen in Figure 3b.

Ion irradiation experiments were carried out in suspended 50-100 nm thick flakes with varying doses, keeping the area dimensions and ion current at the same values (20 x 600 nm^2 and 1 pA, respectively). By increasing the processing time from 0.8 to 6 seconds, the irradiation dose was increased from 0.4 to 3.1x10 ^{17} ions/cm^2, in seven separate 20 nm wide areas (0.8, 2, 3, 3, 4, 5 and 6 seconds irradiation), with 150 nm spacing between their centers. The results can be seen in Figure 4, where a scanning electron microscope (SEM) image of a MLG flake after irradiation is shown. Darker areas reveal the lateral dimensions of the ion beam interaction volume, where the graphene amorphization occurs. The amorphized areas have increasing lateral sizes from ~ 60 nm to 135 nm (from left to right), in accordance with the growing ion dose. Note that the minimum lateral dimension of 60 nm observed here (spreading of 40 nm over incident 20 nm wide beam) is consistent with the calculated Ga ion beam spreading in a carbon target of ~30 nm, as calculated using TRIM (see above).

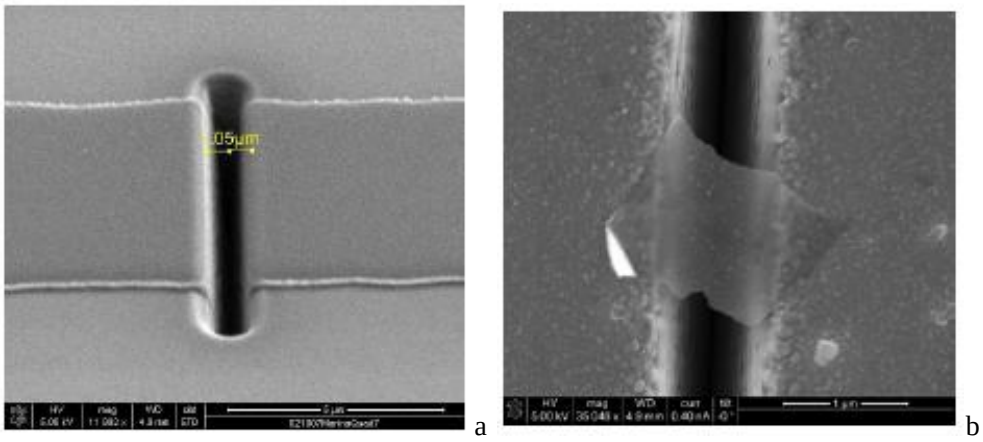

a b

Figure 3. SEM images of W electrodes after gap milling by FIB (a), and MLG deposition by dielectrophoresis (b).

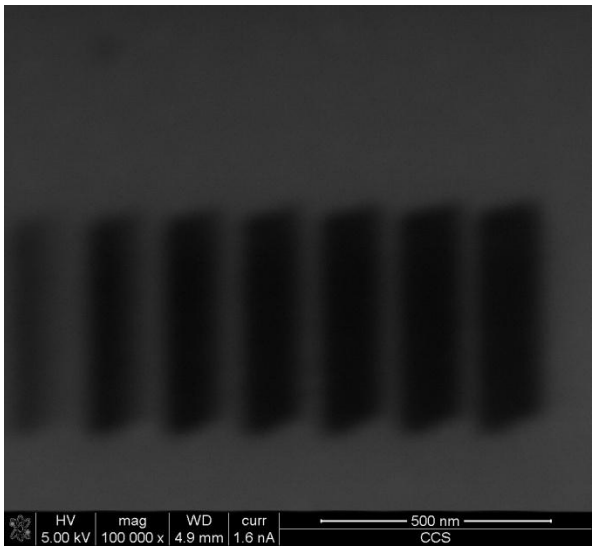

Figure 4. SEM image of MLG surface after irradiation using varying doses (increasing from 0.4 to 3.1x10 ^{17} ions/cm^2 , from left to right).

Cross-sectioning of another flake after ion irradiation with the same doses, was done using FIB milling. For this, the flake was first covered with a protective Pt-C layer deposited by electron beam induced process (Figure 5 a). After that, cross-sectioning (CS) by FIB milling was performed (Figure 5b). In the CS image, darker areas correspond to graphene and brighter areas to the metal electrode material, while the intermediate contrast corresponds to the protective Pt-C layer that is deposited over (and below) the suspended flake. The CS reveals that the flake has 50 nm thickness, and the areas milled out in it due to irradiation are ~60-80 nm wide. This is notably narrower than the area where graphene amorphization occurs (up to 135 nm), and is close to 50 nm where deposition of major ion beam energy should take place, in accordance with TRIM calculations.

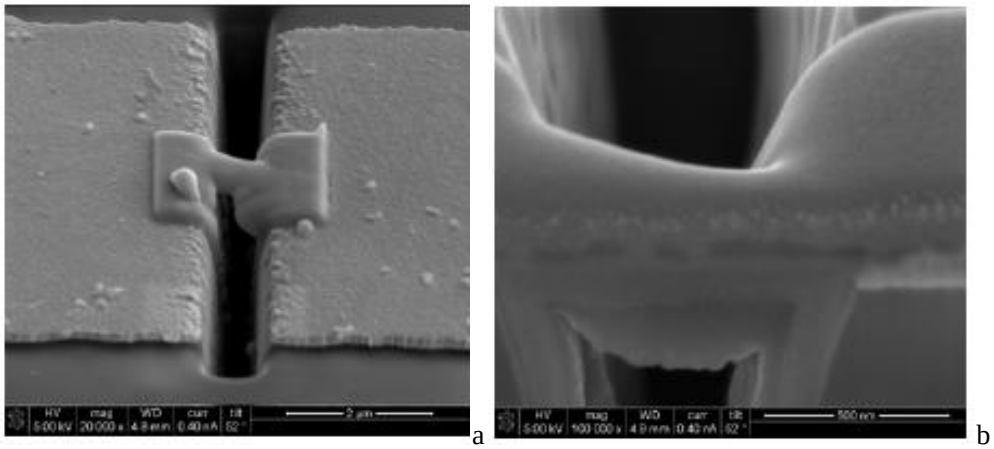

a b

Figure 5. SEM images of MLG flake covered with Pt-C protective layer (a) and cross-section of suspended MLG after FIB milling (b).

CONCLUSIONS

Simulations of ion beam interaction with membranes of C, Si and Pt were carried out. The ion beam lateral spreading was shown to be smaller for light materials like Si and especially C. For membranes with thickness smaller than the projected ion range, considerable reduction in lateral dimensions of the ion interaction area and thus, improved resolution of ion beam processing, can be achieved. Experiments with ion beam irradiation at different doses were carried out with suspended multi-layer graphene flakes. Cross-sectioning using FIB milling revealed that the material removal occurs in areas 60-80 nm wide, in accordance with the TRIM simulation results. Further studies with thinner MLG samples are in progress to achieve better ion beam processing resolution.

ACKNOWLEDGMENTS

The authors would like to thank Dr. James Ziegler for permission to use TRIM code, CCS-UNICAMP staff for technical assistance, and CPNq, FAPESP and INCT NAMITEC for financial support.

REFERENCES

[1] J. Gierak, A. Madouri, A. L. Biance , E. Bourhis , G. Patriarche , C. Ulysse , D. Lucot. *Microelectron. Eng*. 84 (2007) 779-783.

[2] S. K. Tripathi, N. Shukla, N. S Rajput and V. N. Kulkarni. *Nanotechnology* 20 (2009) 275301.

[3] A. R. Vaz, M. M. da Silva, J. Leon, S. A. Moshkalev and J. W. Swart. *J. Mater. Sci*. 43 (2008), 3429-3434.

[4] S.A. Moshkalev, J. Leon, C. Veríssimo, A. R. Vaz, A. Flacker, M. B. de Moraes and J. W. Swart, *J. Nano Research* 3 (2008), 25

[5] F. P. Rouxinol, R.V. Gelamo, R. G.. Amici, A.R. Vaz, S. A. Moshkalev. *Appl. Phys. Lett.* 97 (2010) 253104.

[6] J. Gierak, E. Bourhis, G. Faini, G. Patriarche, A. Madouri, B. Schiedt, A.-L. Biance, L. Auvray. *Ultramicroscopy* 109 (2009) 457.

[7] A. Böttcher, M. Heil, N. Stürzl, S. S. Jester, S. Malik, F. Pérez- Willard, P. Brenner, D. Gerthsen and M. M. Kappes. *Nanotechnology* 17 (2006) 5889.

[8] J. F. Ziegler. TRIM/SRIM - *The Stopping and Range of Ions in Matter*. Available at: http://www.srim.org.